

Portland State University

PDXScholar

Dissertations and Theses

Dissertations and Theses

1-1-2010

Radiative Transfer Theory Applied to Ocean Bottom Modeling

Jorge Quijano

Portland State University

Follow this and additional works at: https://pdxscholar.library.pdx.edu/open_access_etds

Let us know how access to this document benefits you.

Recommended Citation

Quijano, Jorge, "Radiative Transfer Theory Applied to Ocean Bottom Modeling" (2010). *Dissertations and Theses*. Paper 516.

<https://doi.org/10.15760/etd.516>

This Dissertation is brought to you for free and open access. It has been accepted for inclusion in Dissertations and Theses by an authorized administrator of PDXScholar. Please contact us if we can make this document more accessible: pdxscholar@pdx.edu.

Radiative Transfer Theory Applied to Ocean Bottom Modeling

by

Jorge Eduardo Quijano

A dissertation submitted in partial fulfillment of the
requirements for the degree of

Doctor of Philosophy
in
Electrical and Computer Engineering

Dissertation Committee:

Lisa M. Zurk, Chair

James McNames

Martin Siderius

Donald Duncan

Mark Sytsma

Portland State University

©2010

Abstract

Research on the propagation of acoustic waves in ocean bottom sediment is of interest for active sonar applications such as target detection and remote sensing. Currently, all seabed scattering models available in the literature are based on the full solution of the wave equation, which sometimes leads to mathematically intractable problems. In the electromagnetics community, an alternative formulation that overcomes some of this complexity is radiative transfer theory, which has established itself as an important technique for remote sensing. In this work, radiative transfer (RT) theory is proposed for the first time as a tool for the study of seabed acoustic scattering. The focus of this work is the development of a complete model for the interaction of acoustic energy with water-saturated sediments. The general geometry considered in this study consists of multiple elastic layers containing random distributions of inhomogeneities. The accuracy of the proposed model is assessed by rigorous experimental work, with data collected from random media in which acoustic properties such as the concentration and size of scatterers, background material, and the presence of elastic boundaries are controlled parameters. First, the ultrasound RT model is implemented for layers of finite thickness. The range of applicability of the proposed model

is then illustrated using scaled experiments conducted at the Northwest Electromagnetics and Acoustics Research Laboratory (NEAR-Lab). Next, the model is applied to field data collected in a region with gassy sediments and compared to the formulation originally used to explain these data. Finally, insight into the emerging area of study of the time-dependent RT formulation is presented, and its role in the representation of finite broadband pulses is discussed.

Acknowledgments

I want to thank the Office of Naval Research for all the support in the development of my career and for sponsoring this research work.

I am heartily thankful to my advising Professor, Dr. Lisa M. Zurk, for all the guidance provided during my studies. Her continuous support and total commitment for the past five years has enormously enriched my life as a professional and as a human being, and I am grateful for all the wonderful opportunities that I have enjoyed while working with her at the NEAR-Lab.

Thanks to Dr. Dajun Tang and Dr. Dan Rouseff for taking time out of their hectic schedule to be mentors, role models and friends. The time we have spent together during experiments, conferences and discussions has meant a lot to me.

I would like to thank Dr. James McNames and Dr. Malgorzata Chrzanowska-Jeske from the ECE Department for guiding me during my first years as an international student at Portland State University.

I am grateful to Dr. Jean-Pierre Sessarego (CNRS) and Dr. DJ Tang (APL) for lending equipment and materials required to complete my experimental work

at the NEAR-Lab.

Thank you to Dr. Richard Campbell for all his insight into the area of experimental work, and for teaching me that circuit design is another form of art.

Thanks to Dr. Martin Siderius and Dr. Altan Turgut for stimulating discussions and general advice in the advancement of my career.

Thanks to Drs. Lisa Zurk, Richard Campbell, James McNames, Martin Siderius, Donald Duncan and Mark Sytsma for serving on my Committee.

I am indebted to my coworkers at the NEAR-Lab for their support and for helping me relax during busy times, and special thanks to Gabe, Sam, Scott, George, John, Richard, Alex, Eric, Joe and Brian for countless times helping me with my English. Thanks to Garth for valuable insight on how to pass the Ph.D. qualifier tests.

Finally, I would like to thank my family for being there for me every time I needed a friend, and for always believing in me. I dedicate this work specially to my parents for all the unconditional love.

Contents

Abstract	i
Acknowledgments	iii
List of Tables	ix
List of Figures	x
1 Overview of Dissertation Work	1
1.1 Focus of dissertation	5
1.2 Contributions and significance of this work	6
1.3 Summary of dissertation	8
2 Introduction to Seabed Acoustics	10
2.1 Mechanisms of scattering	10
2.2 Scattering from random media: definition of main quantities . . .	14
2.3 Classic approach to scattering from random media	16
2.4 Conclusion	19

3	Radiative transfer model for elastic media	21
3.1	Scalar radiative transfer	24
3.2	Vector radiative transfer	27
3.2.1	Statement of the equation and boundary conditions	27
3.2.2	The reduced intensity for a finite layer	34
3.2.3	The vector RT equation for diffuse intensity with multiple coherent sources	38
3.2.4	Solution of the vector RT equation by Fourier Series and Gaussian Quadrature integration	42
3.3	Transient radiative transfer	50
3.4	Power conservation	52
3.4.1	The scalar case	53
3.4.2	The vector case	56
3.4.3	Numeric example of power conservation in lossless sediment	57
3.5	Obtaining the scattering cross section from transport theory . . .	63
3.6	Conclusion	66
4	Validation of the RT scattering simulator	67
4.1	Scattering from a single elastic particle	67
4.2	Plane wave reflection coefficients	72
4.2.1	Plane wave reflection coefficients for a fluid-solid interface	74

4.2.2	Plane wave reflection coefficients for a solid-solid interface	77
4.3	Solution of the steady-state RT equation	79
4.3.1	Dependency of the steady state solution on the absorption	81
4.3.2	Dependency of the steady state solution on the depth . . .	82
4.4	Solution of the transient RT equation	84
4.5	Conclusion	86
5	Scaled tank experiments and comparison with the radiative transfer model	88
5.1	Experimental setup and calibration	89
5.2	Processing of experimental data	94
5.3	Experiment 1: Aluminum scatterers in water background	95
5.4	Experiment 2: Aluminum scatterers in sand background	98
5.4.1	Characterization of the sand	98
5.4.2	Measurements of volume scattering	102
5.5	Experiment 3: Glass scatterers in resin background	106
5.6	Conclusion	110
6	Comparison of the model to field experimental data	114
6.1	The Eckernförde Bay experiment	115
6.2	RT model for thin and thick layers of randomly distributed scatterers	117
6.3	Conclusion	121

7	Time domain solutions obtained by the radiative transfer method	124
7.1	Time domain dependency of the scattered intensity: an analytical model	125
7.2	Impulse response of a finite layer obtained from the transient RT equation	127
7.3	Conclusion	130
8	Conclusion and future work	133
8.1	Conclusion	133
8.2	Future work	136
8.2.1	Implementation of the Dense Media Radiative Transfer for acoustics	136
8.2.2	Extension of the model to include rough interfaces	137
8.2.3	Radiative Transfer in media with gradients	139
	References	141
A	Definition of Stoke's parameters	146
B	Publications and talks related to this research	148

List of Tables

3.1	Acoustic properties of the sediment and water column used in the RT simulation.	59
4.1	Power (\sim) and Specific Intensity (\wedge) reflection/transmission coefficients for the fluid-elastic interface.	77
5.1	Acoustic properties of the scattering media used in this work. Most of the values for the sand background were measured in the laboratory, as detailed in section 5.4.	89
5.2	Examples of scaling of the performed tank experiments to field experiments. The center frequency of the tank experiments is 350 kHz, corresponding to a wavelength of 4.3 mm.	111
6.1	Acoustic properties of the sediment at the Eckerfoerde Bay. . . .	117
7.1	Acoustic properties of environment in Fig. 7.1 used to obtain solutions to the Transient RT equation.	128

List of Figures

1.1	Illustration of a general active sonar system in a layered ocean environment, where each layer n is characterized by the density ρ_n and the sound speed c_n . The signal at the receiver is a superposition of the direct and the target arrivals, combined with undesired echo returns from the surface and the bottom known as reverberation.	2
1.2	(a) Example of an acoustic survey performed in the eastern coast of New Jersey during the Shallow Water 2006 experiment, revealing strong reflectors that indicate a layered structure. (b) Core sample taken near the area corresponding to the chirp survey shown in (a). Chirp survey data and photographs provided by Dr. Altan Turgut (NRL).	3

2.1	(a) In a perfectly smooth surface, part of the energy is reflected at the specular angle and part is transmitted according to (2.1); (b) When the surface is rough, the energy in the specular direction is reduced and re-distributed in a main lobe and side lobes.	12
2.2	Scattering mechanisms in the ocean sea bed: (a) <i>Multiple-layers</i> contribute to the total volume scattering by redirecting coherent energy to interact multiple times with scatterers in the layers. (b) <i>Single scatterers</i> are regions within the layers where the acoustic impedance $Z_n = \rho_n c_n$ has an abrupt change. (c) <i>Refraction</i> due to gradients in the sound speed and/or the density is considered a form of volume scattering, because it can transport energy back to the water column.	13
3.1	Definition of the specific intensity $I(r, \hat{s})$ as the energy that goes through a differential area da and within a differential solid angle $d\Omega$. The specific intensity forms an angle θ with the normal to the surface da	22
3.2	Change in the specific intensity $I(\vec{r}, \hat{s})$ when it propagates through a differential volume dV containing η scatterers/ m^3 : (a) Loss mechanism due to scattering of energy into direction \hat{s}' ; (b) Gain mechanism, due to coupling of energy from direction \hat{s}' into \hat{s} . . .	23

3.3	View of a parallel-plane scattering media in which the z axis points down and $z = 0$ m corresponds to the water-sediment interface. Since the statistical properties along the x/y coordinates are constant, the specific intensity depends only on the depth z and the direction, specified by the azimuth angle ϕ and the elevation angle θ , so $I(\vec{r}, \hat{s}) = I(z, \theta, \phi)$. Without loss of generality, it can be assumed the the azimuth of the incident radiation is zero ($\phi_o = 0$).	25
3.4	Partition of energy in longitudinal, shear vertical and shear horizontal polarizations for incident waves with different polarization. As in the scalar case presented in section 2.2, $P_{ab} = 4\pi f_{ab} ^2$. Note that longitudinal scattered waves propagate with a wavenumber $k_L = \omega/c_L$ while transversal waves propagate with wavenumber $k_T = \omega/c_T$, where c_L and c_T are the sound speed for longitudinal and shear waves, respectively.	28

3.5	The reduced intensity can be collimated in 8 different directions:	
	(a) The upward longitudinal intensities $I_{ri_1}^{L_1\uparrow}$ and $I_{ri_1}^{L_2\uparrow}$ result from the transformations L-L-L and L-y-L, respectively, where L stands for <i>longitudinal</i> and y for <i>shear vertical</i> ; (b) Similar to (a) for $I_{ri_1}^{y_1\uparrow}$ (L-y-y) and $I_{ri_1}^{y_2\uparrow}$ (L-L-y); (c) The downward longitudinal intensities $I_{ri_1}^{L_1\downarrow}$ and $I_{ri_1}^{L_2\downarrow}$ correspond to the transformations L-L and L-y-L-L, respectively; (d) Similar to (c) for $I_{ri_1}^{y_1\downarrow}$ (L-y) and $I_{ri_1}^{y_2\downarrow}$ (L-L-y-y). . .	35
3.6	Interpretation of the inner and outer frequency scales: (a) Illustration of the time domain of the excitation signal, with a frequency of oscillation ω ; (b) Corresponding input excitation in terms of specific intensity; (c) Input excitation in the outer frequency domain Θ , which describes the rate of change of the specific intensity in (b).	52
3.7	Layered environment consisting of an infinite halfspace and a finite layer of thickness z_d with embedded cavities. Since the background media for layers 1 and 2 are the same, no energy is reflected back from this interface.	58

3.8	A longitudinal wave in the fluid reaches the fluid-solid boundary: \tilde{R}_{01}^{LL} (circles), \tilde{T}_{01}^{LL} (solid) and \tilde{T}_{01}^{Ly} (squares) for the parameters in Table 3.1. Note the critical angle for the transmitted longitudinal wave when $\theta_o = \sin^{-1}(c_f/c_L)$	59
3.9	A longitudinal wave in the solid reaches the solid-fluid boundary: \tilde{T}_{10}^{LL} (solid), \tilde{R}_{10}^{LL} (circles) and \tilde{R}_{10}^{Ly} (squares) for the parameters in Table 3.1. Most of the energy carried by the longitudinal wave in the sediment is transmitted to the water for $0 < \theta_L < 60^\circ$	60
3.10	(a) Scattering cross section for a transversal plane wave at 10 kHz ($k_T = 537 \text{ m}^{-1}$); (b) Same as (a) for an incident longitudinal wave ($k_L = 37.2 \text{ m}^{-1}$). A resonance peak can be observed at $a =$ 3.8 mm. In the example in this section, scatterers with $a = 10 \text{ mm}$ are utilized.	61

- 3.11 Normal component of the outgoing power flux in layer 1, for a configuration Water-Sand-Sand and no background attenuation.
- (a) The difference $F_{ri_0}^{L_1\downarrow} - F_{ri_0}^{L_1\uparrow}$ at $z = 0$ indicates the power flux that is transmitted into layer 1 from the water column; (b) Total upward (red) and downward (black) diffuse power flux at $z = 0$ and $z = z_b$ m, respectively; (c) and (d) show the power flux from coherent longitudinal and shear vertical energy, respectively (note different scale on (d)). Due to the transparent boundary condition at $z = z_b$, $F_{ri_1}^{L_1\uparrow}$, $F_{ri_1}^{L_2\uparrow}$, $F_{ri_1}^{L_2\downarrow}$, $F_{ri_1}^{y_1\uparrow}$, $F_{ri_1}^{y_2\uparrow}$ and $F_{ri_1}^{y_2\downarrow}$ are zero. 62
- 3.12 Measurement of volume scattering from layered media: (a) General bistatic geometry in which a directional transmitter(TX) illuminates a patch (blue) defined by its radiation pattern and its distance from the media. The omni directional receiver detects the energy crossing the area dA (gray); (b) Monostatic configuration used in the experiments presented in section 5. 64

4.1	(a) Scattering of a shear wave incident upon a spherical elastic inclusion with $c_{Lp} = 6000$ m/s, $c_{Tp} = 3500$ m/s, and $\rho_p = 2700$ kg/m ³ , surrounded by elastic media with $c_{L1} = 1400$ m/s, $c_{T1} = 0.1$ m/s, and $\rho_1 = 1000$ kg/m ³ . The blue line corresponds to the normalized cross section, the black line represents the portion of energy scattered as a shear wave and the red line is the energy scattered as a longitudinal wave. (b) Similar results found in the literature are shown for comparison.	73
4.2	(a) A longitudinal wave in fluid media impinges upon a fluid-sediment interface, producing a reflected longitudinal wave and transmitted longitudinal and shear vertical waves; (b) A longitudinal wave in the sediment excites a longitudinal wave in the fluid and reflected longitudinal and transverse waves in the sediment; (c) Similar to (b) for an incident shear vertical wave in the sediment. In all cases, the refracted angles are defined by Snell's law stated in (4.7).	75
4.3	(a) Example of the computation of (4.8) for $c_{L0} = 557$ m/s, $\rho_0 = 664$ kg/m ³ , $c_{L1} = 1670$ m/s, $\rho_1 = 1992$ kg/m ³ and c_{T1} varying from 928 m/s to 1044 m/s; (b) Similar results can be found in the literature.	78

4.4	(a) A longitudinal wave in elastic media impinges upon a sediment-sediment interface, producing transmitted/reflected longitudinal and shear vertical waves; (b) Same as (a) for an incident shear vertical wave; (c) Shear horizontal waves only excite transmitted/reflected waves with the same polarization. In all cases, the refracted angles are defined by Snell's law stated in (4.11).	79
4.5	Measurement of the diffuse intensity as a function of angle θ in an infinite half space at $z = 0$ m (a) and at $z = z_1$ m (b).	80
4.6	The diffuse intensities $I_{dL}(0 < \mu < -1, \phi = 0, \tau = 0)$, $I_{dx}(0 < \mu < -1, \phi = 0, \tau = 0)$ and $I_{dy}(0 < \mu < -1, \phi = 0, \tau = 0)$ corresponding to the measurement depicted in Fig. 4.5(a): (a) Solution obtained at the NEAR-Lab for low absorption (left) and high absorption (right) of $\tilde{\nu}_T = 0.111$ and $\tilde{\nu}_L = 0.0555$, respectively. In both cases, the single scattering solution (dashed lines) is shown for comparison with the full solution (solid lines); (b) Results found in the literature for comparison.	83

4.7	(a) Depth dependency of the diffuse intensities $I_{dL}(\mu, \phi = 0, \tau)$ (blue), $I_{dx}(\mu, \phi = 0, \tau)$ (black) and $I_{dy}(\mu, \phi = 0, \tau)$ (red) corresponding to the measurement depicted in Fig. 4.5(b) at five depths: $\tau = 0$, $\tau = 0.5$, $\tau = 1$, $\tau = 3$ and $\tau = 5$. The horizontal line at each depth indicates $\mu = 0$. (b) Results found in the literature for comparison.	85
4.8	(a) Example of the structure information that can be obtained from time domain solutions of the RT equation. In this simulation, the specific intensity as a function of time is simulated at angles $\theta = 0^\circ$ (blue), $\theta = 49^\circ$ (red) and $\theta = 76^\circ$ (black). (b) Results found in the literature are shown for comparison.	87
5.1	(a) Photograph of the equipment available to perform ultrasound scattering experiments, including a 5x7x3 feet tall acrylic tank, aluminum rail for sensor positioning, amplifiers and a PCI 6110 DAQ board; (b) Diagram of the connection of the hardware elements used in this series of experiments.	90

5.2	Comparison between the measured backscattered energy and the Mie analytical solution (section 4.1) for single spheres of (a) tungsten-carbide with radius $a = 1.9$ cm and (b) steel with radius $a = 1.03$ cm. These measurements verify the system calibration as a preliminary step to the experiments with random media.	93
5.3	(a) Photograph of an ensemble of aluminum spheres suspended with nylon filament in the center of a wooden frame; (b) Example of time domain realizations of the scattered signal from a single sphere and from the ensemble of spheres corresponding to a fractional volume $FV = 2.7$ %. The dashed boxes indicate the time gating used to define $w_n^s(t, \theta_i)$ in (5.1).	96
5.4	Comparison of the measured backscattering $\Upsilon_{av}(f, \theta_i = 0)$ (solid lines), with computations from the RT model for an ensemble of aluminum spheres, with fractional volume (FV) as a parameter. For reference, experimental and theoretical scattering from a single sphere are also shown.	97

5.5	(a) Scattering of a broadband pulse from the sand slab, showing the incident pulse (I_o) and energy reflected from the water-sand interface (I_1) and from the bottom of the tank (I_2). The graph shows the envelope of the scattered pulse after performing pulse compression. The vertical axis is given in units of distance, with the zero lined up to I_1 ; (b) Zoom-in of (a), where scattering from the sand can be observed.	100
5.6	Estimation of the frequency-dependent attenuation of the sand slab as $\ln[I_2/I_o](1/(4z_d))$, showing the measured value (solid line) and the linear fit (dotted line) in (5.3).	101
5.7	(a) Aluminum spheres of radius $a = 2.4 \text{ mm}$ deposited on top of the sand layer. The spheres were pushed within the sand to obtain the configuration shown in (b); (b) Setup for experiment 2, with scatterers located at depths between 1 cm to 7 cm. The amplitude of the scattered energy can be seen to the left, and it exhibits a maximum around 3 cm depth.	103

5.8	(a) Volume scattering from the aluminum spheres and the sand compared to the RT model. The offset between the experimental data and the model is due to scattering from the sand itself. This figure also shows scattering from a rigid aluminum reflector, as well as the energy reflected by the sediment-water interface; (b) Same as (a), but the volume scattering is compensated as indicated in (5.4).	105
5.9	(a) Example of two realizations of the backscattered signal after pulse compression, for $\theta = 0^\circ$ and $\theta = 10^\circ$. The waveforms are normalized to the peak value of the direct blast. (b) $\Upsilon_{av}(f, \theta_i)$ for the two incident angles in (a), with thin solid lines indicating ± 1 standard deviation around the mean of 30 realizations.	112
5.10	Comparison of the measured backscattering, $\Upsilon_{av}(f, \theta)$ (solid lines), with computations from the RT model at 300 kHz and 400 kHz (dashed lines). Computation of backscattering at 500 kHz is also shown (black, dashed line) for comparison to previous experimental work using this slab (see text for details).	113

6.1	Experimental setup for the Eckernfoerde Bay experiment: (a) 3D view of the angle of incidence of the transmitted spherical wave as a function of range; (b) Side view of the experiment and the structure of the seabed. It was found experimentally that $z_{d1} \approx 1 \text{ m}$, while the thickness of the layer, $z_d = z_{d2} - z_{d1}$ is used as a free parameter in the next section.	116
6.2	Backscattering strength vs bubble radius, for a sand background with $c_{L1} = 1468 \text{ m/s}$ and $\rho_1 = 1100 \text{ m/s}$. The average size of the scatterers is obtained from this figure by choosing a value in agreement with the constraint in (6.6).	120
6.3	Comparison of the RT model to the experimental data collected at the Eckernfoerde Bay and to a single scattering model proposed in the literature. The RT model was run with $a = 3.5 \text{ mm}$, $\eta = 112500 \text{ scatterers/m}^3$, $FV = 1.2\%$, and the sediment parameters in Table 6.1. The thickness $z_d = 0.08 \text{ m}$ yielded the best match to the experimental data. RT simulations with $z_d = 0.4 \text{ m}$ and $z_d = 0.8 \text{ m}$ are also shown to illustrate the effect of saturation. . .	122

7.1	General geometry of a monostatic active system that transmits a finite pulse $v_i(t)$ and receive the acoustic echo $v_o(t)$. The scattering media can be represented as a linear system with an impulse response $h(t)$, and an analytical approximate solution can be obtained.	125
7.2	Solution of the transient RT equation (full and single scattering approximation) and comparison to the analytical solution in (7.5). The full solution is in agreement with energy conservation and therefore it represents more accurately the impulse response of the random media.	129
7.3	Coherent and diffuse normal power fluxes at $z = 0$ and $z = R_2 - R_1$ for: (a) The single scattering solution of the transient RT equation and (b) The full solution. The curve labeled as <i>Total</i> refers to the summation in the right hand side of (7.6), and it must equal $F_{ri_0}^{L_1 \downarrow} _{z=0}$ in conservative media.	131
8.1	Illustration of the Kirchhoff approximation for rough surfaces: with this approach, the plane wave reflection coefficients become a function of the position (x,y) along the rough surface, and the angles of reflection and refraction are defined with respect to the vector \hat{n} , normal to the local tangent.	138

8.2	Depth-dependent sound speed in a core sample of sediment from the New Jersey shelf area. The red line shows the general trend of the upward refracting sound speed profile. Data provided by Dr. Altan Turgut, NRL.	139
-----	--	-----

Chapter 1

Overview of Dissertation Work

Scattering of sound from the seabed has been an important area of research within the underwater acoustics community for the last 50 years. Models for acoustic scattering are of great importance for multiple applications involving active sonar. In these systems a known acoustic signal is transmitted into the water and a receiver listens for echoes reflected by potential targets of interest, as illustrated in Fig. 1.1. Frequently, acoustic energy interacts with the ocean bottom either intentionally (as in remote sensing of the sub-bottom layered structure for geological studies) or unintentionally (as in active sonars used for surveillance and port security). In all cases, it is advantageous to have an accurate model that describes the interaction of sound with the sediment.

To illustrate the complexity of the seabed, Fig.1.2(a) shows an example of a chirp survey performed in the eastern coast of New Jersey during the Shallow Water 2006 experiment. The survey consisted of dragging an echo sounder along a straight path, while continuously transmitting a broadband signal. At each

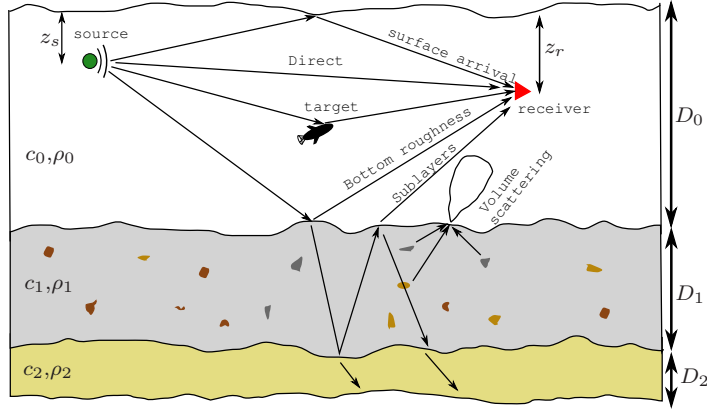


Figure 1.1: Illustration of a general active sonar system in a layered ocean environment, where each layer n is characterized by the density ρ_n and the sound speed c_n . The signal at the receiver is a superposition of the direct and the target arrivals, combined with undesired echo returns from the surface and the bottom known as reverberation.

ping, the reflected echo was recorded and it shows the layered structure of the sea floor, with sublayers of different thickness ranging from 1 to 4 meters. Figure 1.2(b) shows the internal structure of the subbottom layers from a core sample extracted in the same area. It exhibits multiple individual scatterers such as rocks and shells, and similar examples can be found in the literature[1, 2, 3, 4].

Several models with different levels of complexity have been proposed, all of them based on solutions to the wave equation. With this technique, scattering due to multiple layers with arbitrary random inhomogeneities can be described by an integral equation[5]. Although this approach is in principle exact, the solution methods require making approximations about the seabed parameters or restricting the excitation signal within a particular frequency band in order to make the problem mathematically tractable. Examples of common approximations that

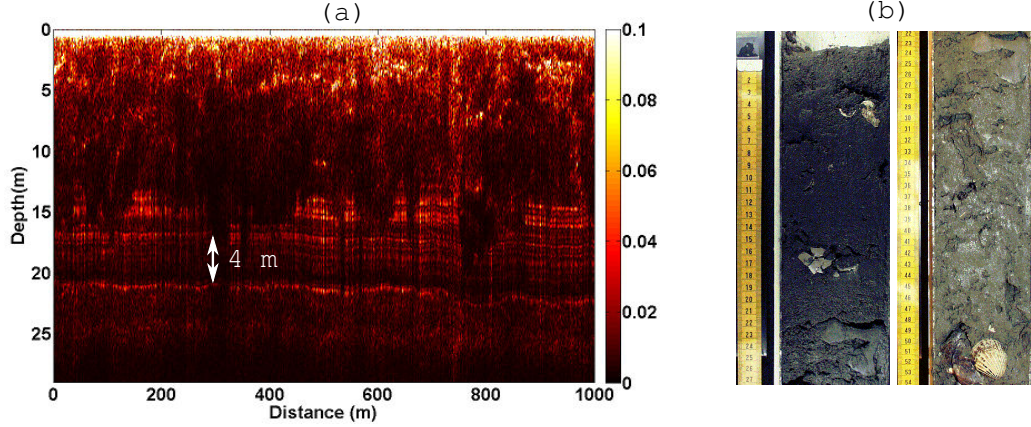


Figure 1.2: (a) Example of an acoustic survey performed in the eastern coast of New Jersey during the Shallow Water 2006 experiment, revealing strong reflectors that indicate a layered structure. (b) Core sample taken near the area corresponding to the chirp survey shown in (a). Chirp survey data and photographs provided by Dr. Altan Turgut (NRL).

might limit the applicability of classic scattering models are:

1. Scatterers are weak perturbations (Born approximation): These methods are adequate in sediments with small random variations in the sound speed or density[6, 7], but they can not be used in the case of strong scatterers such as shells or bubbles[8, 4].
2. Multiple scattering events can be ignored: Methods using this assumption can be applied to media with low concentration of scatterers and with high background attenuation. In most cases these models have shown good agreement with experimental backscattering data, but they have underestimated volume scattering in certain environments[9] and it has been suggested that this might be due to neglecting of multiple scattering.

3. Effect of shear waves can be ignored: This is a valid assumption in fluid-saturated sediments, which poorly support propagation of shear waves. For more consolidated media, simulations[10] have shown that the shear contribution should not be neglected in computation of volume backscattering.
4. Shallow acoustic penetration: This assumption allows neglect of contributions due to deep layers/scatterers, but it might limit the applicability to frequencies higher than 10 kHz and shallow grazing angles[8].

An alternative to the classic approach is Radiative Transfer (RT), a technique based on the principle of conservation of energy and founded in the fact that in random media, the phase of scattered waves at any arbitrary location is random and therefore no information can be extracted from it. Given that the unnecessary phase information is not required in the model, it has been suggested[11, 12] that the solution of the RT integro-differential equation is in general simpler than its classic counterpart and therefore, fewer approximations are required.

This work is inspired on the successful use of the RT techniques in research fields related to electromagnetics, in particular for applications of remote sensing in geophysics and astrophysics. These applications are examples of parallel rough layers with random scatterers, similar to the typical configuration found in the ocean seabed, and several solution techniques are already available and can be adapted to acoustics.

1.1 Focus of dissertation

In this research, the use of the RT equation to model ocean bottom scattering is suggested for the first time. The model has been used intensively in electromagnetics and there is a large number of examples that illustrate its applicability for the study of electromagnetic scattering from media such as clouds with suspended water droplets. As evidenced in the next sections, translating this formulation from electromagnetics into acoustics is not a trivial task, since it requires a whole new set of elastic equations to describe the partition of energy into three kinds of polarizations (i.e. longitudinal, shear vertical and shear horizontal), as opposed to the two polarizations that characterize electromagnetic waves.

To evaluate the performance of the proposed model and compare its capabilities with other models found in the literature, it was required to implement a software simulation tool for the computation of acoustic scattering by solving the transport equation. This simulator accepts input parameters describing the elastic media such as speed of sound, density, concentration of scatterers, and background attenuation, and it solves the Ultrasound Radiative Transfer Equation (URTE) to predict the amount of volume scattering.

1.2 Contributions and significance of this work

The RT technique allows exploring the topic of scattering by random media from a totally different perspective than the existing “classic” methods. To this date, the only applications that have been suggested for the RT theory in acoustics are characterization of materials by ultrasound [13, 14, 15] and seismics [16], with focus on theoretical work without experimental validation. While the creation of software to implement the RT scattering model was based on previous publications, the work presented here makes the following contributions:

1. Extension of the solution method for the URTE to finite layers with reflective boundaries, as opposed to the layer of infinite thickness previously assumed in the literature[13, 14]. This increases the range of application of the model by accounting for the effect of multiple bounces of coherent energy between the boundaries of the layer, as well as multiple stacked layers. This extension applies to the steady-state RT equation (i.e. the media is excited by a permanent source at a single frequency) as well as the transient RT equation[15], which is one of the latest developments in the field of transport theory and it can be used to explore scattering due to broadband finite pulses in the time domain.
2. Development of a mathematical expression to show that the conservation of power holds for the proposed model. This algebraic derivation shows

that the gradient of the power flux in a volume containing lossless elastic media must be zero. This method is utilized in this work as a criteria for the accuracy of steady-state and transient solutions of the RT equation.

3. Validation of the proposed model by comparison to published experimental results corresponding to scattering from gas bubbles trapped in sandy sediment. It was observed that the RT model converges to a single scattering model proposed in the literature for thin layers of scatterers, but the RT model is not limited to this assumption and it can be used in less restrictive experimental conditions.
4. Validation of the RT model by comparison of simulations to measured scattering levels from well characterized random media. Tank experiments were conducted in the NEAR-Lab measurement facility at ultrasound frequencies using several combinations of background material and scatterers. These measurements allowed assessing the accuracy of the model by systematically varying experimental parameters such as the frequency range, attenuation of the background media, concentration of scatterers and their size relative to the wavelength of the excitation signal.

The impact of this work in the underwater acoustics community is on increasing the understanding of the spatial and temporal characteristics of scattering. In general, the RT model provides insight into the physical phenomena of scattering

and it is characterized by its flexibility to adapt to a broad range of experimental conditions.

The model has been well received in the underwater acoustics community, and appendix B contains a list of conference talks and publications related to this work.

1.3 Summary of dissertation

Chapter 2 provides a review of the main scattering mechanisms that must be considered in a model for seabed scattering, and it defines the main parameters and terminology commonly used in the underwater acoustics community. At the end of the chapter, an introduction to classic scattering models is provided and common shortcomings are described.

Chapter 3 focuses on the theory behind the RT model, and describes the equations used to implement software routines for the solution of the transport equation in layered elastic media. This chapter also defines the mathematical formulation that describes power conservation, as well as the definition of the scattering cross section.

Chapter 4 introduces additional concepts related to scattering in random media, and it presents a numerical validation of the model by comparing simulated results to material published in other fields of acoustics.

Chapter 5 shows the applicability of the RT model for the analysis of experimental data obtained in a scaled setup and using well characterized models of random media. In this chapter, simulations of the scattering cross section obtained with the RT model are compared to the measured cross section of three experiments with increasing levels of complexity. The scattering media in these experiments is representative of the conditions in real field experiments, with the advantage of the well controlled environment of a tank setup.

Chapter 6 presents the application of the RT model to field experimental data. The chapter describes an experiment performed by another research group in 1993, and it continues with a description of a simplified RT model that applies to thin layers of scatterers and a comparison to the experimental data.

Chapter 7 illustrates the application of the transient RT formulation to a numerical example with parameters relevant to underwater acoustics, and it compares the model to an analytical “classic” model that can be obtained from wave theory under special experimental conditions.

Chapter 8 summarizes the findings of this work and present areas for additional research.

Chapter 2

Introduction to Seabed Acoustics

The goal of this chapter is to familiarize the reader with the characteristics of the scattering media, as well as with the terminology commonly used in the field of acoustic scattering, in particular the concept of scattering cross section, which will be used in this work to compare experimental measurements with simulated results from the RT model. As a review of the limitations of current scattering models based on approximate solutions to the wave equation, this chapter presents an overview of the *integral method*, which is the starting point of most of the models currently available.

2.1 Mechanisms of scattering

As mentioned in the introduction, the sea floor is a very complex system that may include rough interfaces, multiple layers, single scatterers and smooth variations in parameters such as the sound speed or the density. When acoustic energy interacts with this medium, each of the mentioned factors will have an

impact on the propagation of acoustic waves, and therefore will determine the amount of energy that is scattered back into the water column. Figures 2.1 and 2.2 illustrate the main processes related to acoustic scattering from the ocean seabed in a layered environment:

i) Surface roughness: roughness can be defined as the size of the features in a surface compared to the wavelength λ of the incident wave. If a surface is perfectly smooth as in Fig. 2.1 (a), part of the energy is reflected at the specular direction and part is transmitted at an angle that obeys Snell’s law of refraction:

$$\rho_0 c_0 \sin \theta_0 = \rho_1 c_1 \sin \theta_1, \quad (2.1)$$

where ρ_n and c_n are the density and sound speed of layer n . If the surface is rough then the scattered and transmitted energy are re-distributed over all angles, with a main lobe at the specular direction and several side lobes. This redistribution has implications in terms of volume scattering, because the energy transmitted into layer 1 will “illuminate” the scatterers at multiple angles of incidence.

ii) Multiple layers (Fig. 2.2 (a)): when the environment consists of multiple layers, the acoustic energy undergoes multiple reflections between the boundaries, and each reflection will initiate scattering events that contribute to the total volume scattering.

iii) Discrete scatterers within the sediment: as mentioned before, scattering

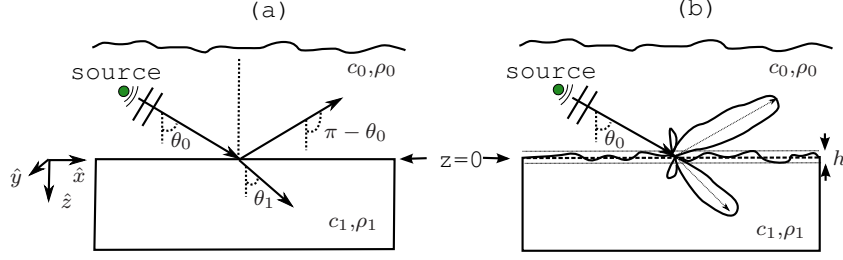


Figure 2.1: (a) In a perfectly smooth surface, part of the energy is reflected at the specular angle and part is transmitted according to (2.1); (b) When the surface is rough, the energy in the specular direction is reduced and re-distributed in a main lobe and side lobes.

takes place only in heterogeneous media, when a propagating wave encounters media with different acoustic properties (sound speed, density) than the background media. In the case of a single scatterer S_1 embedded in sand (Fig. 2.2 (b)), this acoustic contrast is abrupt. In the far field, the scattered field is a spherical wave of the form $\Psi_s = f(\theta, \phi)(e^{ikR}/R)$, where $f(\theta, \phi)$ is the *scattering function* that depends on the geometry of S_1 .

iv) Gradients in the acoustic impedance (Fig. 2.2 (c)): in unconsolidated sediments, it is possible to find smooth variations in the sound speed and/or the density as a function of the depth. This gradient in the acoustic impedance results in refraction of the propagating wave according to (2.1). Part of the refracted energy can couple back into the water column and it is perceived as volume scattering.

One additional complication is introduced by the nature of acoustic waves in elastic media: when a wave propagates in liquid media, only longitudinal

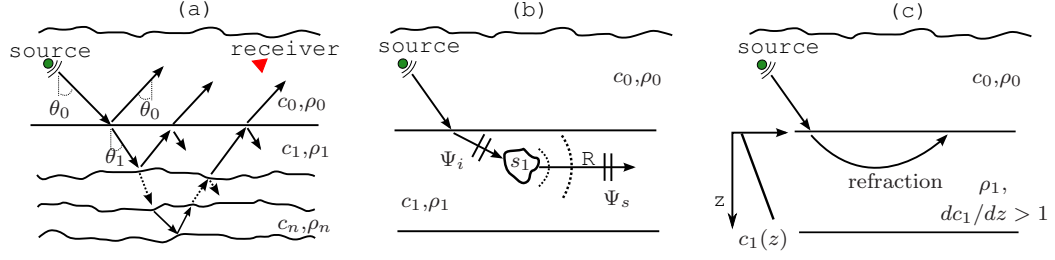


Figure 2.2: Scattering mechanisms in the ocean sea bed: (a) *Multiple-layers* contribute to the total volume scattering by redirecting coherent energy to interact multiple times with scatterers in the layers. (b) *Single scatterers* are regions within the layers where the acoustic impedance $Z_n = \rho_n c_n$ has an abrupt change. (c) *Refraction* due to gradients in the sound speed and/or the density is considered a form of volume scattering, because it can transport energy back to the water column.

waves (those in which the particles of the media oscillate in the same direction as the wave) are supported. But in solid or semi-solid media such as solid rock or fluid-saturated sediment, shear waves (i.e. the particles in the media have a perpendicular movement with respect to the direction of propagation, analogous to electromagnetic waves) are also supported. Therefore, a rigorous scattering formulation should consider all sub-bottom layers as elastic media.

Ideally, a model for ocean bottom scattering must account for all those effects in order to provide a faithful representation of the environment. However, at present there is no single unified model, and the literature shows a vast number of formulations that work only under particular assumptions.

2.2 Scattering from random media: definition of main quantities

Since volume scattering is the result of adding the contribution of multiple scatterers in the seabed, it is insightful to comment about scattering by a single particle surrounded by homogeneous media. This allows the definition of two quantities that are common to both classic and RT theory: the total scattering cross section σ_t and the scattering function $P(\hat{s}, \hat{s}')$, where \hat{s} and \hat{s}' represent outgoing and incoming directions. To give a specific example consider a scatterer with irregular shape being hit by an incident scalar plane wave¹ $\psi_i(r, \hat{n}_i)$ with direction of propagation \hat{n}_i

$$\psi_i(r, \hat{n}_i) = \psi_o e^{ikr}, \quad (2.2)$$

where $k = \omega/c$ is the wavenumber, ω is the frequency of the incident field in rad/s and c is the speed of propagation (i.e. $c = 3 \times 10^8$ m/s for electromagnetic fields or $c = 1500$ m/s for underwater acoustic fields). In the far field, the scattered field in the direction \hat{n}_s approximates a spherical wave of the form

$$\psi_s(r, \hat{n}_s) = \psi_o f(\hat{n}_i, \hat{n}_s) e^{ikR}/R, \quad (2.3)$$

¹Note that in general, the incident field does NOT have to be a plane wave. The plane wave case is used in this example because it is the most simple case.

where $f(\hat{n}_i, \hat{n}_s)$ contains the amplitude and phase of the scattered wave. The power per unit area carried by the incident plane wave is $P_i = |\psi_o|^2$ (W/m²). Likewise, the power per unit area per unit solid angle carried by the scattered spherical wave is $P_o = |\psi_o|^2 |f(\hat{n}_i, \hat{n}_s)|^2 / R^2$ (Wm⁻²Sr⁻¹), where *Sr* stands for *steradian*, the SI unit of solid angles. The differential scattering cross section gives a measure of the power “captured” by the scatterer and radiated into the direction of observation:

$$\sigma_d(\hat{n}_i, \hat{n}_s) = \lim_{R \rightarrow 0} R^2 \frac{P_s}{P_i} = |f(\hat{n}_i, \hat{n}_s)|^2; \quad (\text{m}^2/\text{Sr}). \quad (2.4)$$

The scattering cross section is the collection of the energy captured by the scatterer and re-radiated in all directions, so

$$\kappa_s = \int_{4\pi} \sigma_d(\hat{n}_i, \hat{n}_s) d\Omega = \int_{4\pi} |f(\hat{n}_i, \hat{n}_s)|^2 d\Omega; \quad (\text{m}^2) \quad (2.5)$$

where $\int_{4\pi} \cdot d\Omega = \int_0^\pi \int_0^{2\pi} \sin \theta d\theta d\phi$ is a double integral over a solid angle of 4π .

Finally, the function $P(\hat{n}_i, \hat{n}_s)$ is defined as

$$P(\hat{n}_i, \hat{n}_s) = 4\pi \sigma_d(\hat{n}_i, \hat{n}_s). \quad (2.6)$$

The extinction cross section σ_t is a measurement of how much energy is removed from the wave as it propagates through the medium. This energy can be removed either by scattering into other directions or by absorption (i.e. energy is dissipated as heat). The extinction cross section includes both effects and is defined as:

$$\sigma_t = \kappa_s + \nu, \tag{2.7}$$

where ν represents the absorption cross section of a single scatterer.

The quantities and concepts introduced in this section are required when dealing with transport theory or classic scattering models. The scattering cross section is a standard definition that can be utilized to compare experimental results to simulated results from any scattering model, and it will be mentioned again in sections 3.5 and 5.

2.3 Classic approach to scattering from random media

As an example of the classic approach to model acoustic scattering from random media, this section overviews the *integral method*, which is the starting point of most scattering models currently used.

The integral method consists of writing the wave equation with the density and sound speed as functions of the position within the media. Several models currently used to predict volume scattering are based on this technique (see [17,

18, 19] for example), and therefore it will be suitable for comparison with the results obtained from the proposed RT model.

To develop this section, consider a volume of background material with constant sound speed c_1 and constant density ρ_1 , and this material is mixed with scatterers of different sound speed (to simplify the expressions, it is assumed that the density of the scatterers is the same as ρ_1). Then, the sound speed in the volume is written as $c(\vec{r}) = c_o + \delta c(\vec{r})$, where c_o is the average sound speed of the mix (background+scatterers), and δc is a perturbation, that could be due to a smooth gradient ($\delta c/c_o \ll 1$) or due to a discrete scatterer ($\delta c/c_o \gg 1$). Then,

$$\left[\frac{1}{c(\vec{r})} \right]^2 = \frac{1}{c_o^2} + \frac{\epsilon}{c_o^2}; \quad (2.8)$$

where

$$\epsilon = \left[\frac{-2\delta c(\vec{r})}{c_o} \right]. \quad (2.9)$$

The wave equation for layer 1 can be written as [17]

$$\nabla^2 p(\vec{r}) + \frac{\omega^2}{c(\vec{r})^2} p(\vec{r}) = 0; \quad (2.10)$$

where ∇^2 is the Laplacian and

$$p(\vec{r}) = p_i(\vec{r}) + p_s(\vec{r}); \quad (2.11)$$

is the acoustic pressure at the position \vec{r} , given by the sum of the incident and the scattered pressure. Using (2.8), the wave equation can be written as an inhomogeneous wave equation:

$$\nabla^2 p(\vec{r}) + \frac{\omega^2}{c_o^2} p(\vec{r}) = -\frac{\epsilon^2}{c_o^2} \omega^2 p(\vec{r}); \quad (2.12)$$

and the solution method for this non-homogeneous equation usually requires approximations.

For a volume V containing the random scatterers, the solution of (2.12) is given by Green's theorem [20] as the convolution of the source term $\frac{\epsilon^2}{c_o^2} \omega^2 p(\vec{r})$ with the Green's function $G(\vec{r}, \vec{r}_o)$ ² as

$$p(\vec{r}) = \int_V G(\vec{r}, \vec{r}_o) p(\vec{r}_o) dV_o, \quad (2.13)$$

where \int_V is an integral on the volume containing the scatterers, and r_o is a vector

²The Green's function is the solution to the homogeneous wave equation. In this case, it is the solution of (2.12) in the absence of scatterers. For example, $G(r, r_o) = e^{i\omega|\vec{r}-\vec{r}_o|/c_o} / (4\pi|\vec{r}-\vec{r}_o|)$ for a single homogeneous media with no boundaries, and its complexity increases as layers are included [19].

that indicates the position of the differential volume dV_o . By looking at (2.13) the mathematical complexity of this method is clear: the unknown quantity $p(\vec{r})$ is also part of the integrand.

To overcome this problem, two approximations have been suggested[21]:

1. The small perturbation (Born) approximation: This method assumes that $\delta c/c_o \ll 1$, which means that the contrast of the scatterer with respect to the background is weak (i.e. the scatterer is very similar to the background medium), and therefore the scattered field is very small compared to the incident field. In this case, $p(\vec{r}_o) \approx p_i(\vec{r}_o)$ in the right side of (2.13).
2. The Rayleigh approximation: If the size of the scatterers is much less than the wavelength ($a \ll \lambda$), then it is possible to find algebraic expressions for the scattered field for certain scatterers with regular shape.

Note that both of the solution methods impose limits on the applicability of the model in order to obtain a mathematical tractable solution, but those approximations do not necessarily describe the random media.

2.4 Conclusion

A description of relevant acoustic scattering mechanisms commonly found in the seabed was provided, since this information is required to fully appreciate the capabilities of the proposed model. Then, the main concepts and quantities used

to describe the phenomena of scattering were introduced. Finally, an example of a classic approach to model scattering from random media was presented and its advantages and shortcomings were itemized.

Chapter 3

Radiative transfer model for elastic media

In this section, scattering from random media is explained from the perspective of transport theory, and the Radiative Transfer (RT) equation is obtained using heuristic arguments¹.

Transport theory is an alternative way to describe the propagation of energy through random media. Instead of using the acoustic field (magnitude and phase), transport theory provides equations for the *energy* carried by those fields. In this theory the main quantity is the *specific intensity*, which represents the “average power per unit area, per solid angle, per frequency”, as illustrated in Fig. 3.1.

In Fig. 3.1, $d\Omega$ is a differential solid angle represented as a cone or “energy pencil”, used to indicate a family of directions close to the unit vector \hat{s} . In spherical coordinates, $d\Omega = \sin\theta d\theta d\phi$, where θ is the elevation angle and ϕ is the azimuth angle.

¹The RT equation can also be formally derived from Twersky’s multiple scattering theory[11, 21], and this establishes the connection between transport theory and classic scattering theory.

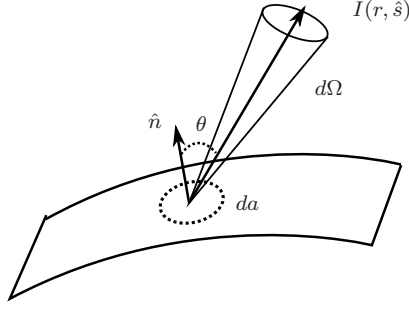


Figure 3.1: Definition of the specific intensity $I(r, \hat{s})$ as the energy that goes through a differential area da and within a differential solid angle $d\Omega$. The specific intensity forms an angle θ with the normal to the surface da .

The RT equation can be obtained from the conservation of energy in a differential volume containing random scatterers, as shown in Fig. 3.2. The specific intensity at the input of the differential volume located at the tip of vector $\vec{r} = |\vec{r}|\hat{s}$ is $I(\vec{r}, \hat{s})$. At the output of the differential volume the intensity $I(\hat{r} + d\hat{r}, \hat{s})$ (where $d\vec{r} = dr\hat{s}$) has changed due to scattering processes. The difference $I(\vec{r} + d\vec{r}, \hat{s}) - I(\vec{r}, \hat{s})$ represents the change in the energy that travels a distance dr in the direction of \hat{s} . This difference can be negative if energy has been lost due to absorption (lossy scatterers or lossy background media) or due to scattering of energy into directions other than \hat{s} (Fig. 3.2(a)). Also, the difference can be positive if energy has been “gained” due to scattering of energy from other particles outside the differential volume (Fig. 3.2(b)).

It can be stated that [22, 21]

$$\frac{\partial I(\vec{r}, \hat{s})}{\partial r} = -\eta\sigma_t I(\vec{r}, \hat{s}) + \frac{\eta}{4\pi} \int_{4\pi} P(\hat{s}, \hat{s}') I(\vec{r}, \hat{s}') d\Omega', \quad (3.1)$$

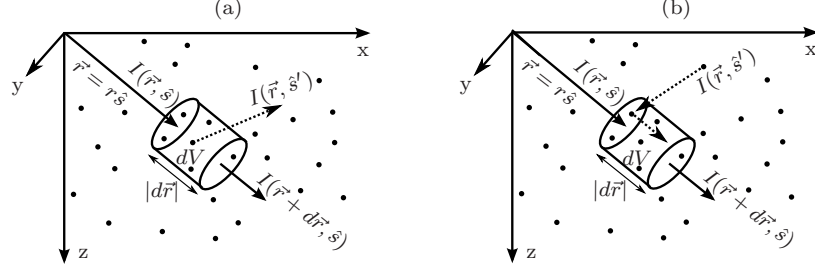


Figure 3.2: Change in the specific intensity $I(\vec{r}, \hat{s})$ when it propagates through a differential volume dV containing η scatterers/ m^3 : (a) Loss mechanism due to scattering of energy into direction \hat{s}' ; (b) Gain mechanism, due to coupling of energy from direction \hat{s}' into \hat{s} .

where η is the concentration of scatterers (scatterers/ m^3), σ_t is the total scattering cross section of a single scatterer and $P(\hat{s}, \hat{s}')$ represents the scattering of energy in the direction \hat{s} due to the incident intensity $I(\vec{r}, \hat{s}')$ coming from other scatterers outside dV . Note that σ_t and $P(\hat{s}, \hat{s}')$ are properties of the scatterers as mentioned in section 2.2, and they depend on the size, orientation, shape, acoustic impedance of the scatterer, and frequency of the excitation signal. Some general observations about the RT equation (3.1) are:

1. $\eta\sigma_t$ has units of scatterer per meter. This product represents the number of scatterers that interact with the intensity while it travels from \vec{r} to $\vec{r} + d\vec{r}$.
2. The double integral represents the collection of energy coming from all directions \hat{s}' and coupling into the direction of observation \hat{s} . The “coupling factor” that determines how much energy is distributed over each angle is $P(\hat{s}, \hat{s}')$.

3. The double integral is known as the *multiple scattering* term, because it implies that the energy is scattered at least twice: first by scatterers outside the differential volume (giving rise to the incoming radiation $I(\vec{r}, \hat{s}')$) and then by scatterers within the differential volume.
4. If the multiple scattering is ignored, (3.1) has an analytical solution of the form $I(\vec{r}, \hat{s}) = I_o e^{-\eta \sigma_t r}$ (the so called Beer’s law, where I_o is the initial intensity), which means that the intensity decays exponentially as a function of the number of scatterers along the propagation path and its corresponding cross section. In Transport theory, this is known as the “single scattering solution”.
5. Equation (3.1) can be written in any coordinate system (spherical, Cartesian, cylindrical). In section 3.1, this equation will be re-written for the special case of parallel plane layers.

The next two sections introduce versions of (3.1) suitable for parallel plane layers.

3.1 Scalar radiative transfer

As mentioned in the opening statement, one of the main advantages of applying the RT formulation to the problem of ocean bottom scattering is that the geometry of the ocean is well described as parallel plane layers with embedded

scatterers. This is very similar to most of the problems in which the RT equation is used nowadays for electromagnetics remote sensing, and specific solution techniques for the RT equation in parallel-plane media have already been developed. This section introduces a version of (3.1) specifically suited for parallel-plane geometries with constant statistical properties along the x/y coordinates, as shown in Fig. 3.3. In ocean acoustics, it is customary to define the \hat{z} axis pointing down, with $z = 0$ m at the water-sediment interface.

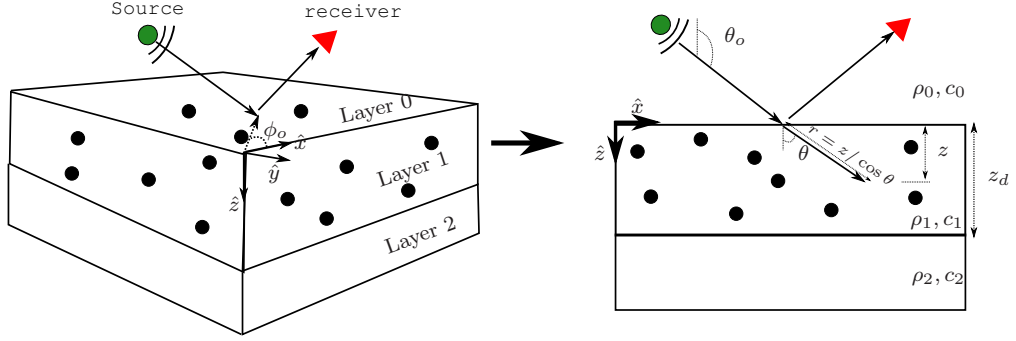


Figure 3.3: View of a parallel-plane scattering media in which the z axis points down and $z = 0$ m corresponds to the water-sediment interface. Since the statistical properties along the x/y coordinates are constant, the specific intensity depends only on the depth z and the direction, specified by the azimuth angle ϕ and the elevation angle θ , so $I(\vec{r}, \hat{s}) = I(z, \theta, \phi)$. Without loss of generality, it can be assumed the the azimuth of the incident radiation is zero ($\phi_o = 0$).

With the assumption of statistical independence in the x/y coordinates, the specific intensity $I(\vec{r}, \hat{s})$ only depends on z and the direction of propagation, which can be unambiguously specified by the azimuth angle ϕ measured with respect to the x axis and the elevation angle θ measured with respect to the z axis. With

the change of variable $r = z / \cos \theta$, (3.1) can be written as

$$\frac{\partial I(z, \theta, \phi)}{\partial z / \cos \theta} = -\eta \sigma_t I(z, \theta, \phi) + \frac{\eta}{4\pi} \int_{4\pi} P(\theta, \phi, \theta', \phi') . I(z, \theta', \phi') d\Omega' \quad (3.2)$$

In most of the publications related to transport theory, the *optical distance* is defined as

$$\tau = \eta \sigma_t z, \quad (3.3)$$

so (3.2) results in

$$\mu \frac{\partial I(\tau, \theta, \phi)}{\partial \tau} = -I(\tau, \theta, \phi) + \frac{1}{4\pi \sigma_t} \int_{4\pi} P(\mu, \phi, \mu', \phi') I(\tau, \theta', \phi') d\Omega', \quad (3.4)$$

with $\mu = \cos \theta$. This equation together with the boundary conditions (BC) constitute the entire mathematical formulation. The BC for the layer 1 in Fig. 3.3 can be written as:

$$\begin{aligned} I(\tau = 0, \theta, \phi) &= R_{10}(\theta) I(\tau = 0, \pi - \theta, \phi) \quad 0 < \theta < \pi/2; \\ I(\tau = \tau_d, \pi - \theta, \phi) &= R_{12}(\theta) I(\tau = \tau_d, \theta, \phi) \quad 0 < \theta < \pi/2; \end{aligned} \quad (3.5)$$

where $R_{10}(\theta)$ and $R_{12}(\theta)$ are the angle-dependent reflection coefficients between layer 0 and layer 1 and between layer 1 and layer 2, respectively.

3.2 Vector radiative transfer

Contrary to fluid media, elastic media such as consolidated sediments support three kinds of polarization of acoustic waves: shear vertical, shear horizontal and longitudinal. These polarizations are orthogonal to each other, which means that the total power carried by an acoustic wave can be found by adding the contribution of the three polarizations. In this section, (3.4) is modified to include the effects of polarization by using the Stoke's parameters for acoustic waves². The material in this section follows the adaptation of the RT formulation to acoustics presented by Turner et al [13]³.

3.2.1 Statement of the equation and boundary conditions

Figure 3.4 shows three cases in which a scatterer surrounded by elastic media is hit by a propagating wave. If the incident wave has longitudinal polarization, the scattered wave can have longitudinal, shear vertical and shear horizontal polarizations with magnitude proportional to $P_{LL}(\mu, \phi; \mu', \phi')$, $P_{yL}(\mu, \phi; \mu', \phi')$ and $P_{xL}(\mu, \phi; \mu', \phi')$, respectively. The terms $P_{ab}(\mu, \phi; \mu', \phi')$ are the equivalent to $P(\mu, \phi, \mu', \phi')$ in (3.4), but they include the conversion from polarization a into

²See appendix A for a definition of the Stoke's parameters for acoustics.

³Turner et al have suggested the use of the RT theory for ultrasound applications in unbounded media with steady excitations [13], and they extended the formulation to semi infinite media[14] with pulsed excitations[15]. Solution for a finite layer with reflective boundaries is developed in this section, and using this formulation for ocean bottom scattering is suggested in this work for the first time.

polarization b , with $\{a, b, c\} \in \{x, y, L\}$.

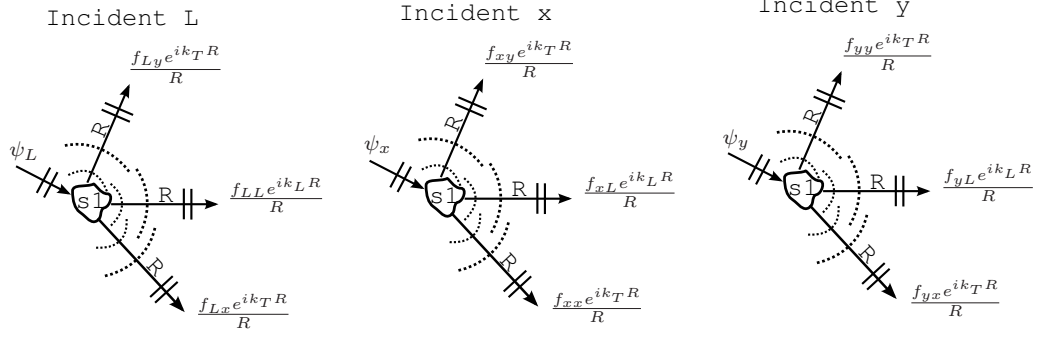


Figure 3.4: Partition of energy in longitudinal, shear vertical and shear horizontal polarizations for incident waves with different polarization. As in the scalar case presented in section 2.2, $P_{ab} = 4\pi|f_{ab}|^2$. Note that longitudinal scattered waves propagate with a wavenumber $k_L = \omega/c_L$ while transversal waves propagate with wavenumber $k_T = \omega/c_T$, where c_L and c_T are the sound speed for longitudinal and shear waves, respectively.

The partition of energy into transversal (x or y) and longitudinal (L) waves leads to the definition of two sets of scattering and absorption cross sections. Similar to (2.5) for the scalar case, the longitudinal and transversal scattering cross sections are

$$\begin{aligned}\kappa_L &= \frac{1}{4\pi} \int_{4\pi} [P_{LL} + P_{Ly} + P_{Lx}] d\Omega' \\ \kappa_T &= \frac{1}{8\pi} \int_{4\pi} [P_{yL} + P_{yy} + P_{yx} + P_{xyL} + P_{xy} + P_{xx}] d\Omega'\end{aligned}\tag{3.6}$$

and the extinction cross section for longitudinal and transversal waves are

$$\sigma_L = \kappa_L + \nu_L\tag{3.7}$$

$$\sigma_T = \kappa_T + \nu_T$$

where ν_L and ν_T are the absorption terms corresponding to longitudinal and transverse polarization, respectively.

Due to orthogonality, an equation similar to (3.4) can be written for each of the Stoke's parameters. For example, the RT equation for the longitudinal component is

$$\begin{aligned}
\mu \frac{\partial I_L(\mu, \phi, z)}{\partial z} = & -\eta \sigma_L I_L(\mu, \phi, z) + \\
\frac{\eta}{4\pi} \int_{-1}^1 \int_0^{2\pi} [& P_{LL}(\mu, \phi; \mu', \phi') I_L(\mu', \phi', z) \\
& + P_{Ly}(\mu, \phi; \mu', \phi') I_y(\mu', \phi', z) \\
& + P_{Lx}(\mu, \phi; \mu', \phi') I_x(\mu', \phi', z) \\
& + P_{LU}(\mu, \phi; \mu', \phi') U(\mu', \phi', z) \\
& + P_{LV}(\mu, \phi; \mu', \phi') V(\mu', \phi', z)] d\mu' d\phi',
\end{aligned} \tag{3.8}$$

and a similar equation can be written for I_y, I_x, U and V . By defining the vector

$$\underline{I}(\mu, \phi, \tau) = \begin{pmatrix} I_L \\ I_y \\ I_x \\ U \\ V \end{pmatrix}, \tag{3.9}$$

the vector RT equation can be written as

$$\mu \frac{\partial \underline{I}(\mu, \phi, \tau)}{\partial \tau} = -\underline{\tilde{\sigma}} \underline{I}(\mu, \phi, \tau) + \frac{1}{4\pi\kappa_T} \int_{-1}^1 \int_0^{2\pi} \underline{P}(\mu, \phi; \mu', \phi') \underline{I}(\mu', \phi', \tau) d\mu' d\phi', \quad (3.10)$$

where $\tau = \eta\kappa_T z$ and

$$\underline{\tilde{\sigma}} = \begin{pmatrix} \tilde{\sigma}_L & 0 & 0 & 0 & 0 \\ 0 & \tilde{\sigma}_T & 0 & 0 & 0 \\ 0 & 0 & \tilde{\sigma}_T & 0 & 0 \\ 0 & 0 & 0 & \tilde{\sigma}_T & 0 \\ 0 & 0 & 0 & 0 & \tilde{\sigma}_T \end{pmatrix}, \quad (3.11)$$

with $\tilde{\sigma}_L = \sigma_L/\kappa_L$ and $\tilde{\sigma}_T = \sigma_T/\kappa_L$. The term $\underline{P}(\mu, \phi; \mu', \phi')$ is the 5x5 Mueller matrix [13] for a single scatterer:

$$\underline{P}(\mu, \phi; \mu', \phi') = \begin{pmatrix} P_{LL} & P_{Ly} & P_{Lx} & P_{LU} & P_{LV} \\ P_{yL} & P_{yy} & P_{yx} & P_{yU} & P_{yV} \\ P_{xL} & P_{xy} & P_{xx} & P_{xU} & P_{xV} \\ P_{UL} & P_{Uy} & P_{Ux} & P_{UU} & P_{UV} \\ P_{VL} & P_{Vy} & P_{Vx} & P_{VU} & P_{VV} \end{pmatrix}, \quad (3.12)$$

where the angular dependence of the elements in the matrix $\underline{P}(\mu, \phi; \mu', \phi')$ has

been suppressed for brevity.

For a finite layer of thickness z_b and reflecting boundaries, the elastic boundary conditions are defined as

$$\begin{aligned} \underline{I}(\mu > 0, \phi, 0^+) &= \underline{I}_{src} + \underline{I}_{10}(\mu > 0, \phi, 0^+) \quad z = 0^+, \text{ downward} \\ \underline{I}(\mu < 0, \phi, \tau_b^-) &= \underline{I}_{12}(\mu < 0, \phi, \tau_b^-) \quad z = z_b^-, \text{ upward} \end{aligned} \quad (3.13)$$

where

$$\underline{I}_{src}(\mu, \phi, 0^+) = \begin{bmatrix} \hat{T}_{01}^{LL} K_{L0} \delta(\theta - \theta_1^{L1}) \\ \hat{T}_{01}^{Ly} K_{L0} \delta(\theta - \theta_1^{y1}) \\ 0 \\ 0 \\ 0 \end{bmatrix}, \quad (3.14)$$

results from the coupling of energy from the water column into the sediment.

The parameter K_{L0} is the amplitude of the incident specific intensity at $z = 0$ due to an acoustic source in the water column. It is assumed to be a collimated beam in the direction (θ_o^{L1}, ϕ_o) and it refracts into longitudinal and shear specific intensities within the sediment, with amplitude determined by the specific intensity transmission coefficients \hat{T}_{01}^{LL} (longitudinal-to-longitudinal) and \hat{T}_{01}^{Ly} (longitudinal-to-shear vertical); there is no longitudinal-to-shear horizontal coupling, so $\hat{T}_{01}^{Lx} = 0$. As a convention, the superscript in the reflection/transmission coefficients indicates the change in polarization and the subscript indicates the

layers at the interface.

The angles of the refracted waves are indicated by $\mu_1^{L_1} = \cos \theta_1^{L_1}$ and $\mu_1^{y_1} = \cos \theta_1^{y_1}$, where the subscript corresponds to the layer and the superscript has been introduced to indicate whether the angle describes a longitudinal or a shear vertical intensity. As explained later, multiple interactions of the intensity with the boundaries of the layer result in the alignment of the coherent intensity along several directions of propagation, which are indicated with a numerical value in the super index. For example, $\theta_1^{L_1}$ and $\theta_1^{L_2}$ correspond both to longitudinal coherent intensities in layer 1, traveling in two different angles that are labeled as L_1 and L_2 . Similarly, $\theta_1^{y_1}$ and $\theta_1^{y_2}$ are shear vertical coherent intensities in layer 1.

The vectors \underline{I}_{10} and \underline{I}_{12} are the reflected specific intensities at $\tau = 0$ and

$\tau = \tau_b$, respectively, and are defined as

$$\underline{I}_{10}(\mu > 0, \phi, 0^+) = \begin{bmatrix} \hat{R}_{10}^{LL} I_L(-\mu, \phi, 0^+) + \hat{R}_{10}^{yL} I_y(-\mu_1^{yA}, \phi, 0^+) \\ \hat{R}_{10}^{Ly} I_L(-\mu_1^{LA}, \phi, 0^+) + \hat{R}_{10}^{yy} I_y(-\mu, \phi, 0^+) \\ I_x(-\mu, \phi, 0^+) \\ \hat{R}_{10}^{UU} I_U(-\mu, \phi, 0^+) + \hat{R}_{10}^{VU} I_V(-\mu, \phi, 0^+) \\ \hat{R}_{10}^{UV} I_U(-\mu, \phi, 0^+) + \hat{R}_{10}^{VV} I_V(-\mu, \phi, 0^+) \end{bmatrix}, \quad (3.15)$$

$$\underline{I}_{12}(\mu < 0, \phi, \tau_b^-) = \begin{bmatrix} \hat{R}_{12}^{LL} I_L(-\mu, \phi, \tau_b^-) + \hat{R}_{12}^{yL} I_y(\mu_1^{yA}, \phi, \tau_b^-) \\ \hat{R}_{12}^{Ly} I_L(\mu_1^{LA}, \phi, \tau_b^-) + \hat{R}_{12}^{yy} I_y(-\mu, \phi, \tau_b^-) \\ I_x(-\mu, \phi, \tau_b^-) \\ \hat{R}_{12}^{UU} I_U(-\mu, \phi, \tau_b^-) + \hat{R}_{12}^{VU} I_V(-\mu, \phi, \tau_b^-) \\ \hat{R}_{12}^{UV} I_U(-\mu, \phi, \tau_b^-) + \hat{R}_{12}^{VV} I_V(-\mu, \phi, \tau_b^-) \end{bmatrix}, \quad (3.16)$$

where \hat{R}_{cd}^{ab} is the reflection coefficient for an incident wave with polarization a into a wave with polarization b at the boundary between media c and d . The variables $\mu_1^{LA} = \cos \theta_1^{LA}$ and $\mu_1^{yA} = \cos \theta_1^{yA}$ indicate off-axis contribution due to conversion from longitudinal and shear vertical polarizations, and are defined as:

$$\begin{aligned} \theta_1^{LA} &= \sin^{-1} \left(\frac{c_{L1}}{c_{T1}} \sin \theta \right); & \theta_1^{yA} &= \sin^{-1} \left(\frac{c_{T1}}{c_{L1}} \sin \theta \right); \\ \theta &= \cos^{-1} |\mu|. \end{aligned} \tag{3.17}$$

Notice that for the vector RT equation, each layer n is characterized by a longitudinal sound speed c_{Ln} and a transversal sound speed c_{Tn} , in addition to the density ρ_n .

Solution of (3.10) subject to the BC in (3.13) will be discussed in section 3.2.4.

3.2.2 The reduced intensity for a finite layer

In transport theory, the reduced intensity takes the form of the incident specific intensity [13], but it is attenuated according to the concentration of scatterers, the extinction coefficient and the attenuation of the background media, as explained below. For the general case of a finite layer with reflecting boundaries, the reduced intensity has upward and downward components [23]. Due to the refraction of longitudinal waves into shear waves and vice versa, the resulting reduced intensity can be collimated along eight different angles, as shown in

Fig. 3.5.

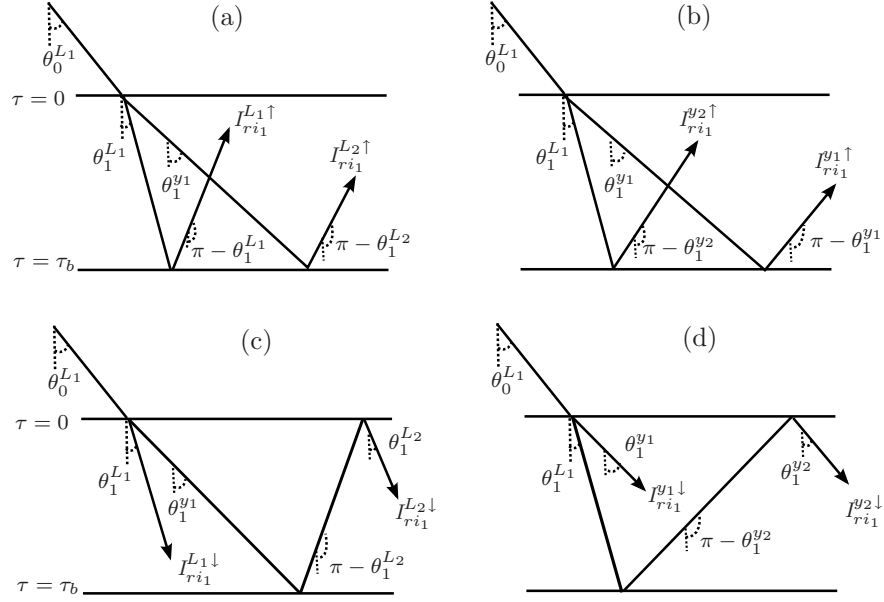


Figure 3.5: The reduced intensity can be collimated in 8 different directions: (a) The upward longitudinal intensities $I_{ri_1}^{L_1 \uparrow}$ and $I_{ri_1}^{L_2 \uparrow}$ result from the transformations L-L-L and L-y-L, respectively, where L stands for *longitudinal* and y for *shear vertical*; (b) Similar to (a) for $I_{ri_1}^{y_1 \uparrow}$ (L-y-y) and $I_{ri_1}^{y_2 \uparrow}$ (L-L-y); (c) The downward longitudinal intensities $I_{ri_1}^{L_1 \downarrow}$ and $I_{ri_1}^{L_2 \downarrow}$ correspond to the transformations L-L and L-y-L-L, respectively; (d) Similar to (c) for $I_{ri_1}^{y_1 \downarrow}$ (L-y) and $I_{ri_1}^{y_2 \downarrow}$ (L-L-y-y).

Each diagram in Fig. 3.5 represents a possible combination of multiple reflections of the energy within the sediment. The notation for the reduced intensity is similar to the notation for angles in (3.14): the subindex ri_1 stands for *reduced intensity in layer 1*, and the super indexes $L_1 \downarrow$ and $L_2 \downarrow$ stand for downward longitudinal intensities collimated along two different angles (L_1 and L_2 respectively), and a similar interpretation applies to the other terms. A closed form expression for each combination of multiple reflections can be found by writing an

infinite summation of terms and simplifying the resulting geometric series. For example, for multiple reflections with no conversion of polarization, the upward longitudinal and vertical shear reduced intensities can be written as [23]:

$$I_{ri_1}^{L_1\uparrow}(\mu, \phi, \tau) = \frac{K_{L0} \hat{T}_{01}^{LL} \hat{R}_{12}^{LL}}{1 - \hat{R}_{12}^{LL} \hat{R}_{01}^{LL} e^{2\tilde{\sigma}_L \tau_b / \mu}} e^{2\tilde{\sigma}_L \tau_b / \mu} e^{-\tilde{\sigma}_L \tau / \mu} \delta(\theta - (\pi - \theta_1^{L_1})) \delta(\phi - \phi_o); \quad (3.18)$$

$$I_{ri_1}^{y_1\uparrow}(\mu, \phi, \tau) = \frac{K_{L0} \hat{T}_{01}^{Ly} \hat{R}_{12}^{yy}}{1 - \hat{R}_{12}^{yy} \hat{R}_{01}^{yy} e^{2\tilde{\sigma}_T \tau_b / \mu}} e^{2\tilde{\sigma}_T \tau_b / \mu} e^{-\tilde{\sigma}_T \tau / \mu} \delta(\theta - (\pi - \theta_1^{y_1})) \delta(\phi - \phi_o).$$

If $\tilde{\sigma}_L \tau_b, \tilde{\sigma}_T \tau_b \gg 1$, there is significant scattering and absorption within the layer so multiple bounces can be ignored. The simplified expressions for the upward intensities in layer 1 become:

$$\begin{aligned} I_{ri_1}^{L_1\uparrow}(\mu, \phi, \tau) &= A_1^{L_1\uparrow}(\mu) e^{-\tilde{\sigma}_L \tau / \mu} \delta(\theta - (\pi - \theta_1^{L_1})) \delta(\phi - \phi_o); \\ I_{ri_1}^{L_2\uparrow}(\mu, \phi, \tau) &= A_1^{L_2\uparrow}(\mu) e^{-\tilde{\sigma}_L \tau / \mu} \delta(\theta - (\pi - \theta_1^{L_2})) \delta(\phi - \phi_o); \\ I_{ri_1}^{y_1\uparrow}(\mu, \phi, \tau) &= A_1^{y_1\uparrow}(\mu) e^{-\tilde{\sigma}_T \tau / \mu} \delta(\theta - (\pi - \theta_1^{y_1})) \delta(\phi - \phi_o); \\ I_{ri_1}^{y_2\uparrow}(\mu, \phi, \tau) &= A_1^{y_2\uparrow}(\mu) e^{-\tilde{\sigma}_T \tau / \mu} \delta(\theta - (\pi - \theta_1^{y_2})) \delta(\phi - \phi_o); \end{aligned} \quad (3.19)$$

where

$$\begin{aligned}
A_1^{L_1\uparrow}(\mu) &= K_{L0} \hat{T}_{01}^{LL} \hat{R}_{12}^{LL} \exp\left[\frac{2\tilde{\sigma}_L \tau_b}{\mu}\right]; \\
A_1^{L_2\uparrow}(\mu) &= K_{L0} \hat{T}_{01}^{Ly} \hat{R}_{12}^{yL} \exp\left[-\tau_b \left(\frac{\tilde{\sigma}_T}{\mu_1^{y1}} - \frac{\tilde{\sigma}_L}{\mu}\right)\right]; \\
A_1^{y_1\uparrow}(\mu) &= K_{L0} \hat{T}_{01}^{Ly} \hat{R}_{12}^{yy} \exp\left[\frac{2\tilde{\sigma}_T \tau_b}{\mu}\right]; \\
A_1^{y_2\uparrow}(\mu) &= K_{L0} \hat{T}_{01}^{LL} \hat{R}_{12}^{Ly} \exp\left[-\tau_b \left(\frac{\tilde{\sigma}_L}{\mu_1^{L1}} - \frac{\tilde{\sigma}_T}{\mu}\right)\right];
\end{aligned} \tag{3.20}$$

are the amplitude terms. Similarly, the expressions for the downward reduced intensities are:

$$\begin{aligned}
I_{ri_1}^{L_1\downarrow}(\tau, \mu, \phi) &= A_1^{L_1\downarrow}(\mu) e^{-\tilde{\sigma}_L \tau / \mu} \delta(\theta - \theta_1^{L_1}) \delta(\phi - \phi_o); \\
I_{ri_1}^{L_2\downarrow}(\tau, \mu, \phi) &= A_1^{L_2\downarrow}(\mu) e^{-\tilde{\sigma}_L \tau / \mu} \delta(\theta - \theta_1^{L_2}) \delta(\phi - \phi_o); \\
I_{ri_1}^{y_1\downarrow}(\tau, \mu, \phi) &= A_1^{y_1\downarrow}(\mu) e^{-\tilde{\sigma}_T \tau / \mu} \delta(\theta - \theta_1^{y_1}) \delta(\phi - \phi_o); \\
I_{ri_1}^{y_2\downarrow}(\tau, \mu, \phi) &= A_1^{y_2\downarrow}(\mu) e^{-\tilde{\sigma}_T \tau / \mu} \delta(\theta - \theta_1^{y_2}) \delta(\phi - \phi_o);
\end{aligned} \tag{3.21}$$

where

$$\begin{aligned}
A_1^{L_1\downarrow}(\mu) &= K_{L0} \hat{T}_{01}^{LL}; \\
A_1^{L_2\downarrow}(\mu) &= K_{L0} \hat{T}_{01}^{Ly} \hat{R}_{12}^{yL} \hat{R}_{11}^{LL} \exp\left[-\tau_b \left(\frac{\tilde{\sigma}_T}{\mu_1^{y1}} + \frac{\tilde{\sigma}_L}{\mu}\right)\right]; \\
A_1^{y_1\downarrow}(\mu) &= K_{L0} \hat{T}_{01}^{Ly}; \\
A_1^{y_2\downarrow}(\mu) &= K_{L0} \hat{T}_{01}^{LL} \hat{R}_{12}^{Ly} \hat{R}_{11}^{yy} \exp\left[-\tau_b \left(\frac{\tilde{\sigma}_L}{\mu_1^{L1}} + \frac{\tilde{\sigma}_T}{\mu}\right)\right].
\end{aligned} \tag{3.22}$$

The variables $\mu_1^{L_1}, \mu_1^{y_1}, \mu_1^{L_2}, \mu_1^{y_2}$ are the cosine of the angles

$$\theta_1^{L_1} = \sin^{-1} \left[\frac{c_{L1}}{c_{L0}} \sin \theta_0^{L_1} \right]; \quad \theta_1^{y_1} = \sin^{-1} \left[\frac{c_{T1}}{c_{L0}} \sin \theta_0^{L_1} \right]; \quad (3.23)$$

$$\theta_1^{L_2} = \sin^{-1} \left[\frac{c_{L1}}{c_{T1}} \sin \theta_1^{y_1} \right]; \quad \theta_1^{y_2} = \sin^{-1} \left[\frac{c_{T1}}{c_{L1}} \sin \theta_1^{L_1} \right];$$

where c_{La} and c_{Ta} are the longitudinal and shear sound speed in the a^{th} layer, respectively.

3.2.3 The vector RT equation for diffuse intensity with multiple coherent sources

The procedure for solving (3.10) consists of writing the total specific intensity as the summation of the reduced and the diffuse intensity:

$$\underline{I}(\mu, \phi, \tau) = \underline{I}_{ri}(\mu, \phi, \tau) + \underline{I}_d(\mu, \phi, \tau), \quad (3.24)$$

where

$$\underline{I}_{ri}(\mu, \phi, \tau) = \begin{bmatrix} I_{ri_1}^{L_1\downarrow}(\mu, \phi, \tau) + I_{ri_1}^{L_2\downarrow}(\mu, \phi, \tau) + I_{ri_1}^{L_1\uparrow}(\mu, \phi, \tau) + I_{ri_1}^{L_2\uparrow}(\mu, \phi, \tau) \\ I_{ri_1}^{y_1\downarrow}(\mu, \phi, \tau) + I_{ri_1}^{y_2\downarrow}(\mu, \phi, \tau) + I_{ri_1}^{y_1\uparrow}(\mu, \phi, \tau) + I_{ri_1}^{y_2\uparrow}(\mu, \phi, \tau) \\ 0 \\ 0 \\ 0 \end{bmatrix}; \quad (3.25)$$

and

$$\underline{I}_d(\mu, \phi, \tau) = \begin{bmatrix} I_{d_1}^L(\mu, \phi, \tau) \\ I_{d_1}^y(\mu, \phi, \tau) \\ I_{d_1}^x(\mu, \phi, \tau) \\ I_{d_1}^U(\mu, \phi, \tau) \\ I_{d_1}^V(\mu, \phi, \tau) \end{bmatrix}; \quad (3.26)$$

is the vector of diffuse intensities to be found. Note that for any specific angle μ only one term in the sum (3.25) will be non-zero due to the δ functions in (3.19) and (3.21). Substitution of (3.24) into (3.10) results in an expression for

$\underline{I}_d(\mu, \phi, \tau)$ with sources of longitudinal and transversal specific intensity:

$$\begin{aligned}
\mu \frac{\partial \underline{I}_d(\mu, \phi, \tau)}{\partial \tau} = & -\tilde{\sigma} \underline{I}_d(\mu, \phi, \tau) + \\
\frac{1}{4\pi\kappa_T} \left[\int_{-1}^1 \int_0^{2\pi} \underline{P}(\mu, \phi; \mu', \phi') \underline{I}_d(\mu', \phi', \tau) d\mu' d\phi' \right] \\
& + \underline{S}_1^{L1\downarrow}(\mu, \phi) e^{-\frac{\tilde{\sigma} L_1^\tau}{\mu_1}} + \underline{S}_1^{L2\downarrow}(\mu, \phi) e^{-\frac{\tilde{\sigma} L_2^\tau}{\mu_1^2}} \\
& + \underline{S}_1^{y1\downarrow}(\mu, \phi) e^{-\frac{\tilde{\sigma} T_1^\tau}{\mu_1}} + \underline{S}_1^{y2\downarrow}(\mu, \phi) e^{-\frac{\tilde{\sigma} T_2^\tau}{\mu_1^2}} \\
& + \underline{S}_1^{L1\uparrow}(\mu, \phi) e^{\frac{\tilde{\sigma} L_1^\tau}{\mu_1}} + \underline{S}_1^{L2\uparrow}(\mu, \phi) e^{\frac{\tilde{\sigma} L_2^\tau}{\mu_1^2}} \\
& + \underline{S}_1^{y1\uparrow}(\mu, \phi) e^{\frac{\tilde{\sigma} T_1^\tau}{\mu_1}} + \underline{S}_1^{y2\uparrow}(\mu, \phi) e^{\frac{\tilde{\sigma} T_2^\tau}{\mu_1^2}},
\end{aligned} \tag{3.27}$$

where

$$\underline{S}_1^{L1\downarrow}(\mu, \phi) = \frac{1}{4\pi\kappa_T} \underline{P}(\mu, \phi; \mu_1^{L1}, \phi_o) \begin{pmatrix} A_1^{L1\downarrow}(\mu_1^{L1}) \\ 0 \\ 0 \\ 0 \\ 0 \end{pmatrix}; \tag{3.28}$$

$$\underline{S}_1^{L2\downarrow}(\mu, \phi) = \frac{1}{4\pi\kappa_T} \underline{P}(\mu, \phi; \mu_1^{L2}, \phi_o) \begin{pmatrix} A_1^{L2\downarrow}(\mu_1^{L2}) \\ 0 \\ 0 \\ 0 \\ 0 \end{pmatrix}; \tag{3.29}$$

$$\underline{S}_1^{y_1\downarrow}(\mu, \phi) = \frac{1}{4\pi\kappa_T} \underline{P}(\mu, \phi; \mu_1^{y_1}, \phi_o) \begin{pmatrix} 0 \\ A_1^{y_1\downarrow}(\mu_1^{y_1}) \\ 0 \\ 0 \\ 0 \end{pmatrix}; \quad (3.30)$$

$$\underline{S}_1^{y_2\downarrow}(\mu, \phi) = \frac{1}{4\pi\kappa_T} \underline{P}(\mu, \phi; \mu_1^{y_2}, \phi_o) \begin{pmatrix} 0 \\ A_1^{y_2\downarrow}(\mu_1^{y_2}) \\ 0 \\ 0 \\ 0 \end{pmatrix}; \quad (3.31)$$

and the upward “source” terms $\underline{S}_1^{L_1\uparrow}(\mu, \phi)$, $\underline{S}_1^{L_2\uparrow}(\mu, \phi)$, $\underline{S}_1^{y_1\uparrow}(\mu, \phi)$ and $\underline{S}_1^{y_2\uparrow}(\mu, \phi)$ can be obtained from (3.28)-(3.31) by substituting “ \downarrow ” by “ \uparrow ” and $\mu_1^{a_b}$ by $-\mu_1^{a_b}$ in the phase matrix $\underline{P}(\mu, \phi; \mu_1^{a_b}, \phi_o)$.

For the diffuse intensity in (3.27) the same boundary conditions as in (3.15) and (3.16) can be used and the solution of the diffuse intensity is outlined in section 3.2.4.

3.2.4 Solution of the vector RT equation by Fourier Series and Gaussian Quadrature integration

This section presents a method of solution of the vector RT equation. It follows the method developed by Turner et al [13] and Ishimaru [21], but it is extended to the general case of a layer with arbitrary thickness τ_d and reflective top and bottom boundaries. This section contains a lot of matrix algebra steps that can be skipped by the reader. The most important result in this section is the expression in (3.54), because it allows computation of the specific intensity as a function of θ , ϕ and τ .

First, a Fourier azimuthal decomposition in $2M + 1$ terms is applied to the Mueller matrix and the specific intensity. The corresponding Fourier series representation is

$$\begin{aligned}\underline{P}_m(\mu, \mu_o) &= \frac{1}{2\pi} \int_0^{2\pi} \underline{P}(\mu, \mu_o, \phi - \phi_o) e^{im(\phi - \phi_o)} d(\phi - \phi_o); \\ \underline{I}_{dm}(\mu, \tau) &= \frac{1}{2\pi} \int_0^{2\pi} \underline{I}_d(\mu, \phi - \phi_o, \tau) e^{im(\phi - \phi_o)} d(\phi - \phi_o);\end{aligned}\tag{3.32}$$

which allows to write the source terms as

$$\underline{\mathbf{S}}_{1m}^{L_1\downarrow}(\mu) = \frac{1}{4\pi\kappa_T} \underline{\mathbf{P}}_m(\mu, \mu_1^{L_1}) \begin{pmatrix} A_1^{L_1\downarrow}(\mu_1^{L_1}) \\ 0 \\ 0 \\ 0 \\ 0 \end{pmatrix}, \quad (3.33)$$

for (3.28) and in a similar way for (3.29) through (3.31). The θ dependency can be simplified with the Gaussian Quadrature method by discretizing the variable θ in $2N$ angles. Equation (3.27) is transformed to⁴

$$\begin{aligned} \frac{\partial \mathbf{I}_{dm}(\tau)}{\partial \tau} + \mathbf{W}_m \mathbf{I}_{dm}(\tau) = & \mathbf{S}_{1m}^{L_1\downarrow} \exp\left[-\frac{\tilde{\sigma}_L \tau}{\mu_1^{L_1}}\right] + \mathbf{S}_{1m}^{L_2\downarrow} \exp\left[-\frac{\tilde{\sigma}_L \tau}{\mu_1^{L_2}}\right] \\ & + \mathbf{S}_{1m}^{y_1\downarrow} \exp\left[-\frac{\tilde{\sigma}_T \tau}{\mu_1^{y_1}}\right] + \mathbf{S}_{1m}^{y_2\downarrow} \exp\left[-\frac{\tilde{\sigma}_T \tau}{\mu_1^{y_2}}\right] \\ & + \mathbf{S}_{1m}^{L_1\uparrow} \exp\left[\frac{\tilde{\sigma}_L \tau}{\mu_1^{L_1}}\right] + \mathbf{S}_{1m}^{L_2\uparrow} \exp\left[\frac{\tilde{\sigma}_L \tau}{\mu_1^{L_2}}\right] \\ & + \mathbf{S}_{1m}^{y_1\uparrow} \exp\left[\frac{\tilde{\sigma}_T \tau}{\mu_1^{y_1}}\right] + \mathbf{S}_{1m}^{y_2\uparrow} \exp\left[\frac{\tilde{\sigma}_T \tau}{\mu_1^{y_2}}\right]; \end{aligned} \quad (3.34)$$

⁴Notice that the underscore is used to indicate vectors of five elements corresponding to the Stoke's parameters as in (3.9), while **bold face** is used for vectors of size $5 \times 2N$, which include all the elements of the gaussian quadrature discretization of the elevation angle θ .

where

$$\begin{aligned}
\mathbf{I}_{dm}(\tau) &= \begin{bmatrix} \underline{I}_{dm}(\mu_{-N}, \tau) \\ \underline{I}_{dm}(\mu_{-N+1}, \tau) \\ \cdot \\ \cdot \\ \underline{I}_{dm}(\mu_{N-1}, \tau) \\ \underline{I}_{dm}(\mu_N, \tau) \end{bmatrix}; \\
\mathbf{S}_{1m}^{(L_{1,2}/y_{1,2})(\uparrow, \downarrow)} &= \begin{bmatrix} \underline{S}_{1m}^{(L_{1,2}/y_{1,2})(\uparrow, \downarrow)}(\mu_{-N}) / \mu_{-N} \\ \underline{S}_{1m}^{(L_{1,2}/y_{1,2})(\uparrow, \downarrow)}(\mu_{-N+1}) / \mu_{-N+1} \\ \cdot \\ \cdot \\ \underline{S}_{1m}^{(L_{1,2}/y_{1,2})(\uparrow, \downarrow)}(\mu_{N-1}) / \mu_{N-1} \\ \underline{S}_{1m}^{(L_{1,2}/y_{1,2})(\uparrow, \downarrow)}(\mu_N) / \mu_N \end{bmatrix};
\end{aligned} \tag{3.35}$$

and \mathbf{W}_m is defined by Turner [13]. The solution to (3.34) consists of a particular solution for each of the eight sources and a homogeneous solution. The particular

solution is

$$\begin{aligned}
\mathbf{I}_{pm}(\tau) = & \mathbf{H}_{1m}^{L_1\downarrow} \exp\left[-\frac{\tilde{\sigma}_L\tau}{\mu_1^{L_1}}\right] + \mathbf{H}_{1m}^{L_2\downarrow} \exp\left[-\frac{\tilde{\sigma}_L\tau}{\mu_1^{L_2}}\right] \\
& + \mathbf{H}_{1m}^{y_1\downarrow} \exp\left[-\frac{\tilde{\sigma}_T\tau}{\mu_1^{y_1}}\right] + \mathbf{H}_{1m}^{y_2\downarrow} \exp\left[-\frac{\tilde{\sigma}_T\tau}{\mu_1^{y_2}}\right] \\
& + \mathbf{H}_{1m}^{L_1\uparrow} \exp\left[\frac{\tilde{\sigma}_L\tau}{\mu_1^{L_1}}\right] + \mathbf{H}_{1m}^{L_2\uparrow} \exp\left[\frac{\tilde{\sigma}_L\tau}{\mu_1^{L_2}}\right] \\
& + \mathbf{H}_{1m}^{y_1\uparrow} \exp\left[\frac{\tilde{\sigma}_T\tau}{\mu_1^{y_1}}\right] + \mathbf{H}_{1m}^{y_2\uparrow} \exp\left[\frac{\tilde{\sigma}_T\tau}{\mu_1^{y_2}}\right],
\end{aligned} \tag{3.36}$$

where

$$\begin{aligned}
\mathbf{H}_{1m}^{L_1\downarrow} &= \left(\mathbf{W}_m - \mathbf{D} \frac{\tilde{\sigma}_L}{\mu_1^{L_1}}\right)^{-1} \mathbf{S}_{1m}^{L_1\downarrow}, \\
\mathbf{H}_{1m}^{L_2\downarrow} &= \left(\mathbf{W}_m - \mathbf{D} \frac{\tilde{\sigma}_L}{\mu_1^{L_2}}\right)^{-1} \mathbf{S}_{1m}^{L_2\downarrow}, \\
\mathbf{H}_{1m}^{y_1\downarrow} &= \left(\mathbf{W}_m - \mathbf{D} \frac{\tilde{\sigma}_T}{\mu_1^{y_1}}\right)^{-1} \mathbf{S}_{1m}^{y_1\downarrow}, \\
\mathbf{H}_{1m}^{y_2\downarrow} &= \left(\mathbf{W}_m - \mathbf{D} \frac{\tilde{\sigma}_T}{\mu_1^{y_2}}\right)^{-1} \mathbf{S}_{1m}^{y_2\downarrow},
\end{aligned} \tag{3.37}$$

correspond to the downward source terms and

$$\begin{aligned}
\mathbf{H}_{1m}^{L_1\uparrow} &= \left(\mathbf{W}_m + \mathbf{D} \frac{\tilde{\sigma}_L}{\mu_1^{L_1}}\right)^{-1} \mathbf{S}_{1m}^{L_1\uparrow}, \\
\mathbf{H}_{1m}^{L_2\uparrow} &= \left(\mathbf{W}_m + \mathbf{D} \frac{\tilde{\sigma}_L}{\mu_1^{L_2}}\right)^{-1} \mathbf{S}_{1m}^{L_2\uparrow}, \\
\mathbf{H}_{1m}^{y_1\uparrow} &= \left(\mathbf{W}_m + \mathbf{D} \frac{\tilde{\sigma}_T}{\mu_1^{y_1}}\right)^{-1} \mathbf{S}_{1m}^{y_1\uparrow}, \\
\mathbf{H}_{1m}^{y_2\uparrow} &= \left(\mathbf{W}_m + \mathbf{D} \frac{\tilde{\sigma}_T}{\mu_1^{y_2}}\right)^{-1} \mathbf{S}_{1m}^{y_2\uparrow},
\end{aligned} \tag{3.38}$$

correspond to the upward terms, with \mathbf{D} as the $10N \times 10N$ identity matrix.

The homogeneous solution can be found by solving an eigenvalue problem (see [13]) with eigenvectors g_{mn} and eigenvalues λ_{mn} . The full solution for the m^{th} Fourier expansion term of the diffuse intensity is written as

$$\mathbf{I}_{dm}(\tau) = \mathbf{I}_{pm}(\tau) + \sum_{n=1}^{10N} C_{mn} g_{mn} e^{-\lambda_{mn}\tau}, \quad (3.39)$$

where the constants C_{mn} must be found from the boundary conditions.

The intensity vector \mathbf{I}_{dm} can be divided in upward intensity(\mathbf{I}_{dm}^+ , $\mu < 0$) and downward intensity(\mathbf{I}_{dm}^- , $\mu > 0$), and it is evaluated at $\tau = 0^+$ and $\tau = \tau_b^-$, so the top boundary condition $\mathbf{I}_{dm}^-(\tau = 0^+) = \hat{\mathbf{R}}_{10} \mathbf{I}_{dm}^+(\tau = 0^+)$ yields the equation

$$\sum_{n=1}^{10N} C_{mn} g_{mn}^- + \mathbf{I}_{pm}^-(0^+) = \hat{\mathbf{R}}_{10} \left(\sum_{n=1}^{10N} C_{mn} g_{mn}^+ + \mathbf{I}_{pm}^+(0^+) \right), \quad (3.40)$$

and the bottom boundary condition $\mathbf{I}_m^+(\tau_b^-) = \hat{\mathbf{R}}_{12} \mathbf{I}_m^-(\tau_b^-)$ yields

$$\begin{aligned} & \sum_{n=1}^{10N} C_{mn} g_{mn}^+ e^{-\lambda_{mn}\tau_b} + \mathbf{I}_{pm}^+(\tau_b) = \\ & \hat{\mathbf{R}}_{12} \left(\sum_{n=1}^{10N} C_{mn} g_{mn}^- e^{-\lambda_{mn}\tau_b} + \mathbf{I}_{pm}^-(\tau_b) \right), \end{aligned} \quad (3.41)$$

where

$$\hat{\mathbf{R}}_{10} = \begin{pmatrix} 0 & 0 & 0 & \dots & 0 & 0 & \hat{\underline{R}}_{10}(\mu_{-1}) \\ 0 & 0 & 0 & \dots & 0 & \hat{\underline{R}}_{10}(\mu_{-2}) & 0 \\ & & & & & \cdot & \\ & & & & & \cdot & \\ & & & & & \cdot & \\ 0 & \hat{\underline{R}}_{10}(\mu_{-N+1}) & 0 & 0 & 0 & 0 & 0 \\ \hat{\underline{R}}_{10}(\mu_{-N}) & 0 & 0 & 0 & 0 & 0 & 0 \end{pmatrix}; \quad (3.42)$$

$$\hat{\mathbf{R}}_{12} = \begin{pmatrix} 0 & 0 & 0 & \dots & 0 & 0 & \hat{\underline{R}}_{12}(\mu_N) \\ 0 & 0 & 0 & \dots & 0 & \hat{\underline{R}}_{12}(\mu_{N-1}) & 0 \\ & & & & & \cdot & \\ & & & & & \cdot & \\ & & & & & \cdot & \\ 0 & \hat{\underline{R}}_{12}(\mu_2) & 0 & 0 & 0 & 0 & 0 \\ \hat{\underline{R}}_{12}(\mu_1) & 0 & 0 & 0 & 0 & 0 & 0 \end{pmatrix}; \quad (3.43)$$

with the matrix of reflection coefficients $\hat{\underline{R}}_{ab}$ defined as:

$$\hat{\underline{R}}_{ab} = \begin{pmatrix} \hat{R}_{ab}^{LL} & \hat{R}_{ab}^{yL} & 0 & 0 & 0 \\ \hat{R}_{ab}^{Ly} & \hat{R}_{ab}^{yy} & 0 & 0 & 0 \\ 0 & 0 & \hat{R}_{ab}^{xx} & 0 & 0 \\ 0 & 0 & 0 & \hat{R}_{ab}^{UU} & \hat{R}_{ab}^{VU} \\ 0 & 0 & 0 & \hat{R}_{ab}^{UV} & \hat{R}_{ab}^{VV} \end{pmatrix}. \quad (3.44)$$

Equations (3.40) and (3.41) can be written in matrix form as

$$\begin{aligned} G^-(0)C_m + \mathbf{I}_{pm}^-(0) &= \hat{\mathbf{R}}_{10} \left(G^+(0)C_m + \mathbf{I}_{pm}^+(0) \right); \\ G^+(\tau_b)C_m + \mathbf{I}_{pm}^+(\tau_b) &= \hat{\mathbf{R}}_{12} \left(G^-(\tau_b)C_m + \mathbf{I}_{pm}^-(\tau_b) \right); \end{aligned} \quad (3.45)$$

where

$$G^-(\tau) = \begin{pmatrix} g_{m1}^1 e^{-\lambda_1 \tau} & g_{m2}^1 e^{-\lambda_2 \tau} & \dots & g_{m10N}^1 e^{-\lambda_{10N} \tau} \\ g_{m1}^2 e^{-\lambda_1 \tau} & g_{m2}^2 e^{-\lambda_2 \tau} & \dots & g_{m10N}^2 e^{-\lambda_{10N} \tau} \\ \cdot & \cdot & \cdot & \cdot \\ g_{m1}^N e^{-\lambda_1 \tau} & g_{m2}^N e^{-\lambda_2 \tau} & \dots & g_{m10N}^N e^{-\lambda_{10N} \tau} \end{pmatrix}; \quad (3.46)$$

$$G^+(\tau) = \begin{pmatrix} g_{m1}^{-N} e^{-\lambda_1 \tau} & g_{m2}^{-N} e^{-\lambda_2 \tau} & \dots & g_{m10N}^{-N} e^{-\lambda_{10N} \tau} \\ g_{m1}^{-N+1} e^{-\lambda_1 \tau} & g_{m2}^{-N+1} e^{-\lambda_2 \tau} & \dots & g_{m10N}^{-N+1} e^{-\lambda_{10N} \tau} \\ \cdot & \cdot & \cdot & \cdot \\ g_{m1}^{-1} e^{-\lambda_1 \tau} & g_{m2}^{-1} e^{-\lambda_2 \tau} & \dots & g_{m10N}^{-1} e^{-\lambda_{10N} \tau} \end{pmatrix}; \quad (3.47)$$

$$C_m = \begin{pmatrix} C_{m1} \\ C_{m2} \\ \dots \\ C_{m10N} \end{pmatrix}. \quad (3.48)$$

The equations in (3.45) are grouped to form a single matrix equation:

$$G_1 C_m + P = R_G C_m + R_P, \quad (3.49)$$

where

$$G_1 = \begin{pmatrix} G^-(0) \\ G^+(\tau_b) \end{pmatrix}; \quad (3.50)$$

$$P = \begin{pmatrix} \mathbf{I}_{pm}^-(0) \\ \mathbf{I}_{pm}^+(\tau_b) \end{pmatrix}; \quad (3.51)$$

$$R_G = \begin{pmatrix} \hat{\mathbf{R}}_{10} G^+(0) \\ \hat{\mathbf{R}}_{12} G^-(\tau_b) \end{pmatrix}; \quad (3.52)$$

$$R_P = \begin{pmatrix} \hat{\mathbf{R}}_{10} \mathbf{I}_{pm}^+(0) \\ \hat{\mathbf{R}}_{12} \mathbf{I}_{pm}^-(\tau_b) \end{pmatrix}. \quad (3.53)$$

Solving for C_m ,

$$C_m = (G_1 - R_G)^{-1}(R_P - P). \quad (3.54)$$

Once the constants C_m are known, the diffuse intensity can be computed at any depth from (3.39). Section 3.5 details the computation of the scattering cross section from the specific intensity, which is required to compare the RT model with experimental measurements in section 5.

3.3 Transient radiative transfer

From (3.10), the intensity was assumed to be a function of the position z and the direction (μ, ϕ) . If the intensity changes with time, it can be shown that the transient RT equation⁵ is given by [15]

$$\begin{aligned} & \mu \frac{\partial \underline{I}(\mu, \phi, \tau, \xi)}{\partial \tau} + \frac{1}{\tilde{\underline{c}}} \frac{\partial \underline{I}(\mu, \phi, \tau, \xi)}{\partial \xi} = \\ & -\tilde{\underline{c}} \underline{I}(\mu, \phi, \tau, \xi) + \frac{1}{4\pi\kappa_T} \int_{-1}^1 \int_0^{2\pi} \underline{P}(\mu, \phi; \mu', \phi') \underline{I}(\mu', \phi', \tau, \xi) d\mu' d\phi', \end{aligned} \quad (3.55)$$

⁵The transient RT equation is the most recent development in transport theory for both electromagnetics and acoustics and therefore it is still a topic of ongoing research [24, 15].

where $\xi = \eta c_T \kappa_T t$ is a *normalized time* similar to the normalized depth $\tau = \eta \kappa_T z$,

and

$$\tilde{\underline{c}} = \frac{1}{c_T} \begin{pmatrix} c_L & 0 & 0 & 0 & 0 \\ 0 & c_T & 0 & 0 & 0 \\ 0 & 0 & c_T & 0 & 0 \\ 0 & 0 & 0 & c_T & 0 \\ 0 & 0 & 0 & 0 & c_T \end{pmatrix}. \quad (3.56)$$

By using the property of the Fourier Transform for derivatives, $\mathcal{F} \left(\frac{\partial \underline{I}(\mu, \phi, \tau, \xi)}{\partial \xi} \right) = i\Theta \underline{I}(\mu, \phi, \tau, \Theta)$, (3.55) is transformed to the Θ domain:

$$\begin{aligned} \mu \frac{\partial \underline{I}(\mu, \phi, \tau, \Theta)}{\partial \tau} &= - \left[\frac{i\Theta}{\tilde{\underline{c}}} + \tilde{\underline{\sigma}} \right] \frac{\partial \underline{I}(\mu, \phi, \tau, \Theta)}{\partial \xi} \\ &+ \frac{1}{4\pi\kappa_T} \int_{-1}^1 \int_0^{2\pi} \underline{P}(\mu, \phi; \mu', \phi') \underline{I}(\mu', \phi', \tau, \Theta) d\mu' d\phi'. \end{aligned} \quad (3.57)$$

It is important to establish a distinction between the frequency domain Θ , referred as the *outer frequency* [15], and the frequency ω of the source, known as the *inner frequency*. The inner frequency determines the behavior of the scatterers in the random media, and it is included in the formulation by calculating $\underline{P}(\mu, \phi; \mu', \phi')$ and the scattering cross sections.

On the other hand, the outer frequency determines the rate of change of the intensity, and therefore it is expected that $\Theta \ll \omega$. Figure 3.6 illustrates the difference between the inner and outer frequency, and it shows the extreme cases

of a steady-state source ($\Theta = 0$) or an instantaneous pulse of energy.

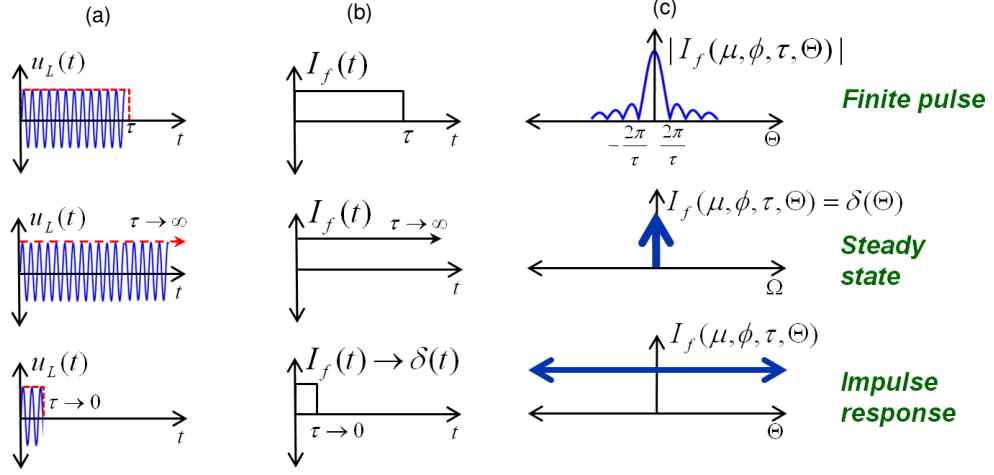


Figure 3.6: Interpretation of the inner and outer frequency scales: (a) Illustration of the time domain of the excitation signal, with a frequency of oscillation ω ; (b) Corresponding input excitation in terms of specific intensity; (c) Input excitation in the outer frequency domain Θ , which describes the rate of change of the specific intensity in (b).

Equation (3.55) has the same form of (3.10) with the only exception of a complex total cross section $\sigma_c = \left[\frac{i\Theta}{\underline{c}} + \underline{\tilde{\sigma}} \right]$, where $\underline{\tilde{\sigma}}$ is real and it was defined in (3.11). Then, the solution method for the vector RT equation also apply to (3.55). Equation (3.55) corresponds to the last row in Fig. 3.6, and therefore it gives the impulse response of the media when the input intensity is an instantaneous pulse of energy.

3.4 Power conservation

In most of the applications of the RT model found in the literature, the measured quantity is the radiance (another name for the specific intensity), while

in sonar applications, a more useful quantity is the power flux F (i.e. the amount of power per unit area). In this section, this relationship is established, and an expression was developed by the author to show the conservation of power in the RT model.

3.4.1 The scalar case

It is easier to show the conservation of power starting with the scalar RT equation. Once this result is obtained, it can be extended to the vector case. Equation (3.2) can be written as

$$\begin{aligned} \nabla \cdot (I(\mu, \phi, z) \hat{s}) &= -\eta \sigma_t I(\mu, \phi, z) + \\ &\frac{\eta}{4\pi} \int_{4\pi} P(\mu, \phi; \mu', \phi') I(\mu', \phi', z) d\Omega', \end{aligned} \quad (3.58)$$

where $\nabla \cdot (I(\mu, \phi, z) \hat{s}) = \left(\frac{\partial}{\partial x} \hat{x} + \frac{\partial}{\partial y} \hat{y} + \frac{\partial}{\partial z} \hat{z} \right) \cdot (I(\mu, \phi, z) \hat{s})$ is the divergence that acts upon the specific intensity in the direction of the unit vector $\hat{s} = \sin \theta \cos \phi \hat{x} + \sin \theta \sin \phi \hat{y} + \cos \theta \hat{z}$. By integrating over a solid angle of 4π in both sides of (3.58),

$$\begin{aligned} \nabla \cdot \int_{4\pi} (I(\mu, \phi, z) \hat{s}) d\Omega &= -\eta \sigma_t \int_{4\pi} I(\mu, \phi, z) d\Omega + \\ &\frac{\eta}{4\pi} \int_{4\pi} \int_{4\pi} P(\mu, \phi; \mu', \phi') d\Omega I(\mu', \phi', z) d\Omega'. \end{aligned} \quad (3.59)$$

Since $\kappa_s = \frac{1}{4\pi} \int_{4\pi} P(\mu, \phi; \mu', \phi') d\Omega$ (see (2.5)), (3.59) can be simplified to

$$\begin{aligned} \nabla \cdot F(z, \mu, \phi) &= -\eta \sigma_t \int_{4\pi} I(\mu, \phi, z) d\Omega + \eta \kappa_s \int_{4\pi} I(\mu', \phi', z) d\Omega' \\ &= -\eta \nu \int_{4\pi} I(\mu, \phi, z) d\Omega, \end{aligned} \quad (3.60)$$

where $F(z, \mu, \phi) = \int_{4\pi} (I(\mu, \phi, z) \hat{s}) d\Omega$ is the power flux in the \hat{s} direction and ν is the absorption cross section defined in (2.7). Therefore, for lossless media in which $\nu = 0$, the divergence of the power flux is zero and the conservation of energy holds[21].

Nevertheless, a more useful way to write (3.60) is as a mathematical expression for the gradient of the diffuse flux using the reduced intensity as a source. By assuming that the reduced intensity is a decaying exponential $I_{ri}(z) = K_{L0} e^{-\eta \sigma_t z / \mu} \delta(\omega - \omega_o)$, (3.58) can be written as:

$$\begin{aligned} \nabla \cdot (I_d(\mu, \phi, z) \hat{s}) &= -\eta \sigma_t I_d(\mu, \phi, z) + \\ &\frac{\eta}{4\pi} \int_{4\pi} P(\mu, \phi; \mu', \phi') I_d(\mu', \phi', z) d\Omega' + \eta \frac{K_{L0} P(\mu, \phi; \mu_o, \phi_o) e^{-\eta \sigma_t z / \mu_o}}{4\pi}. \end{aligned} \quad (3.61)$$

Integration over a solid angle of 4π yields an expression for the diffuse power flux F_d :

$$\begin{aligned} \nabla \cdot (F_d(\mu, \phi, z)) &= -\eta \sigma \int_{4\pi} I_d(\mu, \phi, z) d\Omega + \\ &\eta \kappa_s \int_{4\pi} I_d(\mu, \phi, z) d\Omega + K_{L0} \eta \kappa_s e^{-\eta \sigma_t z / \mu_o}; \end{aligned} \quad (3.62)$$

or

$$\nabla \cdot (F_d(\mu, \phi, z)) = -\eta\nu \int_{4\pi} I_d(\mu, \phi, z) d\Omega + K_{L0}\eta\kappa_s e^{-\eta\sigma z/\mu_o}. \quad (3.63)$$

From the divergence theorem[25],

$$\int_{vol} \nabla \cdot (F_d(\mu, \phi, z)) dV = \int_{surf} (F_d(\mu, \phi, z)) \cdot \hat{s} dS, \quad (3.64)$$

where $\int_{vol} < . > dV$ is an integral over a finite volume containing scatterers and $\int_{surf} < . > dS$ is a surface integral over the area that encloses the volume V . Since $F_d(\mu, \phi, z)$ is a power flux (i.e. power per unit area), (3.64) gives the total diffuse power P_d going through the surface that encloses V :

$$P_d = \int_{x_o}^{x_o+1 \text{ m}} \int_{y_o}^{y_o+1 \text{ m}} \int_0^{z_d} \nabla \cdot (F_d(\mu, \phi, z)) dz dy dx; \quad (3.65)$$

or

$$\begin{aligned} P_d &= -\eta\nu \int_{4\pi} \int_{z=0}^{z=z_d} I_d(\mu, \phi, z) dz d\Omega + K_{L0}\eta\kappa_s \int_{z=0}^{z=z_d} e^{-\eta\sigma_t z/\mu_o} dz \\ &= -\eta\nu \int_{4\pi} \int_{z=0}^{z=z_d} I_d(\mu, \phi, z) dz d\Omega + K_{L0} \frac{\kappa_s}{\sigma_t} \mu_o [1 - e^{-\eta\sigma_t z_d/\mu_o}]. \end{aligned} \quad (3.66)$$

Equation 3.66 can be interpreted as follows: the term $[1 - e^{-\eta\sigma_t z_d/\mu_o}]$ represents the difference between the incident flux from the source and the output

coherent power flux at $z = z_d$. This difference represents the amount of power that was “taken” by the scatterers and transformed into diffuse intensity or absorbed by the media. If the absorption $\nu = 0$, then the diffuse power is exactly the amount of power removed from the incident coherent stream. If there is absorption, the diffuse power is reduced by $-\eta\nu \int_{4\pi} \int_{z=0}^{z=z_d} I_d(\mu, \phi, z) dz d\Omega$.

3.4.2 The vector case

For (3.10) the same procedure as in the scalar case can be followed by considering independently each source term. The equivalent expression for the diffuse power with eight sources is:

$$\begin{aligned}
P_d = & P_{av}^L + P_{av}^T - \eta\nu_L \int_{4\pi} \int_{z=0}^{z=z_d} I_{dL}(\mu, \phi, z) dz d\Omega \\
& - \eta\nu_T \int_{4\pi} \int_{z=0}^{z=z_d} (I_{dx}(\mu, \phi, z) + I_{dy}(\mu, \phi, z)) dz d\Omega,
\end{aligned} \tag{3.67}$$

where ν_L and ν_T are the absorption coefficients for longitudinal and transversal waves and

$$\begin{aligned}
P_{av}^L = & A_{1L}^{\downarrow} \frac{\kappa_L}{\sigma_L} \mu_{LL}^{01} \left(1 - e^{-\eta \sigma_L z_d / \mu_{LL}^{01}} \right) + \\
& + A_{2L}^{\downarrow} \frac{\kappa_L}{\sigma_L} \mu_{TL}^{11} \left(1 - e^{-\eta \sigma_L z_d / \mu_{TL}^{11}} \right) + \\
& + A_{1L}^{\uparrow} \frac{\kappa_L}{\sigma_L} \mu_{LL}^{01} \left(e^{-\eta \sigma_L z_d / \mu_{LL}^{01}} - 1 \right) + \\
& + A_{2L}^{\uparrow} \frac{\kappa_L}{\sigma_L} \mu_{TL}^{11} \left(e^{-\eta \sigma_L z_d / \mu_{TL}^{11}} - 1 \right) ;
\end{aligned} \tag{3.68}$$

$$\begin{aligned}
P_{av}^T = & A_{1T}^{\downarrow} \frac{\kappa_T}{\sigma_T} \mu_{LT}^{01} \left(1 - e^{-\eta \sigma_T z_d / \mu_{LT}^{01}} \right) + \\
& + A_{2T}^{\downarrow} \frac{\kappa_T}{\sigma_T} \mu_{LT}^{11} \left(1 - e^{-\eta \sigma_T z_d / \mu_{LT}^{11}} \right) + \\
& + A_{1T}^{\uparrow} \frac{\kappa_T}{\sigma_T} \mu_{LT}^{01} \left(e^{-\eta \sigma_T z_d / \mu_{LT}^{01}} - 1 \right) + \\
& + A_{2T}^{\uparrow} \frac{\kappa_T}{\sigma_T} \mu_{LT}^{11} \left(e^{-\eta \sigma_T z_d / \mu_{LT}^{11}} - 1 \right) ;
\end{aligned}$$

represent the available power density supplied by the longitudinal and transversal sources to the media.

3.4.3 Numeric example of power conservation in lossless sediment

The conservation of the normal component of the power flux can be illustrated using parameters relevant to ocean acoustics. In this example, the environment consists of a layer of sand with spherical cavities as scatterers, lying on top of a sand infinite half space, as depicted in Fig. 3.7.

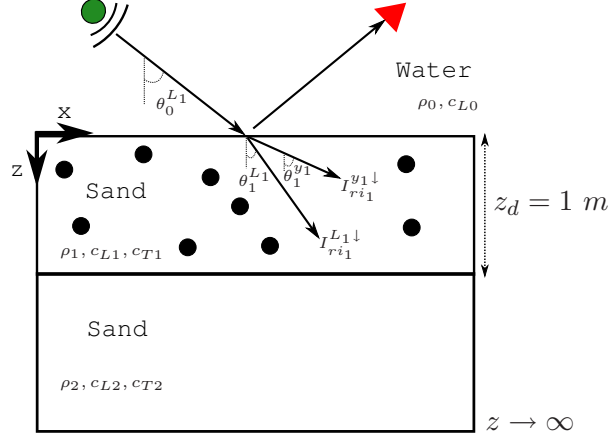


Figure 3.7: Layered environment consisting of an infinite halfspace and a finite layer of thickness z_d with embedded cavities. Since the background media for layers 1 and 2 are the same, no energy is reflected back from this interface.

Since the background media are the same for layers 1 and 2, the elastic reflection coefficients are zero. Therefore, from (3.34) the corresponding RT equation is:

$$\begin{aligned} \frac{\partial \mathbf{I}_{dm}(\tau)}{\partial \tau} + \mathbf{W}_m \mathbf{I}_{dm}(\tau) = \\ \mathbf{S}_{1m}^{L_1\downarrow} \exp \left[-\frac{\tilde{\sigma}_L \tau}{\mu_1^{L_1}} \right] + \mathbf{S}_{1m}^{y_1\downarrow} \exp \left[-\frac{\tilde{\sigma}_T \tau}{\mu_1^{y_1}} \right], \end{aligned} \quad (3.69)$$

where the two sources correspond to the coupling of longitudinal energy in the water column into longitudinal and shear vertical reduced intensities in the sediment.

For the sand-water interface between layers 0 and 1, reflection and transmission coefficients must be considered to determine the amplitude of the sources $\mathbf{S}_{1m}^{L_1\downarrow}$ and $\mathbf{S}_{1m}^{y_1\downarrow}$, and to define the top BC. Table 3.1 shows the value of the density

and sound speed for a typical sandy sediment [26] and water.

Table 3.1: Acoustic properties of the sediment and water column used in the RT simulation.

Variable	Sediment(see [26])	Water
ρ_s (kg/m ³)	2023.2	1027
c_L (m/s)	1689	1500
c_T (m/s)	117	0

Simulations of the transmission/reflection coefficients at the water-sediment interface [27] are shown in Fig. 3.8 and 3.9:

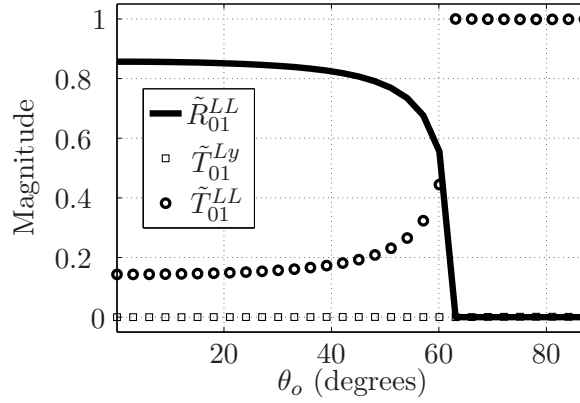


Figure 3.8: A longitudinal wave in the fluid reaches the fluid-solid boundary: \tilde{R}_{01}^{LL} (circles), \tilde{T}_{01}^{LL} (solid) and \tilde{T}_{01}^{Ly} (squares) for the parameters in Table 3.1. Note the critical angle for the transmitted longitudinal wave when $\theta_o = \sin^{-1}(c_f/c_L)$.

The scatterers are spherical cavities with radius $a = 10$ mm and the concentration is $\eta = 2388$ scat./m³. Environments consisting of gassy sediments are well known in ocean acoustics, and this phenomenon has been studied by several authors (see section 6.1). As a reference of the scattering properties of air

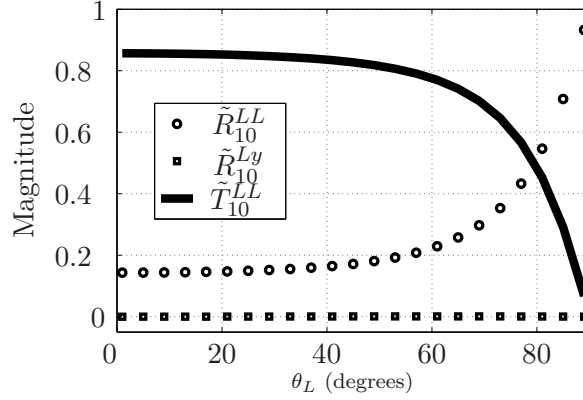


Figure 3.9: A longitudinal wave in the solid reaches the solid-fluid boundary: \tilde{T}_{10}^{LL} (solid), \tilde{R}_{10}^{LL} (circles) and \tilde{R}_{10}^{Ly} (squares) for the parameters in Table 3.1. Most of the energy carried by the longitudinal wave in the sediment is transmitted to the water for $0 < \theta_L < 60^\circ$.

cavities in elastic media, Fig. 3.10 shows the cross section for a transversal and longitudinal plane wave of frequency 10 kHz impinging upon a single scatterer of radius a ⁶. In Fig. 3.10(b), a resonance peak is observed at $a = 3.8$ mm and it matches the value predicted by Kargl et al [28]. The values of $\kappa_L = 1.8 \times 10^{-3} \text{ m}^2$ and $\kappa_T = 0.45 \times 10^{-3} \text{ m}^2$ from Fig. 3.10 corresponding to $a = 10 \text{ mm}$ will be used in this simulation.

Figure 3.11 shows the incident and scattered power fluxes. For this simulation, the incident power flux is $K_{L0} = 1 \text{ W/m}^2$, the frequency of the source is $f = 10 \text{ kHz}$, the particle radius is $a = 0.01 \text{ m}$ and the thickness of layer 1 is $z_b = 1 \text{ m}$. It is observed that the amount of volume (diffuse) scattering coming out of the

⁶Computation of scattering cross section from spherical scatterers will be explained in section 4.1

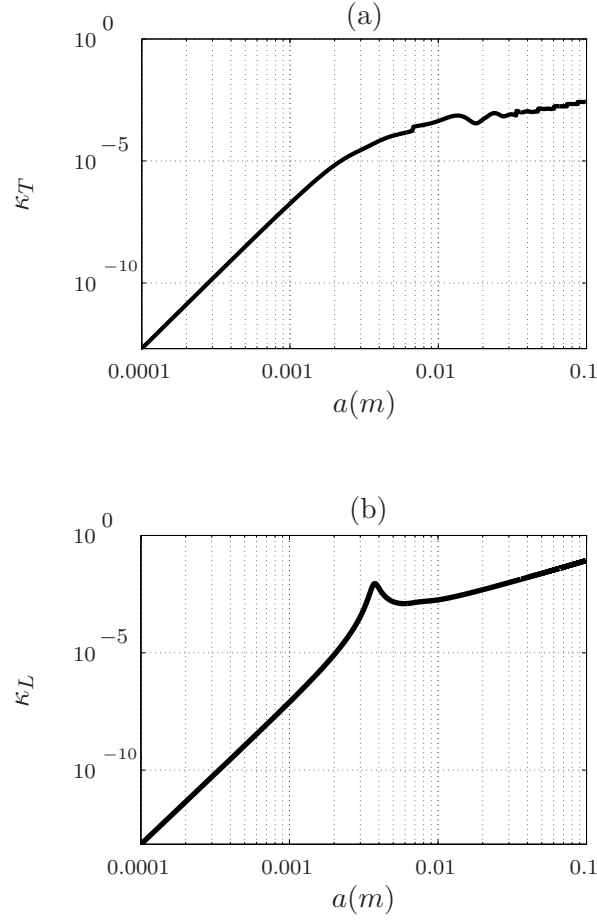


Figure 3.10: (a) Scattering cross section for a transversal plane wave at 10 kHz ($k_T = 537 \text{ m}^{-1}$); (b) Same as (a) for an incident longitudinal wave ($k_L = 37.2 \text{ m}^{-1}$). A resonance peak can be observed at $a = 3.8 \text{ mm}$. In the example in this section, scatterers with $a = 10 \text{ mm}$ are utilized.

layer at $z = z_b$, $\left(F_{d_1}^{L\downarrow} + F_{d_1}^{T\downarrow}\right)|_{z=z_b}$, is higher than the volume scattering at $z = 0$, $\left(F_{d_1}^{L\uparrow} + F_{d_1}^{T\uparrow}\right)|_{z=0}$.

The critical angle for the longitudinal energy that couples into the sediment is 62° , and above this angle the volume scattering is negligible. Because the shear

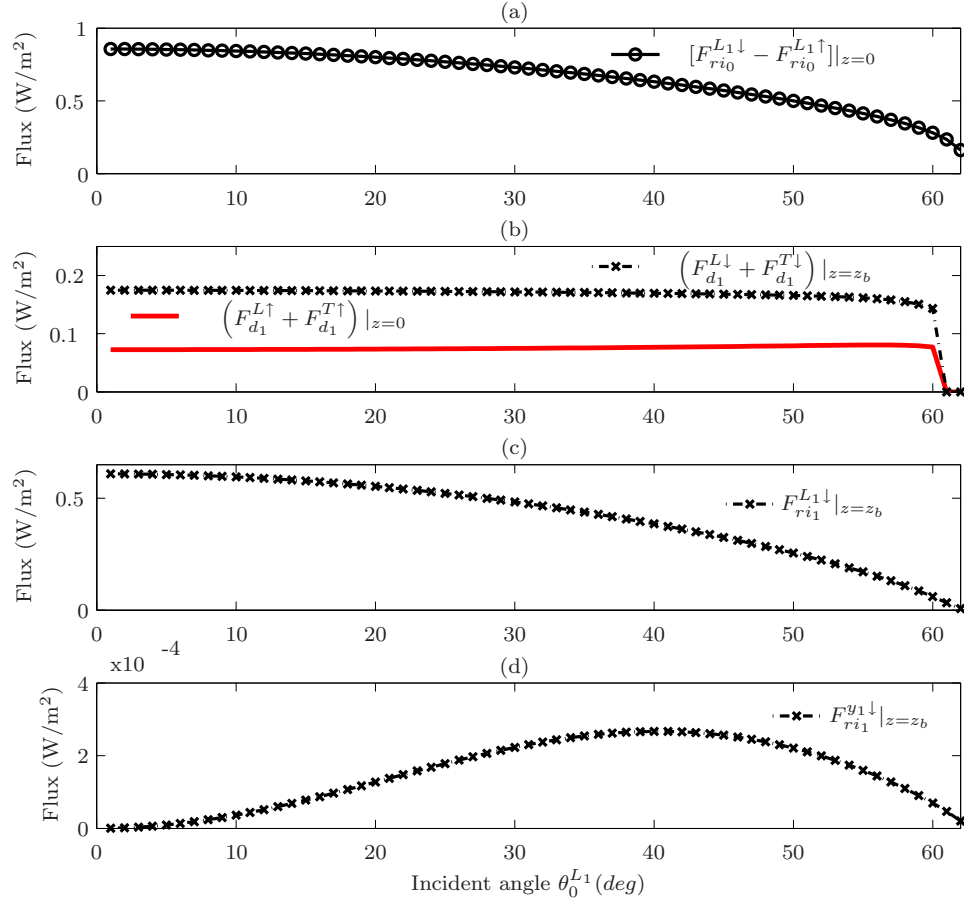


Figure 3.11: Normal component of the outgoing power flux in layer 1, for a configuration Water-Sand-Sand and no background attenuation. (a) The difference $F_{ri0}^{L1\downarrow} - F_{ri0}^{L1\uparrow}$ at $z = 0$ indicates the power flux that is transmitted into layer 1 from the water column; (b) Total upward (red) and downward (black) diffuse power flux at $z = 0$ and $z = z_b$ m, respectively; (c) and (d) show the power flux from coherent longitudinal and shear vertical energy, respectively (note different scale on (d)). Due to the transparent boundary condition at $z = z_b$, $F_{ri1}^{L1\uparrow}$, $F_{ri1}^{L2\uparrow}$, $F_{ri1}^{L2\downarrow}$, $F_{ri1}^{y1\uparrow}$, $F_{ri1}^{y2\uparrow}$ and $F_{ri1}^{y2\downarrow}$ are zero.

sound speed in the sediment is smaller than the sound speed in the water, there is always some minimum amount of transversal energy coupled into the finite layer. Nevertheless, the total contribution to volume scattering related to the

shear polarization is small (note scale on Fig. 3.11(d)), since the transmission coefficient from the water column into the sediment, T_{01}^{Ly} , is very small compared to T_{01}^{LL} . Since Fig. 3.11 was computed assuming lossless media, the conservation of the normal power flux in (3.68) can be confirmed at each incidence angle θ_0^{L1} .

The example presented in this section illustrates the application of the expression (3.68) developed in section 3.4.2 as a tool to verify the RT model in terms of conservation of power. Note that the power flux in Fig. 3.11 corresponds to the total power scattered from the media in all directions, which differs from the actual power that would be measured with a finite size receiver in a field experiment. In section 3.5, the definition of the received power is introduced, and it will be used in chapter 6 to compare the RT model to experimental data from a three-layer environment in which the scatterers are gas cavities trapped in a lossy background sediment.

3.5 Obtaining the scattering cross section from transport theory

Once the specific intensity has been obtained, it is required to make a transformation into more standard units that can be related to other scattering models or to measurements[29]. One choice is to define the scattering cross section of the random medium, which is introduced in this section.

Consider the bistatic measurement system represented in Fig. 3.12(a), in

which a directional source illuminates a finite patch denoted in blue. The size of this patch is determined by the radiation pattern of the transmitter and its distance from the surface. An omni directional hydrophone will detect energy propagating within a solid angle that is entirely defined by the size of the illuminated patch and the radial distance to the slab. From Fig. 3.12(a), this solid angle is defined as $\Delta\Omega = dA/R^2$, where dA is the area subtended by the solid angle at a distance R from the receiver.

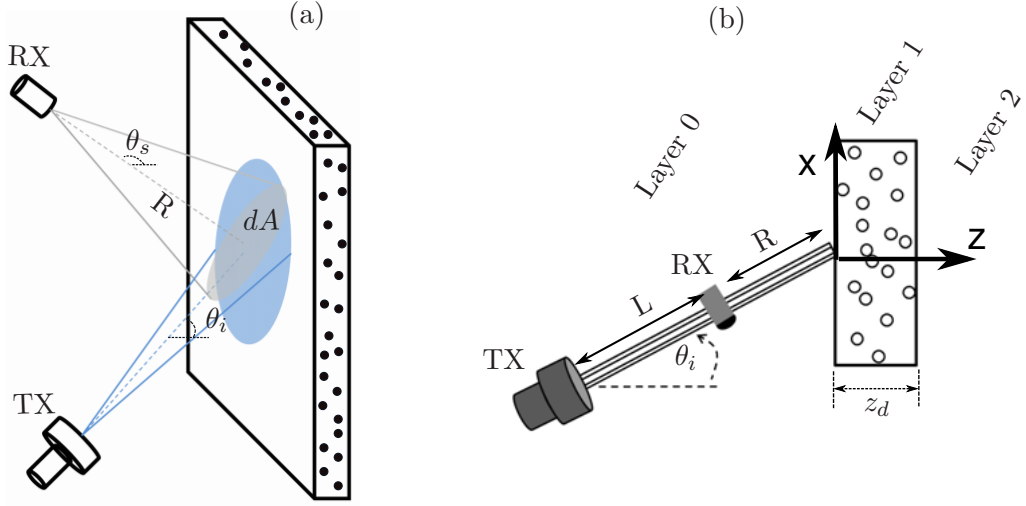


Figure 3.12: Measurement of volume scattering from layered media: (a) General bistatic geometry in which a directional transmitter(TX) illuminates a patch (blue) defined by its radiation pattern and its distance from the media. The omni directional receiver detects the energy crossing the area dA (gray); (b) Monostatic configuration used in the experiments presented in section 5.

For the experiments presented in section 5, the measurement setup is the special case illustrated in Fig. 3.12(b), for which θ_i is the elevation angle that determines the direction of the excitation, while $\theta_s = \pi - \theta_i$ is the elevation

corresponding to the scattered energy. The origin of the coordinate system is the center of the illuminated patch, with the z axis pointing toward the media. Therefore, $\theta > 0$ represents energy propagating from left to right. Without loss of generality the azimuth angle of the incident radiation is defined as $\phi_i = 0^\circ$.

The power received at an omni directional hydrophone can be computed from the specific intensity $I(\mu, \phi, z)$ as:

$$P_r = \int_{\Delta\Omega} \hat{T}_{10} I(\mu, \phi, z = 0) d\Omega, \quad (3.70)$$

where $\Delta\Omega$ was related to dA in the discussion concerning Fig. 3.12(a). The integration in (3.70) can be solved numerically, but an approximation can provide some insight into the relation between the RT model and classic models. For example, in the far field $\Delta\Omega$ is small and it can be expected that $I(\mu, \phi, z = 0)$ does not change significantly within the domain of integration, so it can be treated as a constant in the integration which reduces (3.70) to:

$$P_r = \hat{T}_{10} I(\mu, \phi, z = 0) \frac{dA}{R^2}. \quad (3.71)$$

Then, the scattering cross section of the media is given by

$$\Upsilon = R^2 \frac{P_r}{P_i} = \hat{T}_{10} I(\mu, \phi, z = 0) dA. \quad (3.72)$$

3.6 Conclusion

This section introduces the concept of Radiative Transfer for the scalar case, and it extends the set of required equations for an elastic layer with finite thickness supporting three kinds of polarizations. The solution method of the steady-state and transient RT equation was described, and software routines were implemented in MATLAB to simulate scattering as a function of different experimental parameters such as frequency of operation, size and constitution of scatterers, background attenuation and layer thickness. Since the conservation law is an important statement in transport theory, expressions for the conservation of the normal component of the power flux were derived and used as a preliminary validation of the implemented software routines. Finally, the scattering cross section was introduced as a standard way to relate the specific intensity obtained from the RT model to measured data or for comparison with other models.

Chapter 4

Validation of the RT scattering simulator

The computational model developed for this work consists of three main modules: the first module computes the frequency-dependent scattering properties of a single scatterer. The second module computes the elastic reflection coefficients to be used as boundary conditions. The last module computes the solution of the transient and the steady-state RT equation, according to the theory presented in section 3.2.4. In this section, equations related to the first two modules are introduced, and simulations from each of the modules are presented and compared to results found in the literature.

4.1 Scattering from a single elastic particle

This section discusses the method of obtaining the function $\underline{P}(\mu, \phi; \mu', \phi')$ in (3.10) and the scattering cross sections (3.6) for the special case of spherical scatterers. There are two important observations related to the scattering function:

1. The form of the RT equation in (3.10) is the same for different shapes of

scatterers (cylinders, irregular scatterers, etc.), and as long as the scattering function $\underline{P}(\mu, \phi; \mu', \phi')$ can be found, the RT equation can be solved.

2. The procedure to obtain $\underline{P}(\mu, \phi; \mu', \phi')$ is analogous to finding the Fresnel reflection coefficients, with the exception that the scattering surface is not an infinite flat plane, but the surface of the scatterer. For scatterers with regular shapes like spheres and cylinders, $\underline{P}(\mu, \phi; \mu', \phi')$ can be computed analytically. For irregular shapes, numerical methods or other approximations can be utilized.

Figure 3.4(a) shows a diagram of an incident plane longitudinal wave on a scatterer. If the scatterer is a sphere of radius a , the scattered wave has components on \hat{r} , $\hat{\theta}$ and $\hat{\phi}$. Following the procedure by Ying et al [30], the particle displacement s due to the incident plane wave can be expressed as a summation of spherical harmonics:

$$\begin{aligned}
 s_{ir}(r, \theta) &= -\frac{1}{k_L} \sum_{m=0}^{\infty} (-1)^{m+1} (2m+1) \frac{\partial j_m(k_L r)}{r} P_m(\cos \theta); \\
 s_{i\theta}(r, \theta) &= -\frac{1}{rk_L} \sum_{m=0}^{\infty} (-1)^{m+1} (2m+1) j_m(k_L r) \frac{\partial P_m(\cos(\theta))}{\partial \theta}; \\
 s_{i\phi}(r, \theta) &= 0;
 \end{aligned} \tag{4.1}$$

where $k_L = \omega/c_L$ and $k_T = \omega/c_T$ are the longitudinal and transversal wave numbers of the background media, respectively. The quantity $P_m(\cos \theta)$ is the

Legendre polynomial of m^{th} degree and $j_m(k_L r)$ is the spherical Bessel function of the first kind.

Similarly, the particle displacement due to the scattered wave can be written as a summation of spherical harmonics multiplied by (eventually known) coefficients A_m and B_m ¹:

$$\begin{aligned} s_{sr}(r, \theta) &\approx \frac{e^{ik_L r}}{r} \sum_{m=0}^{\infty} A_m (-1)^m P_m(\cos \theta) = \frac{e^{ik_L r}}{r} f_{LL}(\cos \theta); \\ s_{s\theta}(r, \theta) &\approx \frac{e^{ik_L r}}{r} \sum_{m=0}^{\infty} B_m (-1)^m \frac{\partial P_m(\cos \theta)}{\partial \theta} = \frac{e^{ik_L r}}{r} f_{Ly}(\cos \theta); \\ s_{s\phi}(r, \theta) &= 0; \end{aligned} \quad (4.2)$$

In (4.2), f_{LL} and f_{Ly} represent the partition of the incident longitudinal polarization into scattered longitudinal and shear vertical polarizations, and they are proportional to P_{LL} and P_{Ly} from (3.12), so the task is reduced to finding the coefficients A_m and B_m .

The unknown coefficients can be found by enforcing boundary conditions (BC) at the surface of the sphere of radius $r = a$. For example, if the sphere is made of rigid material, the particles at the surface of the sphere can not oscillate. This

¹This is similar to a Fourier Series decomposition in the sense that spherical harmonics are a complete orthonormal set. Therefore, most functions can be written as a weighted summation of spherical harmonics.

rigid boundary condition results in a system of two equations with two unknowns,

$$\begin{aligned} s_{ir}(r = a, \theta) + s_{sr}(r = a, \theta) &= 0; \\ s_{i\theta}(r = a, \theta) + s_{s\theta}(r = a, \theta) &= 0; \end{aligned} \tag{4.3}$$

from which A_m and B_m can be found.

When the incident wave is transversal, it is written as [31]

$$\begin{aligned} s_{ir}(r, \theta) &= \cos \phi \frac{e^{ik_L r}}{k_L r} \sum_{m=0}^{\infty} (-1)^{m+1} (2m+1) \frac{\partial j_m(k_L r)}{r} P_m(\cos \theta); \\ s_{i\theta}(r, \theta) &= -\frac{1}{rk_L} \sum_{m=0}^{\infty} (-1)^{m+1} (2m+1) j_m(k_L r) \frac{\partial P_m(\cos \theta)}{\partial \theta}; \\ s_{i\phi}(r, \theta) &= 0; \end{aligned} \tag{4.4}$$

and the scattered wave as

$$\begin{aligned}
s_{sr}(r, \theta) &\approx \cos \phi \frac{e^{ik_L r}}{k_L r} \sum_{m=0}^{\infty} d_m \frac{(2m+1)}{m(m+1)} P_m(\cos \theta) = \cos \phi \frac{e^{ik_L r}}{r} f_{Ly}(\cos \theta); \\
s_{s\theta}(r, \theta) &\approx \cos \phi \frac{e^{ik_T r}}{k_T r} \sum_{m=0}^{\infty} \frac{i}{\sin \theta} [a_m P_m(\cos \theta) \\
&\quad + b_m \left(\frac{m P_{m+1}(\cos \theta)}{m+1} - \frac{(m+1) P_{m-1}(\cos \theta)}{m} \right)] \\
&= \cos \phi \frac{e^{ik_T r}}{r} f_{yy}(\cos \theta); \\
s_{s\phi}(r, \theta) &\approx \sin \phi \frac{e^{ik_T r}}{k_T r} \sum_{m=0}^{\infty} \frac{i}{\sin \theta} [b_m \frac{2m+1}{m(m+1)} P_m(\cos \theta) \\
&\quad + a_m \left(\frac{m P_{m+1}(\cos \theta)}{m+1} - \frac{(m+1) P_{m-1}(\cos \theta)}{m} \right)] \\
&= \sin \phi \frac{e^{ik_T r}}{r} f_{xx}(\cos \theta);
\end{aligned} \tag{4.5}$$

and the coefficients a_m, b_m and d_m can be found following a similar procedure of matching BC at the surface of the scatterer.

MATLAB routines were written by the author to compute the scattering coefficients for a spherical air cavity surrounded by elastic media and for the more general case of an elastic sphere surrounded by elastic media. These coefficients (A_m, B_m, a_m, b_m and d_m) are required in (3.6) to compute the scattering cross sections and the elements in $\underline{\mathbb{P}}(\mu, \phi; \mu', \phi')$. It can be demonstrated [30, 31] that the longitudinal and transversal scattering cross sections for spherical scatterers in (3.6) are:

$$\begin{aligned}
\kappa_L &= \sum_{m=0}^{\infty} \frac{1}{2m+1} \left(|A_m|^2 + m(m+1) \frac{k_L}{k_T} |B_m|^2 \right); \\
\kappa_T &= \sum_{m=0}^{\infty} \frac{2m+1}{2} \left(\frac{1}{k_T^2} |a_m|^2 + \frac{1}{k_T^2} |b_m|^2 + \frac{k_T}{k_L^3 m(m+1)} |d_m|^2 \right);
\end{aligned} \tag{4.6}$$

To test the MATLAB code, Fig. 4.1 shows the scattering cross section when a shear wave is incident upon an elastic sphere with $c_{Lp} = 6000$ m/s, $c_{Tp} = 3500$ m/s, and $\rho_p = 2700$ kg/m³. The sphere is surrounded by a “softer” material with $c_{L1} = 1400$ m/s, $c_{T1} = 0.1$ m/s, and $\rho_2 = 1000$ kg/m³. The results are compared to the ones published by Korneev et al [32]². Similar results (not shown) were verified for the case of an incident longitudinal wave and for void scatterers, which can be found in seabed sediments in the form of trapped gas bubbles.

4.2 Plane wave reflection coefficients

If the roughness of the interface between layers can be ignored, plane wave reflection/transmission coefficients for elastic media can be used as the BC in (3.13). In ocean acoustics, there are two types of interfaces: the liquid-solid interface between the water column and the sediment, and the solid-solid interface,

²During the implementation of software routines for scattering of shear waves by an elastic sphere, disagreement was found in one of the coefficients presented by McBride et al [33]. This will be addressed in a letter to the Journal of Applied Physics in the near future.

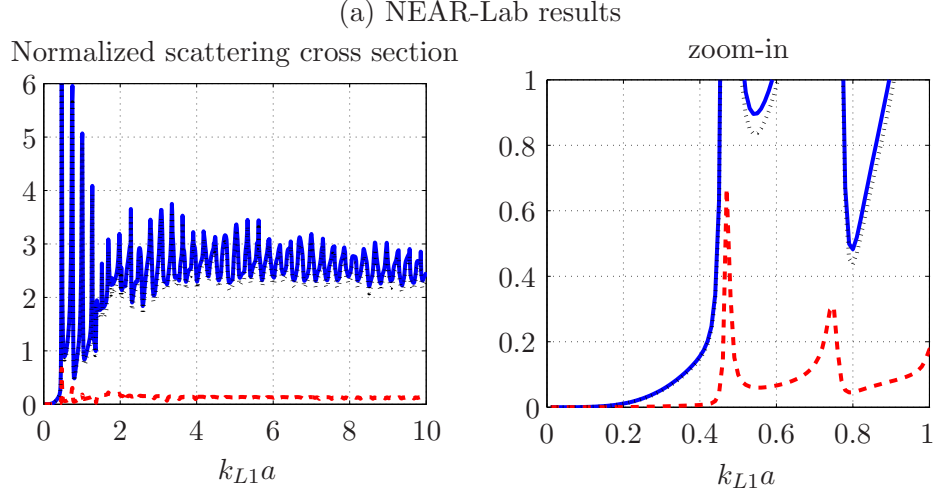


Figure 4.1: (a) Scattering of a shear wave incident upon a spherical elastic inclusion with $c_{Lp} = 6000$ m/s, $c_{Tp} = 3500$ m/s, and $\rho_p = 2700$ kg/m³, surrounded by elastic media with $c_{L1} = 1400$ m/s, $c_{T1} = 0.1$ m/s, and $\rho_1 = 1000$ kg/m³. The blue line corresponds to the normalized cross section, the black line represents the portion of energy scattered as a shear wave and the red line is the energy scattered as a longitudinal wave. (b) Similar results found in the literature are shown for comparison.

between any pair of sub-bottom layers. The coefficients in this section are those presented by Brekhovskikh [34]. These expressions were coded by the author

using MATLAB, and the results are utilized to solve the vector RT equation in [3.10].

4.2.1 Plane wave reflection coefficients for a fluid-solid interface

Reflection and transmission coefficients for elastic media must account for the polarization of the incident, reflected and transmitted waves. In liquid media, only longitudinal waves are supported, while in solid media, longitudinal, shear vertical and shear horizontal polarizations can propagate. Figure 4.2 (a) shows an incident longitudinal wave from the fluid medium that results in a reflected longitudinal wave, and transmitted shear vertical and longitudinal waves (the transmitted shear horizontal wave is always zero). The transmitted waves are refracted into angles that obey Snell's law (4.7):

$$\frac{\sin \theta_0^L}{c_{L0}} = \frac{\sin \theta_1^L}{c_{L1}} = \frac{\sin \theta_1^y}{c_{T1}}. \quad (4.7)$$

Since the reflection and transmission coefficients depend on the interface as well as in the polarization of the incident wave, a new nomenclature of the form T_{cd}^{ab} and R_{cd}^{ab} is now introduced. The super index indicates the transformation from polarization a into b , and the subindex indicates the boundary between layers c and d , where c is the layer corresponding to the excitation. Expressions for the reflection and transmission coefficients for the cases illustrated in Fig. 4.2 can be

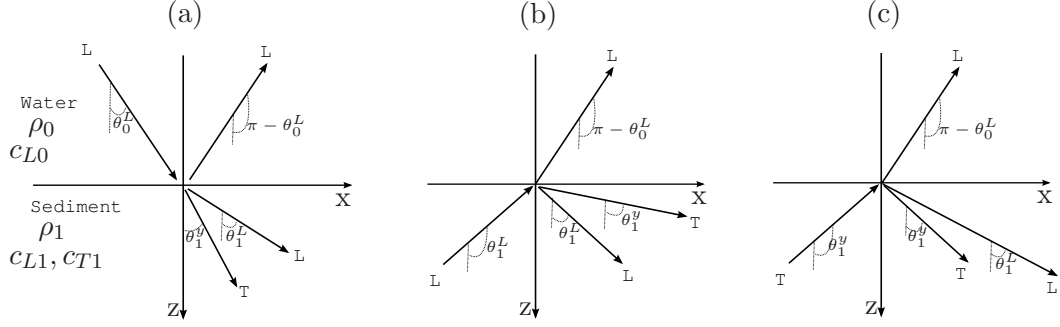


Figure 4.2: (a) A longitudinal wave in fluid media impinges upon a fluid-sediment interface, producing a reflected longitudinal wave and transmitted longitudinal and shear vertical waves; (b) A longitudinal wave in the sediment excites a longitudinal wave in the fluid and reflected longitudinal and transverse waves in the sediment; (c) Similar to (b) for an incident shear vertical wave in the sediment. In all cases, the refracted angles are defined by Snell's law stated in (4.7).

found in the literature [34]. For a L wave incident from the fluid (Fig. 4.2(a)),

$$R_{01}^{LL} = \frac{Z_{L1} \cos^2 2\theta_1^y + Z_{T1} \sin^2 2\theta_1^y - Z_{L0}}{Z_{L1} \cos^2 2\theta_1^y + Z_{T0} \sin^2 2\theta_1^y + Z_{L0}};$$

$$T_{01}^{LL} = \frac{\rho_0}{\rho_1} \frac{2Z_{L1} \cos 2\theta_1^y}{Z_{L1} \cos^2 2\theta_1^y + Z_{y1} \sin^2 2\theta_1^y + Z_{L0}}; \quad (4.8)$$

$$T_{01}^{Ly} = -\frac{\rho_0}{\rho_1} \frac{2Z_{y1} \sin 2\theta_1^y}{Z_{L1} \cos^2 2\theta_1^y + Z_{y1} \sin^2 2\theta_1^y + Z_{L0}}.$$

If the L wave is incident from the sediment (Fig. 4.2(b)):

$$R_{10}^{LL} = \frac{Z_{L0} + Z_{y1} \sin^2 2\theta_1^y - Z_{L1} \cos^2 2\theta_1^y}{Z_{L0} + Z_{1y} \sin^2 2\theta_1^y + Z_{y1} \cos^2 2\theta_1^y},$$

$$R_{10}^{Ly} = \left(\frac{c_{T1}}{c_{L1}} \right)^2 \frac{\sin 2\theta_1^L}{\cos 2\theta_1^y} (1 - R_{10}^{LL}); \quad (4.9)$$

$$T_{10}^{LL} = \frac{c_{L0} \cos \theta_1^L}{c_{L1} \cos \theta_0^L \cos^2 2\theta_1^y} (1 - R_{10}^{LL}).$$

For an incident shear vertical wave in the sediment (Fig. 4.2(c)):

$$R_{10}^{yy} = -\frac{Z_{L0} + Z_{L1} \cos^2 2\theta_1^y - Z_{y1} \sin^2 2\theta_1^y}{Z_{L0} + Z_{L1} \cos^2 2\theta_1^y + Z_{y1} \sin^2 2\theta_1^y},$$

$$R_{10}^{yL} = -\left(\frac{c_{L1}}{c_{T1}} \right)^2 \frac{\cos 2\theta_1^y}{\sin 2\theta_1^L} (1 + R_{10}^{yy}); \quad (4.10)$$

$$T_{10}^{yL} = \frac{\tan 2\theta_0^L}{2 \sin^2 \theta_1^y} (1 + R_{10}^{yy}).$$

Finally, a shear horizontal wave in the sediment will be totally reflected, which results in $R_{10}^{xx} = 1$ and $R_{10}^{xL} = R_{10}^{xy} = T_{10}^{xL} = 0$.

The coefficients presented in this section for a fluid-sediment interface are written in terms of plane waves, but those coefficients must be adjusted when working with the specific intensity [14, 21]. A summary of the relation between

plane wave coefficients, power coefficients (indicated by \sim) and specific intensity coefficients (indicated by $\hat{\cdot}$) according to [14] is given in table 4.1.

Table 4.1: Power (\sim) and Specific Intensity ($\hat{\cdot}$) reflection/transmission coefficients for the fluid-elastic interface.

Incident	Power coefficient	Specific intensity
L (fluid)	$\tilde{R}_{01}^{LL} = R_{01}^{LL} ^2$ $\tilde{T}_{01}^{LL} = T_{01}^{LL} ^2 \frac{\rho_1 \tan \theta_0^L}{\rho_0 \tan \theta_1^L}$ $\tilde{T}_{01}^{Ly} = T_{01}^{Ly} ^2 \frac{\rho_1 \tan \theta_0^L}{\rho_0 \tan \theta_1^y}$	$\hat{R}_{01}^{LL} = R_{01}^{LL} ^2$ $\hat{T}_{01}^{LL} = T_{01}^{LL} ^2 \frac{c_{L1}^2}{c_{L0}^2}$ $\hat{T}_{01}^{Ly} = T_{01}^{Ly} ^2 \frac{c_{T1}^2}{c_{L0}^2}$
L (sediment)	$\tilde{R}_{10}^{LL} = R_{10}^{LL} ^2$ $\tilde{T}_{10}^{LL} = T_{10}^{LL} ^2 \frac{\rho_0 \tan \theta_1^L}{\rho_1 \tan \theta_0^L}$ $\tilde{R}_{10}^{Ly} = R_{10}^{Ly} ^2 \frac{\tan \theta_1^L}{\tan \theta_1^y}$	$\hat{R}_{10}^{LL} = R_{10}^{LL} ^2$ $\hat{T}_{10}^{LL} = T_{10}^{LL} ^2 \frac{c_{L0}^2}{c_{L1}^2}$ $\hat{R}_{10}^{Ly} = R_{10}^{Ly} ^2 \frac{c_{T1}^2}{c_{L1}^2}$
y (sediment)	$\tilde{R}_{10}^{yy} = R_{10}^{yy} ^2$ $\tilde{T}_{10}^{yL} = T_{10}^{yL} ^2 \frac{\rho_0 \tan \theta_1^y}{\rho_1 \tan \theta_0^L}$ $\tilde{R}_{10}^{yL} = R_{10}^{yL} ^2 \frac{\tan \theta_1^y}{\tan \theta_1^L}$	$\hat{R}_{10}^{yy} = R_{10}^{yy} ^2$ $\hat{T}_{10}^{yL} = T_{10}^{yL} ^2 \frac{c_{L0}^2}{c_{T1}^2}$ $\hat{R}_{10}^{yL} = R_{10}^{yL} ^2 \frac{c_{L1}^2}{c_{T1}^2}$

A simulation of the power coefficients can help to illustrate the relation between the incident and excited waves. Figure 4.3(a) shows an example of the reflection/transmission coefficients for the case illustrated in Fig. 4.2 (a). The simulation corresponds to $c_{L0} = 557$ m/s, $\rho_0 = 664$ kg/m³, $c_{L1} = 1670$ m/s, $\rho_1 = 1992$ kg/m³ and c_{T1} varying from 928 m/s to 1044 m/s, and it matches with published results [34] shown in Fig. 4.3(b).

4.2.2 Plane wave reflection coefficients for a solid-solid interface

In this work, sub-bottom layers are modeled as elastic media in which all polarizations (longitudinal, shear vertical and shear horizontal) are supported

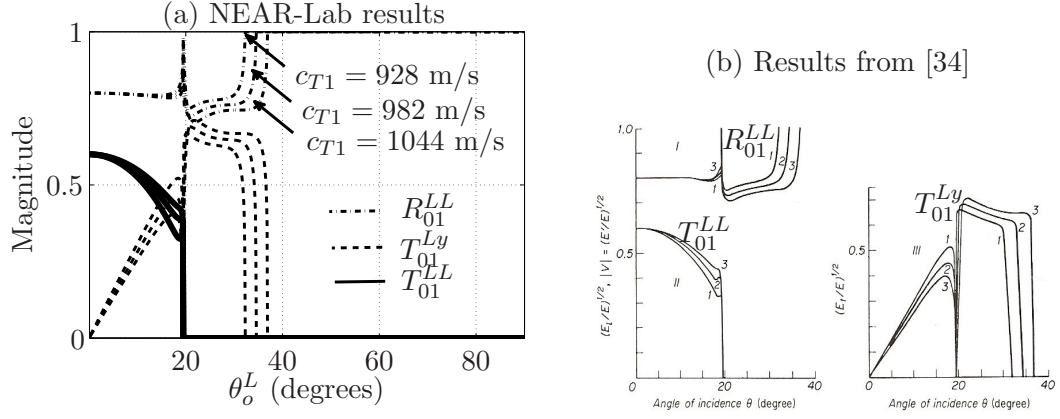


Figure 4.3: (a) Example of the computation of (4.8) for $c_{L0} = 557$ m/s, $\rho_0 = 664$ kg/m³, $c_{L1} = 1670$ m/s, $\rho_1 = 1992$ kg/m³ and c_{T1} varying from 928 m/s to 1044 m/s; (b) Similar results can be found in the literature.

in both sides of an interface. Figure 4.4 shows the possible combinations of incident/reflected/transmitted waves for an elastic-elastic interface. Snell's law can now be written as

$$\frac{\sin \theta_1^L}{c_{L1}} = \frac{\sin \theta_1^y}{c_{T1}} = \frac{\sin \theta_2^L}{c_{L2}} = \frac{\sin \theta_2^y}{c_{T2}}. \quad (4.11)$$

The reflection and transmission coefficients for the three cases in Fig. 4.4 can be found in the literature [34]. For an incident shear horizontal wave there is no cross-polarization, so the transmission and reflection coefficients R_{12}^{xx} and T_{12}^{xx} completely describe this interaction.

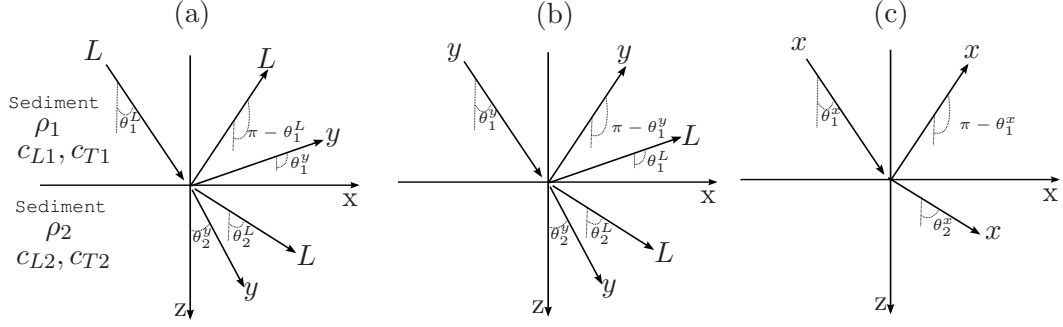


Figure 4.4: (a) A longitudinal wave in elastic media impinges upon a sediment-sediment interface, producing transmitted/reflected longitudinal and shear vertical waves; (b) Same as (a) for an incident shear vertical wave; (c) Shear horizontal waves only excite transmitted/reflected waves with the same polarization. In all cases, the refracted angles are defined by Snell's law stated in (4.11).

4.3 Solution of the steady-state RT equation

The solution method presented in section 3.2.4 for the RT vector equation including multiple scattering was implemented in MATLAB. In this section, simulated results of the specific intensity propagating through random media are presented and compared to results published by Turner et al [13].

Figure 4.5 shows a diagram of the simulated environment, which consists of an infinite half space ($\tau_d \rightarrow \infty$) with $c_{L0} = c_{L1} = 2000$ m/s, $c_{T0} = c_{T1} = 1000$ m/s, $\eta = 2.6e^{14}$ scatterers/m³, $f = 318.3$ kHz, $a = 0.5$ μ m and $\rho_0 = \rho_1 = 1000$ kg/m³. The specific intensity $\underline{I}_d(\mu, \phi, \tau)$ can be computed at the surface of the layer containing scatterers (Fig. 4.5(a)) or at any arbitrary depth z_1 into the media (Fig. 4.5(b)) as a function of the angle θ .

For these simulations, the excitation is a fixed source located at $z < 0$ with

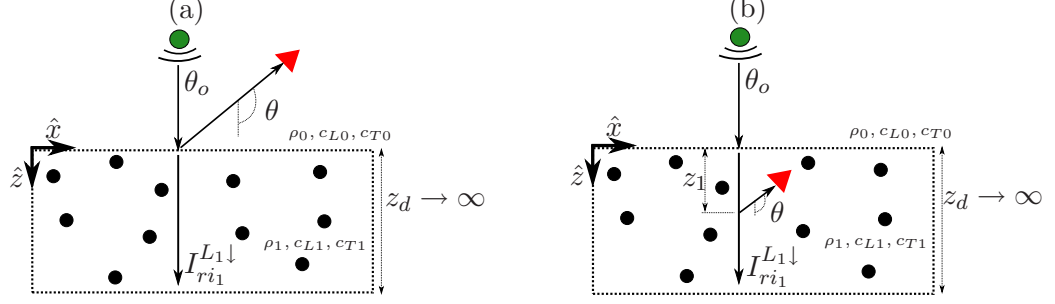


Figure 4.5: Measurement of the diffuse intensity as a function of angle θ in an infinite half space at $z = 0$ m (a) and at $z = z_1$ m (b).

longitudinal polarization and $\phi_o = 0$ and $\theta_o = 0$ (normal incidence). Since the acoustic impedance of layer 1 and layer 2 are the same, there are no internal reflection of energy at the boundary $z = 0$ m. Then, the only reduced intensity from (3.19) and (3.21) different than zero is $I_{ri_1}^{L_1\downarrow}$ and (3.27) simplifies to

$$\begin{aligned} \mu \frac{\partial \underline{I}_d(\mu, \phi, \tau)}{\partial \tau} = & -\tilde{\sigma} \underline{I}_d(\mu, \phi, \tau) + \\ & \frac{1}{4\pi\kappa_T} \left[\int_{-1}^1 \int_0^{2\pi} \underline{P}(\mu, \phi; \mu', \phi') \underline{I}_d(\mu', \phi', \tau) d\mu' d\phi' \right] \\ & + \underline{S}_1^{L_1\downarrow}(\mu, \phi) e^{-\frac{\tilde{\sigma} L_1 \tau}{\mu_1^{L_1}}}; \end{aligned} \quad (4.12)$$

with the boundary conditions

$$\begin{aligned} \underline{I}_d(\mu > 0, \phi, \tau = 0) &= 0; \\ \underline{I}_d(\mu < 0, \phi, \tau \rightarrow \infty) &= 0. \end{aligned} \quad (4.13)$$

One of the main advantages of the RT formulation is that the results can be easily related to physical phenomena, and this provides a better understanding

of the nature of the problem, as illustrated with the following simulations.

4.3.1 Dependency of the steady state solution on the absorption

As mentioned before, the total cross section $\sigma_t = \kappa_s + \nu$ is the summation of scattering (which is a re-distribution of energy) and absorption (which is actual loss of mechanical energy when it is transformed into heat). Figure 4.6 (a) and (b) show the value of the specific intensities $I_{dL}(0 < \mu < -1, \phi = 0, \tau = 0)$, $I_{dx}(0 < \mu < -1, \phi = 0, \tau = 0)$ and $I_{dy}(0 < \mu < -1, \phi = 0, \tau = 0)$, measured at $z = 0$ for angles $\pi/2 < \theta < \pi$. In each case, the single scattering solution (i.e. the solution of (4.12) ignoring the double integral) is shown in dashed lines for comparison with the full solution, in solid lines.

Figure 4.6 (a) corresponds to *normalized* absorptions³ of $\tilde{\nu}_T = 0.111$ and $\tilde{\nu}_L = 0.0555$ (low absorption) while Fig. 4.6 (b) corresponds to $\tilde{\nu}_T = 4$ and $\tilde{\nu}_L = 2$ (high absorption). In both cases, the results obtained by using the NEAR-Lab implemented routine are compared to the results by Turner et al [13]. In this figure, solid lines correspond to the full solution of the RT equation, while dashed lines are the single scattering solutions (i.e. the solutions obtained by ignoring the double integral in (3.10)).

By comparing the low and high absorption simulations, two conclusions can be made:

³Similar to (3.11), the normalized absorption is defined as $\tilde{\nu}_L = \nu_L/\kappa_T$ and $\tilde{\nu}_T = \nu_T/\kappa_T$

1. The magnitude of the specific intensity is higher for the low absorption case, as expected. For example, the peak of the longitudinal specific intensity has a magnitude of 0.4 for the low absorption case, and it decreases to 0.055 in the high absorption case.
2. For high absorption, the full solutions (solid lines) converge to the single scattering solutions (dashed lines). This behavior can be explained by considering that in lossy media a large portion of energy is lost after each scattering event, and therefore the contribution of the multiple scattering term is very small.

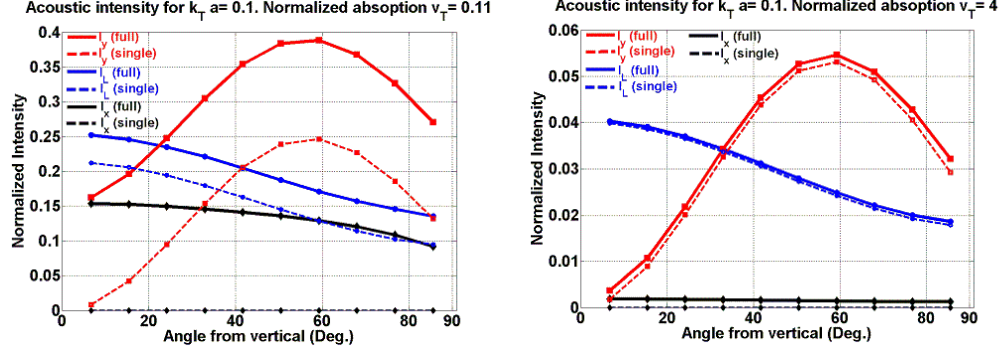
The second point is very important in applications of ocean acoustics at high frequencies, because the acoustic attenuation of sediments is large and this would allow ignoring the multiple scattering effect.

4.3.2 Dependency of the steady state solution on the depth

Simulations of the specific intensity at different depths into the random media (Fig. 4.5(b)) can also be computed for $0 < \theta < \pi$, as shown in Fig. 4.7. The simulation parameters are the same as in section 4.3.1, except that the absorptions ν_L and ν_T are set to zero. Note that the horizontal line at each depth indicates $\mu = 0$ (where μ was defined following (3.4)) and not the interface at $z = 0$.

The simulations were run at normalized depths $\tau = 0, \tau = 0.5, \tau = 1, \tau = 3$

(a) NEAR-Lab results



(b) Results from Turner et al. [13]

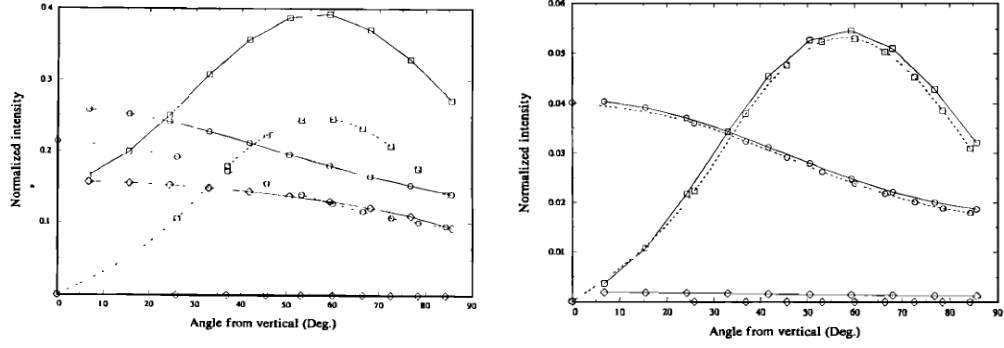


Figure 4.6: The diffuse intensities $I_{dL}(0 < \mu < -1, \phi = 0, \tau = 0)$, $I_{dx}(0 < \mu < -1, \phi = 0, \tau = 0)$ and $I_{dy}(0 < \mu < -1, \phi = 0, \tau = 0)$ corresponding to the measurement depicted in Fig. 4.5(a): (a) Solution obtained at the NEAR-Lab for low absorption (left) and high absorption (right) of $\tilde{\nu}_T = 0.111$ and $\tilde{\nu}_L = 0.0555$, respectively. In both cases, the single scattering solution (dashed lines) is shown for comparison with the full solution (solid lines); (b) Results found in the literature for comparison.

and $\tau = 5$. When $\tau = 0$, due to the BC in (4.13), the downward diffuse intensities are zero for $0 < \theta < \pi/2$. Physically, this can be explained by remembering that the diffuse intensity can only be generated as the result of the interaction between coherent energy and the scatterers. Since there are no scatterers at $z < 0$, then no diffuse intensity propagates downwards at $z = 0$.

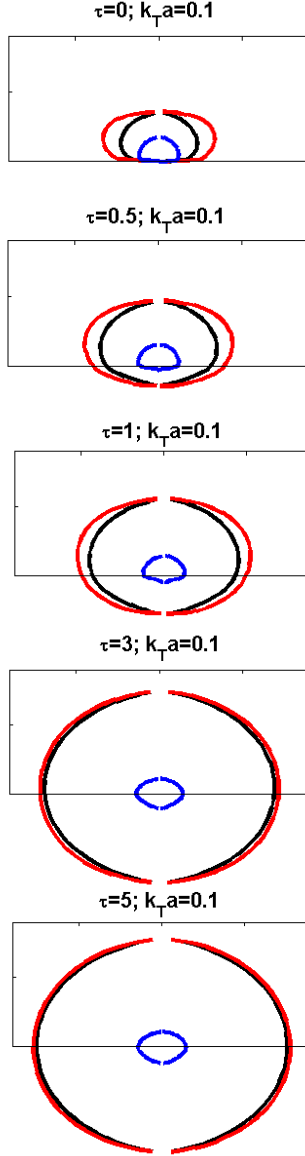
As the depth increases to $\tau = 0.5$, some downward diffuse intensity is observed, and this is due to the contributions from the scatterers located at $0 < \tau < 0.5$. At large depths, when $\tau \geq 5$, a similar number of scatterers contribute to the intensity from any direction ⁴, and this results in isotropic intensity. This is a well known effect in scattering from random media, known as the *isotropic diffusion limit*.

4.4 Solution of the transient RT equation

As mentioned in section 3.3, the time dependency of the specific intensity can be obtained by including the term $\partial \underline{I}(\mu, \phi, \tau, \xi)/\partial \xi$ in (3.55), where $\xi = \eta c_T \kappa_T t$ is a normalized time variable. Recent research on characterization of materials by ultrasound [15] (as well as applications of ultrafast lasers in electromagnetics [24]), suggests that information about the internal structure of the random media can be extracted from the time-dependent characteristics of the scattered intensity. As an example, Fig.4.8 shows a simulation of the longitudinal specific intensity $I_L(\mu, \phi, \tau, \psi)$ when the scattering media is an infinite layer of polycrystalline iron ($c_L = 5900$ m/s, $c_T = 3230$ m/s), and the incident energy is a short pulse of ultrasound energy with a carrier frequency of $f = 15$ MHz at normal incidence. The specific intensity as a function of time is simulated at angles

⁴Even though there is an infinite number of scatterers as $z \rightarrow \infty$ in Fig. 4.5, only the ones close to the measurement point contribute to the scattering. This is due to the fact that the specific intensity attenuates as $e^{-\tau}$.

(a) NEAR-Lab results



(b) Results from Turner et al. [35]

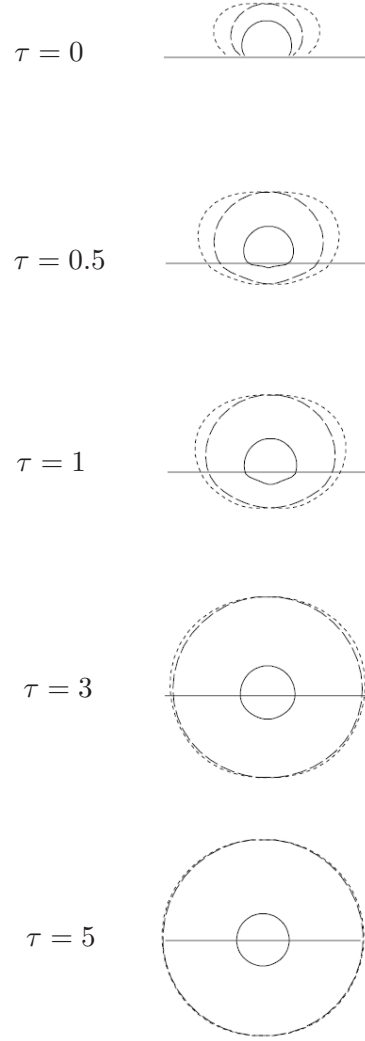


Figure 4.7: (a) Depth dependency of the diffuse intensities $I_{dL}(\mu, \phi = 0, \tau)$ (blue), $I_{dx}(\mu, \phi = 0, \tau)$ (black) and $I_{dy}(\mu, \phi = 0, \tau)$ (red) corresponding to the measurement depicted in Fig. 4.5(b) at five depths: $\tau = 0$, $\tau = 0.5$, $\tau = 1$, $\tau = 3$ and $\tau = 5$. The horizontal line at each depth indicates $\mu = 0$. (b) Results found in the literature for comparison.

$\theta = 0^\circ$ (blue), $\theta = 49^\circ$ (red) and $\theta = 76^\circ$ (black), and the author proposed [15] that information about the directivity of the random media (i.e. if the media is isotropic, or if the media tends to scatter energy in the forward direction) can be obtained from the time difference between the maximum of the specific intensity at each angle.

In geoacoustic inversion, the time domain solutions of the scattered intensity can be used to invert for the total attenuation (due to background+scattering) of the sediment, by utilizing a broadband chirp with a known envelope as a probe and analyzing the change in the shape of such an envelope[36]. The potential for this kind of analysis motivated the implementation of the time domain solution in the proposed RT model for seabed scattering. Simulations of transient RT solutions with realistic parameters for the seabed will be presented in section 7.

4.5 Conclusion

In this section, numerical examples for each of the main computational modules of the RT model were presented and compared to published results, and some insight into the re-distribution of energy between the three polarization components supported by elastic media was provided. This partition of energy into longitudinal, shear vertical and shear horizontal polarizations can take place at the interfaces between layers, or at the boundaries of the scatterers. Finally,

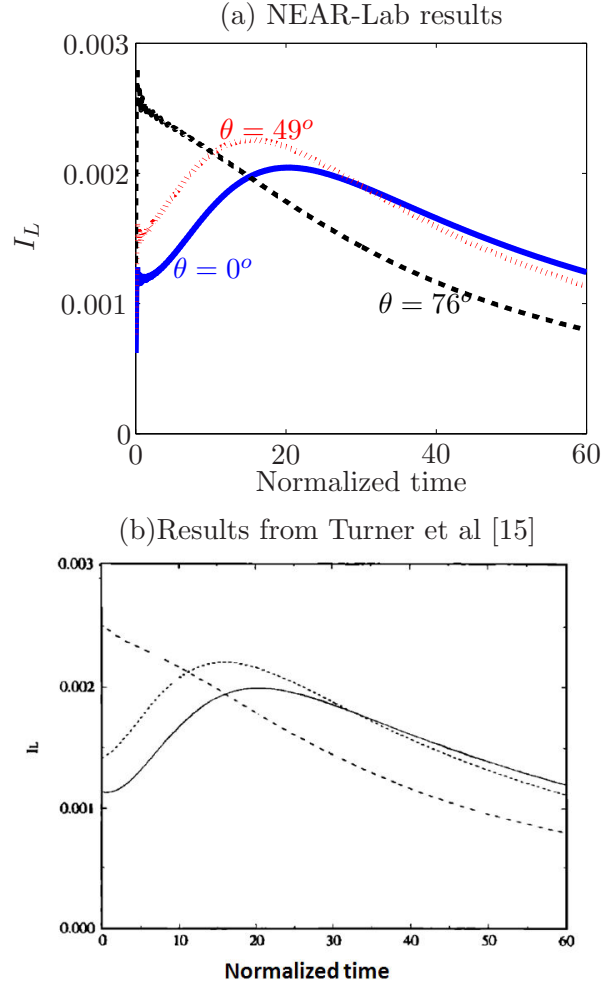


Figure 4.8: (a) Example of the structure information that can be obtained from time domain solutions of the RT equation. In this simulation, the specific intensity as a function of time is simulated at angles $\theta = 0^\circ$ (blue), $\theta = 49^\circ$ (red) and $\theta = 76^\circ$ (black). (b) Results found in the literature are shown for comparison.

results of the steady-state and transient RT formulation obtained by Turner et al [13] for infinite halfspaces were obtained as a limiting case of the finite layer formulation presented in section 3.2. In the next sections, the RT model is compared to experimental data obtained in a tank setup, as well as from field experiments.

Chapter 5

Scaled tank experiments and comparison with the radiative transfer model

In this section, the experimental work for the validation of the proposed RT model is described. The section begins with a description of the experimental setup and the procedure to verify the calibration of the system. Then, the method to compute the experimental scattering cross section $\Upsilon_{av}(f, \theta_i)$ is explained, followed by the results from three experiments in which the effect of different combinations of scatterers, background material, and concentration is explored. In all cases, Υ_{av} is compared to the theoretical cross section computed from the RT model. Table 5.1 summarizes the background material and scatterers used in each experiment. These parameters, together with the frequency-dependent background attenuation, thickness of the slab and concentration of scatterers are the inputs to the RT model.

Table 5.1: Acoustic properties of the scattering media used in this work. Most of the values for the sand background were measured in the laboratory, as detailed in section 5.4.

	Experiment 1 [37]		Experiment 2 [38]		Experiment 3	
Material	Water	Aluminum	Sand	Aluminum	Resin	Glass
ρ_1 (kg/m ³)	1000	2700	1710	2700	1251	2539
c_{L1} (m/s)	1468	6290	1676	6290	1020	5231
c_{T1} (m/s)	1	3260	10	3260	1	3124

5.1 Experimental setup and calibration

Scaled tank experiments were performed using ultrasound excitation sources in the band 250 *kHz* to 450 *kHz* (with corresponding wavelengths of $\lambda = 6$ *mm* and $\lambda = 3$ *mm*, respectively). In scattering theory, three regimes can be defined according to the size of the scatterers (denoted as a) with respect to the wavelength: the Rayleigh regime ($\lambda \gg a$), the Mie regime ($\lambda \approx a$) and the Geometric Optics regime ($\lambda \ll a$). Since the scattering characteristics of the individual inhomogeneities are computed from the analytical coefficients A_m , B_m , a_m , b_m , and d_m (section 4.1) and those coefficients account for the scatterer size relative to the wavelength, the RT model must be able to make reasonable predictions in all regimes.

The validation experiments were performed at the Northwest Electromagnetics and Acoustics Research Laboratory (NEAR-Lab) in a rectangular tank of

dimensions 5x7x3 feet shown in Fig. 5.1(a), filled with fresh water¹ with a measured sound speed $c_{L0} = 1468$ m/s. The size of the tank allows time gating of the returns coming from the sample, and the returns from the walls of the tank can be excluded from the analysis. Figure 5.1(b) illustrates the interconnection between the sensors, data acquisition hardware, voltage amplifier and signal conditioner used in this series of experiments.

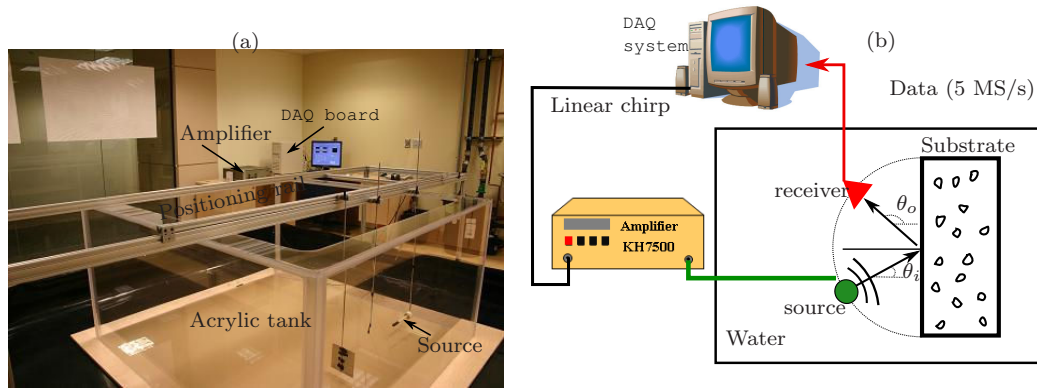


Figure 5.1: (a) Photograph of the equipment available to perform ultrasound scattering experiments, including a 5x7x3 feet tall acrylic tank, aluminum rail for sensor positioning, amplifiers and a PCI 6110 DAQ board; (b) Diagram of the connection of the hardware elements used in this series of experiments.

A multipurpose Data Acquisition (DAQ) board PCI-6110 (National Instruments) with 2 analog output channels (4 MS/s, 16 bit resolution) and 4 simultaneously sampled input channels (5 MS/s, 12 bit) was used to transmit the excitation pulse and to record the signal scattered by the random media. The acquisition was controlled by a graphic user interface programmed in Labview

¹The levels of salinity found in field experiments can be included in the model by adjusting the sound speed in the fluid layer to higher values around 1520 m/s.

by the author. The excitation was amplified to ± 20 volts by a power amplifier Krohn-Hite 7500, driving a piston shaped projector (Panametrics A391S) used as the acoustic source. The receiver was a TC4038 omni directional hydrophone (Reson) with a flat frequency response in the frequency band of operation. Before digitalization, the received signal was amplified by 50 dB using a VP2000 preamplifier (Reson). The source and the receiver were fixed to a rigid arm, driven by a rotary stage (Vemex B4836TS) that varied the angle of incidence θ_i .

The angle- and frequency-dependent volume scattering was measured by transmitting linear chirps with duration of 18 ms in the frequency band of 250 kHz to 450 kHz, and pulse compression was used to obtain time resolution and distinguish the returns from the scattering media, the walls of the tank and other supporting structures. In all cases, both the incident and scattered pulses were recorded at the hydrophone and compensated for spherical spreading using the lengths L and R indicated in Fig. 3.12(b).

As a preliminary step to verify the calibration of the measurement system, scattering from a single sphere suspended in the water tank was measured and compared to the analytical solution explained in section 4.1. Figure 5.2 shows the results for spheres of tungsten-carbide and steel with radius $a = 1.9$ cm and $a = 1.03$ cm, respectively. The spectrum of the scattered wave was normalized by the spectrum of the incident wave.

In this kind of calibrations, the most important features to match are the location of resonance peaks as a function of the parameter ka , as well as having a mean scattering level within a few dB units relative to the model. For example, in Fig.5.2(a) the model predicts a mean scattering level around -40 dB, similar to the experimental data for $20 < ka < 35$. In this range, the discrepancy between measured and simulated scattering is less than 2.2 dB except at points where the model predicts deep nulls, which are typically “filled” by noise in experimental data. The location of those nulls at $ka = 19.6, 22.4, 25.1, 27.9, 30.82$ and 33.9 is clearly observed in the experimental and simulated data. Due to the frequency response of the transducers and amplifiers, the power of the transmitted pulse is reduced for $ka < 20$ and $ka > 35$, leading to edge effects after normalizing the scattered pulse by the incident pulse. This explains the higher discrepancies between experiment and model observed at these intervals of ka .

The calibration using the tungsten carbide sphere is a best case scenario, due to the large size of the sphere and strong acoustic contrast of this material which favors signal-to-noise ratio in the measurements. In addition, the rigidity of tungsten carbide reduces the number of resonances as compared to other spheres of similar size, providing experimental data with less complicated features and easier to match with the model. In contrast, Fig.5.2(b) shows the case of the much smaller steel sphere, for which lower levels of scattering are obtained. Despite

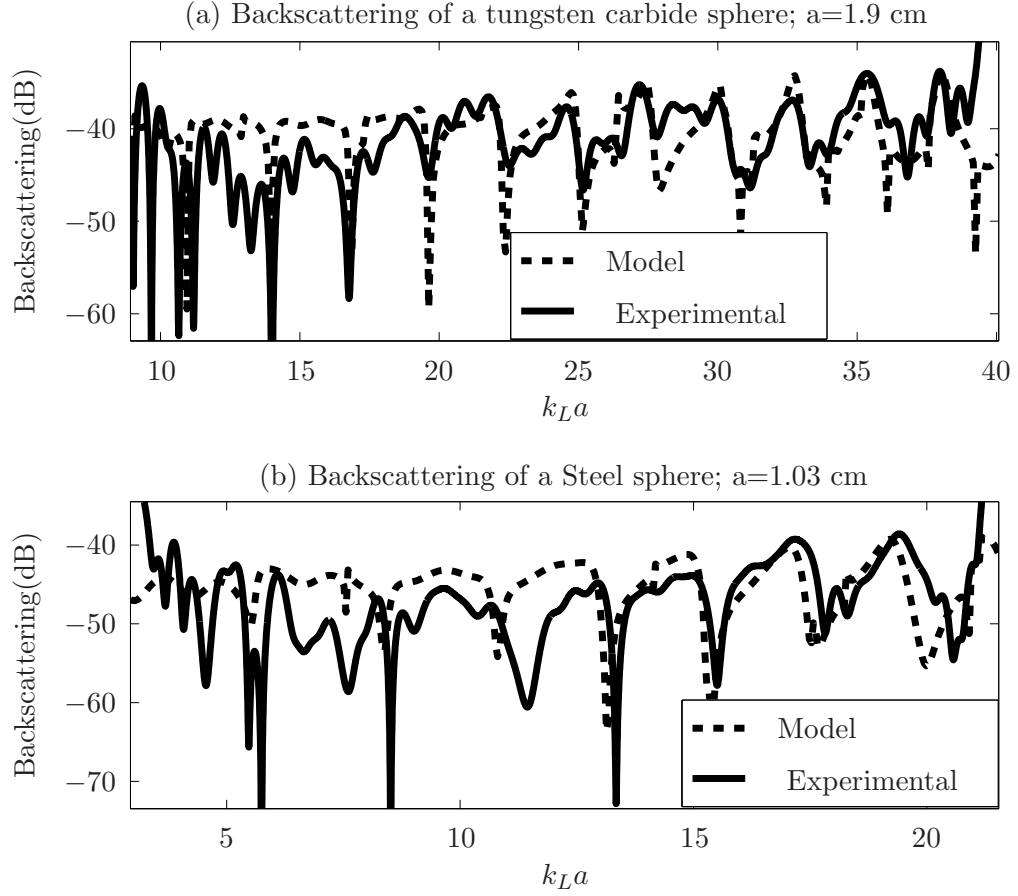


Figure 5.2: Comparison between the measured backscattered energy and the Mie analytical solution (section 4.1) for single spheres of (a) tungsten-carbide with radius $a = 1.9$ cm and (b) steel with radius $a = 1.03$ cm. These measurements verify the system calibration as a preliminary step to the experiments with random media.

this, the discrepancy between model and experimental data for $12.8 < ka < 19.4$ is less than 2.2 dB, and the prediction of the nulls within this range is still accurate.

5.2 Processing of experimental data

Referring to Fig. 3.12(b), the angle-dependent scattering from the random medium was measured at each angle θ_i , with N realizations taken by laterally shifting the slab in the $\pm x$ direction. This assures that each realization corresponds to a different ensemble of scatterers. The frequency dependent backscattering of the n^{th} realization for an angle of incidence θ_i was computed as:

$$\Upsilon_n(f, \theta_i) = C \frac{|\mathcal{F}(w_n^s(t, \theta_i))|^2}{|\mathcal{F}(w_n^i(t, \theta_i))|^2}, \quad (5.1)$$

where f is the frequency in Hz, C is a compensation factor for spherical spreading, $w_n^s(t, \theta_i)$ and $w_n^i(t, \theta_i)$ are the time-gated scattered and direct arrivals, \mathcal{F} indicates the Fourier transform and $|\cdot|$ is the absolute value. Figure 5.3 in section 5.3 shows examples of the time gating applied to the acoustic echoes from a single sphere and an ensemble of spheres.

The estimated average backscattering $\Upsilon_{av}(f, \theta_i) = (1/N) \sum_{n=1}^N \Upsilon_n(f, \theta_i)$ and its standard deviation are used in the next sections to compare experimental results to simulations from the RT model.

5.3 Experiment 1: Aluminum scatterers in water background

This experiment was performed with aluminum spheres of radius $a = 0.24$ cm, suspended with nylon filament and positioned randomly at the center of a wooden frame as shown in Fig. 5.3(a). Scattering from the supporting filaments was negligible, as determined by preliminary measurements. This configuration has two main advantages for testing the RT model: first, the background medium is water, which for small propagation ranges can be assumed to be lossless. Second, large spheres result in strong scattered waves, which favors the signal to noise ratio of the recorded data. Examples of the measured time domain signals after pulse compression are shown in Fig. 5.3(b), corresponding to a single sphere and to an ensemble of spheres. In both cases, the scattered pulse can be time gated to extract $w_n^s(t, \theta_i)$, used in (5.1) to estimate the scattering cross section.

The method for positioning the scatterers allowed variation of the fractional volume step by step, starting from a single sphere up to fractional volumes of 0.9 % and 2.7 %. For this experiment only normal incidence measurements ($\theta_i = 0$) were considered. From Fig. 3.12(b), the relative location of the source, receiver and slab are $L = 18$ cm and $R = 36$ cm, which results in an illuminated patch of area $dA = 0.028$ m² given the radiation pattern of the source. This value is required as an input to the RT model, as explained in section 3.5.

Figure 5.4 shows the scattering measured from a single sphere compared to

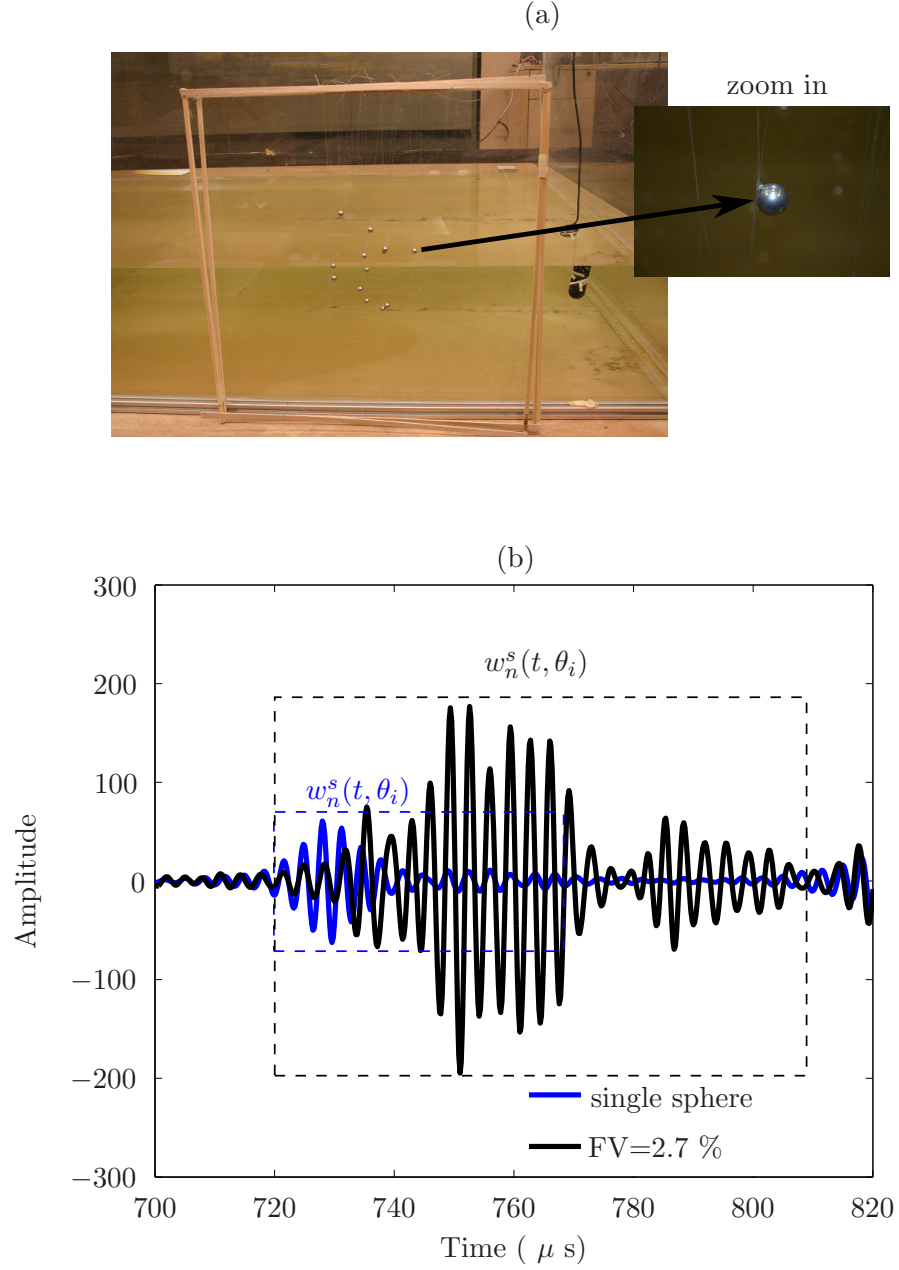


Figure 5.3: (a) Photograph of an ensemble of aluminum spheres suspended with nylon filament in the center of a wooden frame; (b) Example of time domain realizations of the scattered signal from a single sphere and from the ensemble of spheres corresponding to a fractional volume $FV = 2.7$ %. The dashed boxes indicate the time gating used to define $w_n^s(t, \theta_i)$ in (5.1).

the theory (section 4.1). The measured scattering cross section $\Upsilon_{av}(f, \theta_i = 0)$ is also shown in the frequency band 280 kHz to 340 kHz with fractional volume as a parameter. In all cases, the backscattering levels computed with the RT model as in (3.72) are shown as dashed lines and they resemble the experimental results.

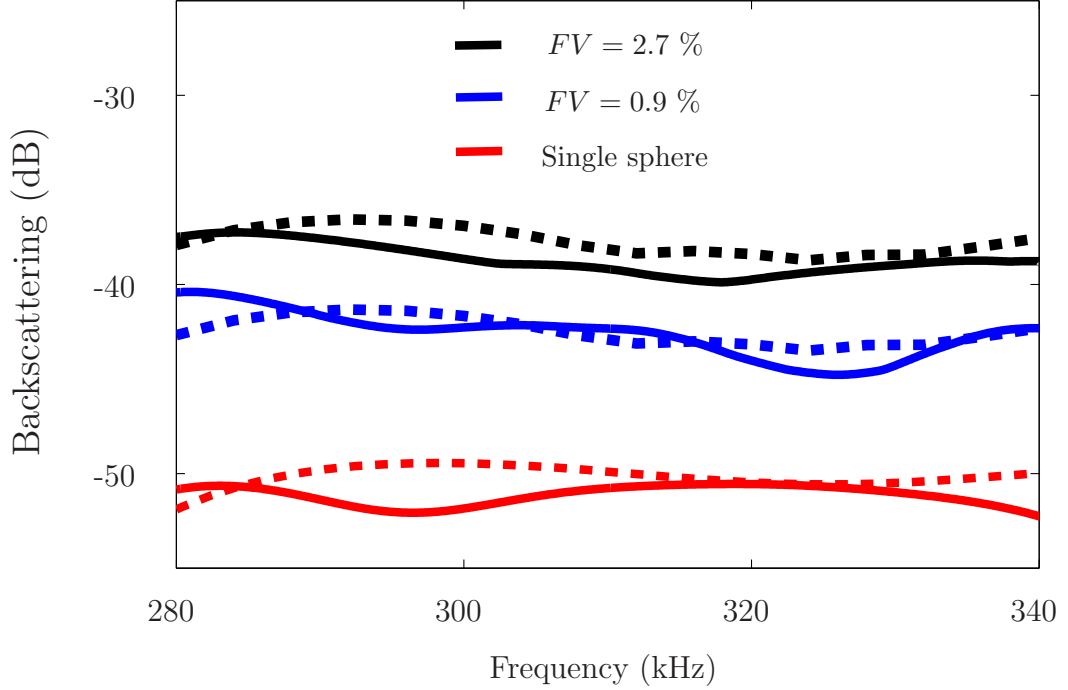


Figure 5.4: Comparison of the measured backscattering $\Upsilon_{av}(f, \theta_i = 0)$ (solid lines), with computations from the RT model for an ensemble of aluminum spheres, with fractional volume (FV) as a parameter. For reference, experimental and theoretical scattering from a single sphere are also shown.

The experiment presented in this section evaluates the performance of the RT model for varying frequency and fractional volume. Nevertheless, more strict tests are warranted in which other phenomena such as a frequency-dependent

background attenuation and the effect of energy reflection at the slab-water interface are included, which is the subject of the following experiments.

5.4 Experiment 2: Aluminum scatterers in sand background

The next level of complexity in these series of experiments was the addition of a background material to hold the aluminum spheres. In this experiment, a box with dimensions 60x60x12 cm was submerged in the water and filled with fine sand, with a grain size between 200 μm and 400 μm . The sand was not centrifuged, so the presence of trapped air bubbles was expected. The fractional volume for this experiment was kept constant at $FV = 5\%$.

5.4.1 Characterization of the sand

Reasonable values for the acoustic parameters of the sand could be found in tables, classified according to grain size[8]. Nevertheless, in order to increase the accuracy some of those parameters were measured in the laboratory prior to the inclusion of scatterers. The procedure to invert the acoustic parameters of the sand substrate can be summarized as follows:

1. Based on the grain size, the longitudinal and shear sound speeds of the sediment are assigned as $c_{L1} = 1676$ m/s and $c_{T1} = 120$ m/s, according to Jackson et al [8].

2. A broadband pulse at normal incidence was transmitted, and the incident and scattered waves were recorded, as shown in Fig. 5.5(a). Three peaks can be distinguished: the one corresponding to the incident pulse (labeled I_o), the energy reflected from the water-sand interface (I_1), and the pulse reflected from the bottom of the tank (I_2). Note in Fig. 5.5(b) that a small amount of volume scattering can be observed coming from the sand. This will be used to compensate the measured volume scattering in section 5.4.2.
3. The ratio I_1/I_o yields the bottom loss, defined as $BL = -20 \log(|R_{01}|)$, where R_{01} is the plane wave reflection coefficient in section 4.2. For $c_{T1}/c_{L1} \ll 1$, $R_{01} \approx (c_{L1}\rho_1 - c_{L0}\rho_0) / (c_{L1}\rho_1 + c_{L0}\rho_0)$ where c_{L0} and ρ_0 are the (known) speed of sound and the density of fresh water. Then, the density ρ_1 of the water-saturated sand can be estimated. Note that since the sand is not a perfectly flat surface, R_{01} was actually estimated as an average over 70 realizations, where each realization consisted of shifting the source/receiver to slightly different positions over the sand.
4. The final step is to measure the frequency-dependent attenuation of the sand, α_{L1} , which is related to I_2 and I_o as:

$$I_2 = (1 - |R_{01}|^2)^2 R_{12} e^{-4\alpha_{L1} z_d} I_o, \quad (5.2)$$

where R_{12} is the reflection coefficient at the bottom of the water tank.

5. Figure 5.6 shows a plot of $\ln(I_2/I_o)(1/(4z_d))$, where the frequency-dependent attenuation was estimated by a linear fit as

$$\alpha_L \approx 0.016f_{kHz} + 4 \quad (\text{Np/m}). \quad (5.3)$$

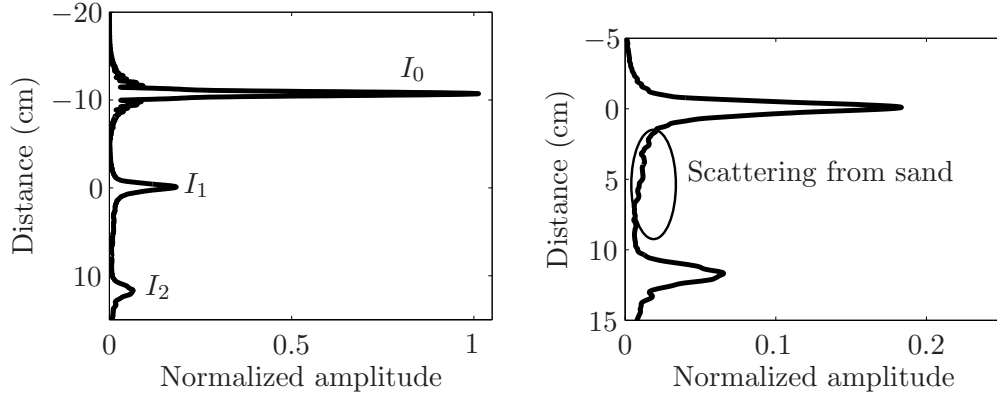


Figure 5.5: (a) Scattering of a broadband pulse from the sand slab, showing the incident pulse (I_o) and energy reflected from the water-sand interface (I_1) and from the bottom of the tank (I_2). The graph shows the envelope of the scattered pulse after performing pulse compression. The vertical axis is given in units of distance, with the zero lined up to I_1 ; (b) Zoom-in of (a), where scattering from the sand can be observed.

The inversion of geoacoustic parameters for the sand substrate was carried out to increase the accuracy of the input values provided to the RT model in the next section. All the estimated values are of similar order to the ones found in the literature [8] for sediments of similar grain size², and small variations

²See for example the geoacoustic properties of sites MonPT and SG98-10 in table 5.1 of Jackson et al. [8], measured at a frequency of 400 kHz.

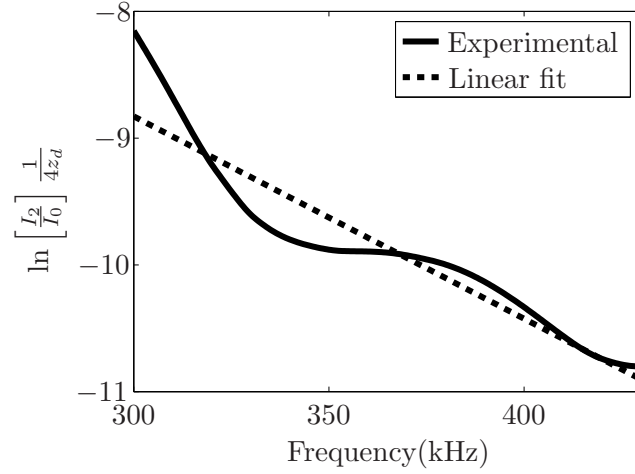


Figure 5.6: Estimation of the frequency-dependent attenuation of the sand slab as $\ln[I_2/I_0](1/(4z_d))$, showing the measured value (solid line) and the linear fit (dotted line) in (5.3).

in the background sound speed or the density does not have strong impact on the estimated volume scattering, as long as the product $c_{L1}\rho_1$ which controls the reflection coefficient in the sediment-water interface is kept constant to the measured value. The results are also sensitive to the background attenuation, because this parameter controls the amount of power incident at the layer of scatterers, as well as the strength of multiple scattering effects. The performed measurements provide an estimate of the attenuation in the full frequency band of interest. This estimate is a more appropriate choice than using values taken from tables based on grain size, because the direct measurement also accounts for the (potential) effect of trapped air bubbles.

5.4.2 Measurements of volume scattering

Once the acoustic parameters of the sediment were determined, the scatterers were positioned within the sand. To this end, aluminum spheres with radius $a = 2.4 \text{ mm}$ were deposited on top of the sand layer as shown in Fig.5.7(a), and then each scatterer was pushed into the sediment to end up with the configuration shown in Fig.5.7(b). The scatterers are located at depths between 1 cm and 7 cm in the slab. The purpose of leaving a gap of 1 cm is to separate the volume scattering from the return of the sediment interface.

The amplitude of the energy scattered by the aluminum spheres can be seen to the left of Fig. 5.7(b), with a maximum at around 3 cm depth and significantly higher than the volume scattering from the sand background (measured prior to the deposition of aluminum scatterers).

With the spheres in the sediment, volume scattering at normal incidence ($\theta_i = 0^\circ$) was measured by taking 70 realizations and processing the data as described in section 5.2 to compute the average scattering cross section $\Upsilon_{av}(f, \theta_i)$, which is shown in Fig.5.8(a). Since the processing requires the spectral normalization in (5.1) as well as compensation for spherical spreading by the factor C , it is convenient to begin the experiment by measuring the energy reflected from a rigid reflector, which is known to yield a flat response of 0 dB at all frequencies. To this end, an aluminum plate (15x15 cm) was temporary placed on top of

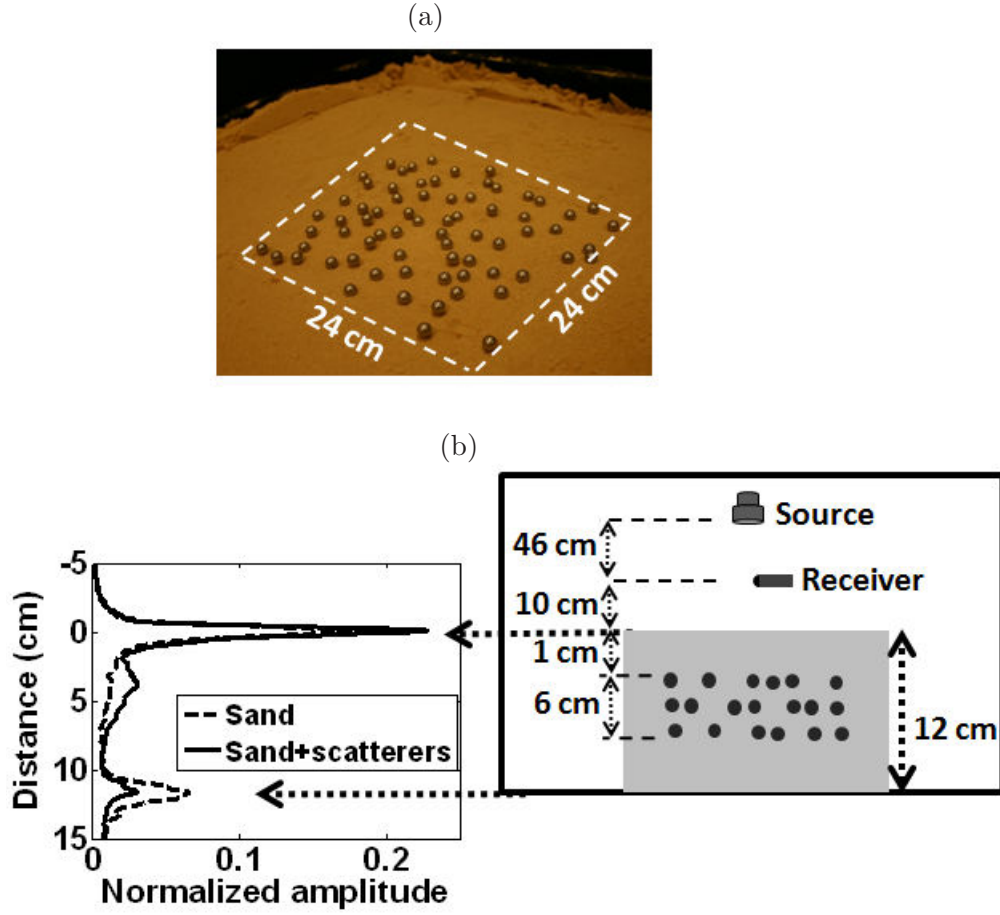


Figure 5.7: (a) Aluminum spheres of radius $a = 2.4 \text{ mm}$ deposited on top of the sand layer. The spheres were pushed within the sand to obtain the configuration shown in (b); (b) Setup for experiment 2, with scatterers located at depths between 1 cm to 7 cm. The amplitude of the scattered energy can be seen to the left, and it exhibits a maximum around 3 cm depth.

the sediment, and the measured reflected energy is shown in Fig.5.8(a). This preliminary measurement confirms that no artifacts are being introduced by doing the spectral normalization, and also verifies the correct value of the compensation factor C . Figure 5.8(a) also shows the energy reflected from the sediment-water interface (average over 70 realizations). The average over realizations reduces the

effect of the rough surface, and it yields a frequency response that resembles the scattering from a flat surface with a reflection coefficient $R = 0.32$, in agreement with the parameters in Table 5.1.

Figure 5.8(a) also shows the simulated scattering cross section according to (3.72), and it is evident that there is an offset between the RT simulation and the experimental measurements. To explain this effect, it is observed that the sand background also contributes to scattering, and therefore it must be subtracted from the total cross section. This compensated cross section $\Upsilon_{comp}(f, \theta_i = 0)$ was computed as:

$$\Upsilon_{comp}(f, \theta_i) = \frac{1}{N} \sum_{n=1}^{70} \Upsilon_n(f, \theta_i = 0) - \frac{1}{N} \sum_{n=1}^{70} \Upsilon_n^{sand}(f, \theta_i = 0); \quad (5.4)$$

where $\Upsilon_n^{sand}(f, \theta_i = 0)$ is the n^{th} realization of the scattering cross section due only to the sand, measured prior to the positioning of the aluminum spheres in the sediment. $\Upsilon_{comp}(f, \theta_i = 0)$ is shown in Figure 5.8(b), and it provides a better match with the RT model.

The experimental results in Fig. 5.8 show that the RT model performs well when modeling complex media in which background attenuation and reflective boundaries are involved. In this example, the average over realizations was required not only to obtain the expected value of the cross section (which is the aim of radiative transfer), but also to mitigate the effect of the rough water-sediment

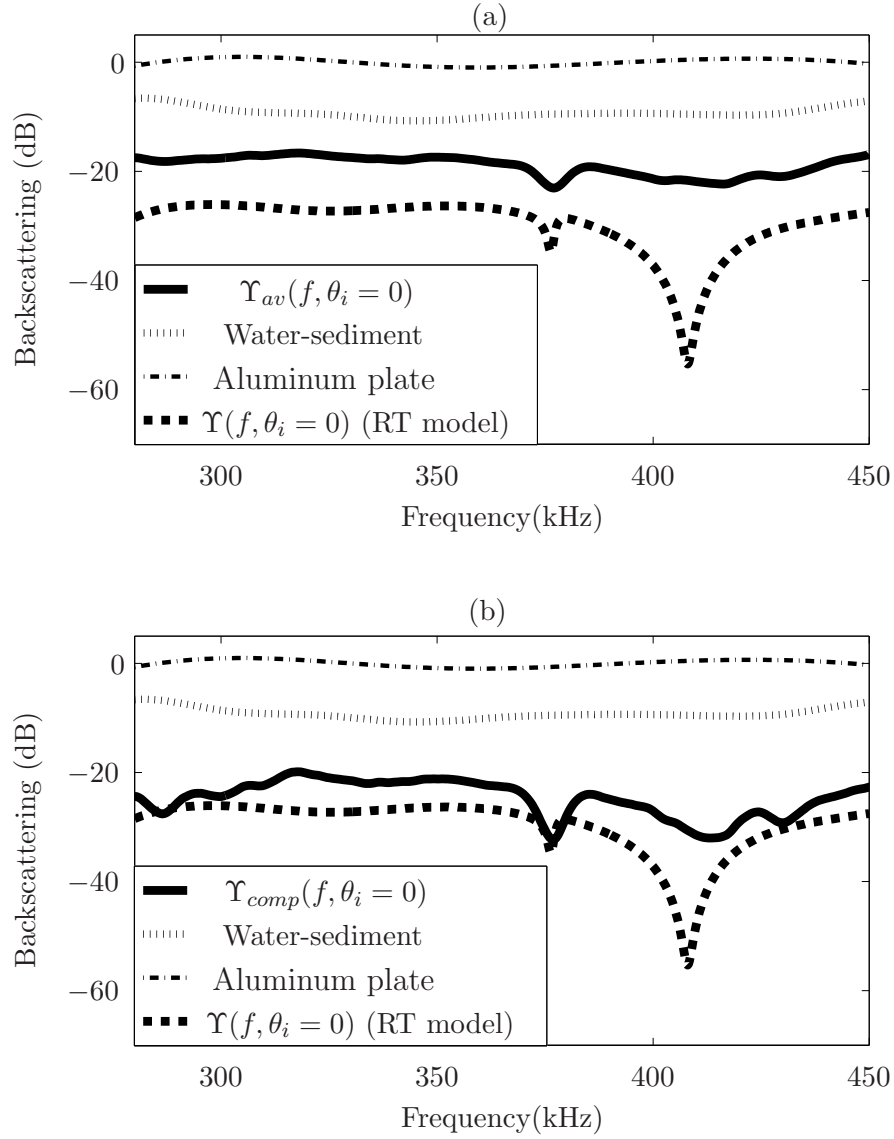


Figure 5.8: (a) Volume scattering from the aluminum spheres and the sand compared to the RT model. The offset between the experimental data and the model is due to scattering from the sand itself. This figure also shows scattering from a rigid aluminum reflector, as well as the energy reflected by the sediment-water interface; (b) Same as (a), but the volume scattering is compensated as indicated in (5.4).

interface. The experimental measurement captured one of the sharp resonances predicted by the model (around 376 kHz) but missed the strongest resonance at 407 kHz. The explanation for this could be due to the sand acting as a dense scattering medium and introducing frequency-dependent effects not accounted for in the RT model, which assumes homogeneous media. Scattering due to discrete grains of sand has been reported in the literature [4]. A more certain explanation for the observed phenomenon would require repeating the experiment with centrifuged and finer sand or clay, to minimize the presence of air bubbles and the volume scattering from the background media.

5.5 Experiment 3: Glass scatterers in resin background

A more challenging scenario to test the RT model was achieved by using a slab with smaller scatterers in the Mie regime and at a higher fractional volume. In this experiment, a lossy polyurethane slab (provided by the Laboratory of Mechanics and Acoustics, CNRS/LMA, France) with embedded glass beads was utilized. The background material has an acoustic impedance close to fresh water, with a lower compressional sound speed and a higher density. This results in the absence of a critical angle and favors energy penetration at all angles of incidence. The slab does not support shear propagation, which is automatically accounted for in the RT model by setting the shear sound speed to a small value

of 1 m/s. The scattering material was manufactured to minimize the presence of air bubbles, as corroborated by X-ray studies [38].

The slab contains a uniform distribution of glass beads of 1 mm diameter, with a fractional volume of 10 %. This model has been utilized in the past for similar measurements [38] at a frequency of 500 kHz, and its acoustic properties have been well characterized and are summarized in table 5.1.

In this experiment, $L = 25$ cm, $R = 15$ cm (see Fig. 3.12(b)), and the angle of incidence θ_i was varied from 0° to 75° in 5° steps. The angle-dependent scattering from the slab was measured as follows: at each angle θ_i , $N = 30$ realizations were taken by laterally shifting the slab in the $\pm x$ direction.

Fig. 5.9(a) shows pulse-compressed realizations corresponding to two scattering angles. At normal incidence ($\theta = 0^\circ$), the scattered energy includes both the specular reflection from the water-slab interface and the contribution from the scatterers, while at $\theta = 10^\circ$ the return is due only to volume scattering. Figure 5.9(b) shows the corresponding $\Upsilon_{av}(f, \theta)$, with thinner solid lines that indicate ± 1 standard deviation. As in experiment 2 (aluminum scatterers in sand background), the scattering from a reference plate is shown to have a flat frequency response around 0 dB, which rules out the insertion of artifacts during data processing.

The large standard deviation and frequency dependent variability of the mean

observed in Fig. 5.9(b) required further analysis. It is roughly ± 5 dB and it was present at all scattering angles. It is important to note that due to the small size of the slab, measurements at shallow angles were affected by edge effects of the slab as well as by scattering from the supporting structure depicted in Fig. 5.1(a), located within the tank and used to hold the slab in position. To estimate the effect of this structure, measurements were taken without the slab at all angles, and this revealed that significant contamination of the data occurred for $\theta > 40^\circ$. This was evident from the data, which presented increasing standard deviations at larger angles of incidence.

For the case of $\theta < 40^\circ$, the standard deviation of around 5 dB has also been observed in experimental and simulated data at 500 *kHz*. At this frequency, scattering from the same material was studied by Canepa et al [38] using a time domain model that generates realizations of the ensemble of scatterers at each incident angle, and the simulated data exhibits similar behavior. This suggests that the variability observed in the experimental data is caused by frequency dependent characteristics of the ensemble of glass beads rather than experimental uncertainty. This also indicates that $\Upsilon_{av}(f, \theta_i)$ can be smoothed by incorporating more realizations.

Fig. 5.10 shows volume scattering measured at 300 *kHz* and 400 *kHz* (solid

lines). The mean value of the backscattered data, $\Upsilon_{av}(f, \theta)$, exhibits angle-dependent variations and behavior similar to the measurements at 500 kHz [38], and due to the large variability noted before, it is not possible to make a clear distinction between the scattering at different frequencies. Fig. 5.10 also shows dashed lines with simulations at 300, 400 and 500 kHz using the steady state RT model. At 500 kHz, previous work has concluded that $\alpha_L = 80$ Np/m is a reasonable value for the attenuation of the resin matrix. Using this value in the RT model results in scattering levels comparable to those previously reported [38]. The background attenuation at lower frequencies was not measured for this material, and it was used as a free parameter in the RT simulations since direct measurements are not possible due to the thickness of the slab. At 300 kHz and 400 kHz, attenuation coefficients of 50 Np/m and 65 Np/m respectively yield a good fit of the model to the mean value of the experimental data.

An alternative for estimation of the background attenuation is by running time domain simulations of backscattering [38] with attenuation as a parameter, with the goal of matching the shape of the scattered waveform to experimental measurements. The possibility of using this technique, as well as the simulation of short excitation pulses motivates the ongoing study of the transient RT equation.

5.6 Conclusion

Measurements of the scattering cross section from random media were conducted in a tank setup in the geometrical optic and Mie regimes. The relevant acoustic parameters of the laboratory models were either obtained from the literature or measured at the NEAR-Lab. These parameters summarized in table 5.1 provide the input to the RT model, which was able to match the experimental scattering cross sections. The level of complexity of the random media was gradually increased, from a slab with no reflective boundaries and no background attenuation (experiment 1), to a slab with reflective boundaries, frequency dependent background attenuation and small scatterers (experiment 3). It has been shown that the proposed RT model is able to support:

1. Random media with scatterers in the Mie and geometrical optic regime.
2. Reflective elastic boundary conditions.
3. Different concentrations of scatterers, with fractional volumes ranging from 0.9% to 10% ³.
4. The effect of frequency-dependent background attenuation.

³Fractional volumes of 10% normally require the use of the Dense Media Radiative Transfer (DMRT) formulation to account for strong multiple scattering. Nevertheless, in the case of experiment 3 the background attenuation has the effect of reducing multiple scattering, which allowed application of the model without modification.

To end this section, it is worth to provide an idea on how the experimental models used in these experiments would scale to the the lower frequencies normally used in field experiments performed in the ocean. Table 5.2 shows this relation for experiments 2 and 3, providing the equivalent size of the scatterers at frequencies of $f = 40 \text{ kHz}$ and $f = 12 \text{ kHz}$.

Table 5.2: Examples of scaling of the performed tank experiments to field experiments. The center frequency of the tank experiments is 350 kHz, corresponding to a wavelength of 4.3 mm.

	Experiment 2 (Sand+aluminum)	Experiment 3 (Resin+glass)
Scatterer radius (cm)	0.24	0.05
Scatterer radius (wavelengths)	0.56	0.12
Scaled frequency (kHz)	40	12
Scaled scatterer (cm)	2.1	1.46

The typical frequency range used in field experiments for chirp surveys like the one shown in Fig. 1.2 (a) is between 6 kHz and 12 kHz and similarly, other field experiments have been carried out at frequencies of 40 kHz [39]. At these frequencies, the size of the scaled scatterers in Table 5.2 is of similar order to the size of shells and rocks normally found in the seabed sediment[1, 2, 3, 4], as observed from the core sample in Fig. 1.2 (b). Therefore, except for the background attenuation (which could not be scaled), the tank experiments presented here correspond to realistic conditions of field experiments.

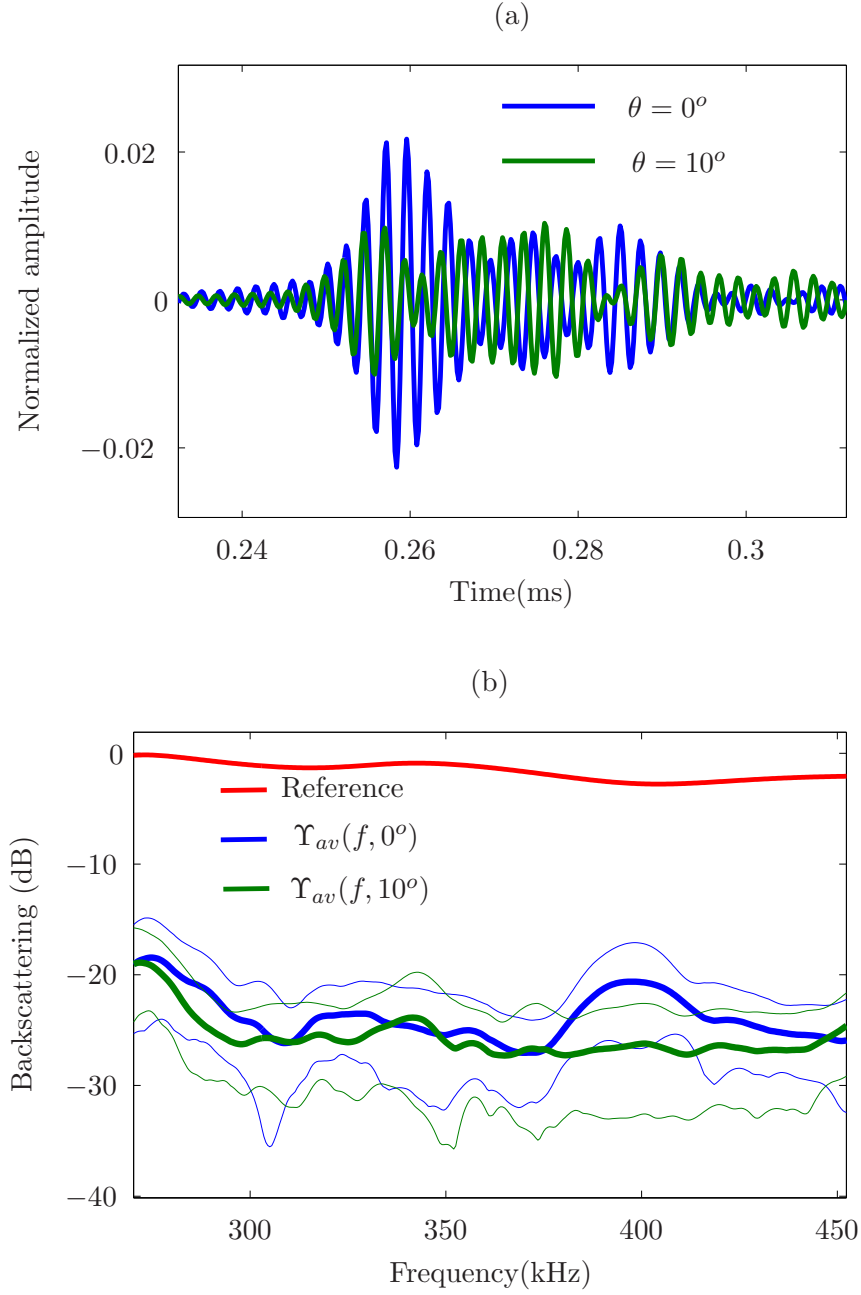


Figure 5.9: (a) Example of two realizations of the backscattered signal after pulse compression, for $\theta = 0^\circ$ and $\theta = 10^\circ$. The waveforms are normalized to the peak value of the direct blast. (b) $\Upsilon_{av}(f, \theta_i)$ for the two incident angles in (a), with thin solid lines indicating ± 1 standard deviation around the mean of 30 realizations.

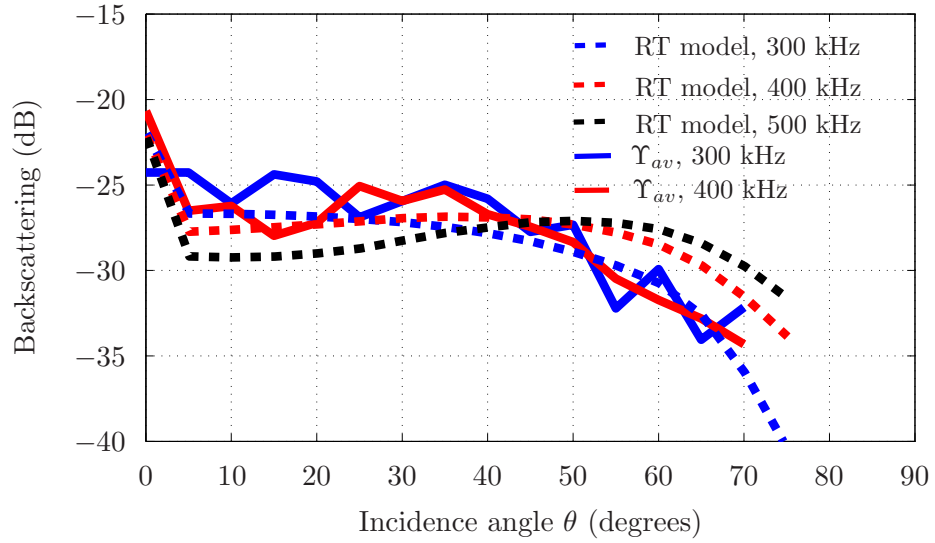


Figure 5.10: Comparison of the measured backscattering, $\Upsilon_{av}(f, \theta)$ (solid lines), with computations from the RT model at 300 kHz and 400 kHz (dashed lines). Computation of backscattering at 500 kHz is also shown (black, dashed line) for comparison to previous experimental work using this slab (see text for details).

Chapter 6

Comparison of the model to field experimental data

The ultimate goal of this research is the application of the RT model to understand acoustic propagation in real seabed sediments. The validation experiments presented in section 5 provided insight into the capabilities of the RT model to accommodate a wide range of experimental conditions, and the task now is to extend this analysis to field experimental data. An example of volume scattering due to discrete scatterers in the seabed can be found in environments with strong biological activity, in which methane gas is trapped in the sediment. Fleischer et al [40] have identified over 100 shallow water sites containing gas-saturated sediments worldwide, and they have discussed the importance of conducting systematic research on the subject.

In this section, the RT formulation is used to model scattering from a sediment layer containing gas bubbles. The acoustic experiment was conducted in 1993 [39], and sediment (core) samples were extracted to determine gas content and structure of the sediment. The experiment setup is described in the next section,

followed by application of the RT model.

6.1 The Eckernförde Bay experiment

In 1993 a series of experiments was conducted to measure acoustic scattering from a silty clay area in the Eckernförde Bay, Germany [39]. Other research in this area included the extraction of core samples of the sediment, which determined the presence of gas bubbles, and these discrete scatterers were responsible for most of the volume scattering measured in this region. The experiment can be summarized as follows: a 5 m tall tower was placed on top of the sediment, as shown in Fig. 6.1(a). The tower supported a transmitter and receivers, and narrow band pulses in the frequency of $f = 40 \text{ kHz}$ were transmitted to be incident upon the sediment. The horizontal and vertical beam widths of the transmitter are 5° and $\approx 14^\circ$, respectively, and the center of the main lobe was pointed toward the sand at a depression angle of 12.5° . Due to the spherical pattern of the transmitted waveform shown in Fig. 6.1(b), the energy hits the sediment at angles ranging from 20° (closer to the base of the tower) to 5° . The scattered echo from the sediment was recorded in two hydrophones on top of the tower. By using two hydrophones, the technique known as differential phase [39] was applied to invert for the depth of the layer containing gas bubbles and it was found to be $z_{d1} = 1 \text{ m}$. The time of flight of the transmitted pulse was utilized

to separate the amount of scattering from different patches of ground, each one associated with a corresponding incidence angle. In total, the illuminated area was divided into 15 patches.

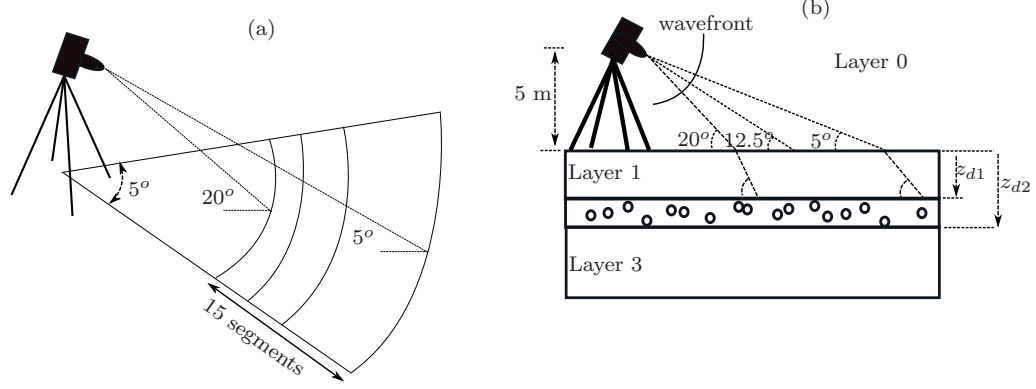


Figure 6.1: Experimental setup for the Eckernförde Bay experiment: (a) 3D view of the angle of incidence of the transmitted spherical wave as a function of range; (b) Side view of the experiment and the structure of the seabed. It was found experimentally that $z_{d1} \approx 1 \text{ m}$, while the thickness of the layer, $z_d = z_{d2} - z_{d1}$ is used as a free parameter in the next section.

Table 6.1 summarizes the known parameters of the sediment for this experiment, which are used as inputs to the RT model discussed in section 3.2. Other quantities such as bubble size distribution, fractional volume and layer thickness are used as free parameters in the next section, with high/low bounds obtained from the core samples.

Table 6.1: Acoustic properties of the sediment at the Eckerfoerde Bay.

Variable	Value (from [39, 9])
ρ_0	1000 kg/m ³
c_{L0}	1448 m/s
$\rho_1=\rho_2$	1100 kg/m ³
$c_{L1}=c_{L2}$	1425 m/s
$c_{T1}=c_{T2}$	9 m/s
$\alpha_{L1}=\alpha_{L2}$	2.4 dB/m

6.2 RT model for thin and thick layers of randomly distributed scatterers

Referring to Fig. 6.1(b), scattering must be predicted from a four-layer model, where the interface between layers 0 and 1 is reflective due to the water-sediment contrast, layer 2 contains the scatterers and layer 3 is an infinite halfspace. Since $\eta = 0$ for layer 1, the diffuse intensity is zero and the RT model predicts a decrease in intensity due to the background attenuation α_{L1} given by:

$$I_{ri_1}^{L_1\downarrow}(z, \mu, \phi) = K_{L0} \hat{T}_{01}^{LL} \exp \left[-\frac{\alpha_{L1} z}{\cos \theta} \right] \delta(\theta - \theta_1^{L_1}) \delta(\phi - \phi_i), \quad (6.1)$$

where $\theta_1^{L_1} = \sin^{-1}(\theta_i c_{L1}/c_{L0})$ is the angle refracted at the water-sediment interface, \hat{T}_{01}^{LL} is the transmission coefficient according to table 4.1, and K_{L0} is the power density of the incident wave. $I_{ri_1}^{L_1\downarrow}(z, \mu, \phi)$ is the excitation source in layer 2, for which the RT model is applied again to obtain the backscattered diffuse intensity.

The RT model can be run as shown in the previous sections, but an approximation can be used to compare its results to the model presented by Tang et al [39]. Assuming that the scattering medium has a small fractional volume (or more accurately, that multiple scattering effects can be ignored) then the upward single scattering solution for the RT model is written as [41]:

$$I_d(z, \mu, \phi) = \frac{\mu_1^{L_1}}{\mu_1^{L_1} - \mu} \frac{P(\theta, \phi; \theta_1^{L_1}, \phi_i)}{4\pi\sigma_L} K_{L0} \hat{T}_{01}^{LL} \exp\left[-\frac{\alpha_{L1} z_{d1}}{\mu_1^{L_1}}\right] \left[\exp\left[\frac{-\eta\sigma_L(z - z_{d1})}{\mu_1^{L_1}}\right] - \exp\left[\frac{-\eta\sigma_L(z_{d2} - z_{d1})}{\mu_1^{L_1}} + \frac{\eta\sigma_L(z_{d2} - z)}{\mu}\right] \right]. \quad (6.2)$$

If it is also known that the layer containing scatterers is thin so $\eta\sigma_L(z_{d2} - z_{d1}) \ll 1$. Then, at $z = z_{d1}$ and $\theta = \pi - \theta_1^{L_1}$, (6.2) reduces to:

$$I_d(z = z_{d1}, \mu, \phi) = \frac{1}{\mu_1^{L_1}} \frac{P(\pi - \theta_1^{L_1}, \phi; \theta_1^{L_1}, \phi_i)}{4\pi} K_{L0} \hat{T}_{01}^{LL} \exp\left[-\frac{\alpha_{L1} z_{d1}}{\mu_1^{L_1}}\right] \eta(z_{d2} - z_{d1}). \quad (6.3)$$

The power at the receiver can be written as

$$P_r = \int_{\Delta\Omega} I_d(z = z_{d1}, \mu, \phi) \hat{T}_{01}^{LL} \left[-\frac{\alpha_{L1} z_{d1}}{\mu_1^{L_1}}\right] \mu_1^{L_1} d\Omega \frac{P(\pi - \theta_1^{L_1}, \phi; \theta_1^{L_1}, \phi_i)}{4\pi} K_{L0} \left[\hat{T}_{01}^{LL} \exp\left[-\frac{\alpha_{L1} z_{d1}}{\mu_1^{L_1}}\right]\right]^2 \eta(z_{d2} - z_{d1}) \frac{dA}{R^2}, \quad (6.4)$$

where dA is the patch illuminated by the incident acoustic pulse, $\Delta\Omega$ is the angle of observation of the receiver, and R is the distance from the center of the patch

to the receiver, which accounts for the spherical spreading. Note that the product $\eta(z_{d2} - z_{d1})dA$ is the number of scatterers within the illuminated volume.

The backscattering strength can be obtained from 6.4 as

$$\begin{aligned} \Upsilon(\theta_i) &= R^2 \frac{P_r}{K_{L0}} \\ &= \eta(z_{d2} - z_{d1})dA \frac{P(\pi - \theta_1^{L_1}, \phi; \theta_1^{L_1}, \phi_i)}{4\pi} \left[\hat{T}_{01}^{LL} \exp \left[-\frac{\alpha_{L1} z_{d1}}{\mu_1^{L_1}} \right] \right]^2, \end{aligned} \quad (6.5)$$

which can be interpreted as the incoherent summation of the power scattered by each individual bubble, adjusted by the two-way sediment attenuation and by the transmission coefficient of the sand-water sediment. This model was used by Tang et al. [39] to explain the volume scattering measured at the Eckernfoerde Bay, under the assumption of a thin layer of scatterers. Chu et al [9] concluded that the bubbles in this sediment have equivalent spherical radius between 0.5 mm and 15 mm, and the equivalent surface density of scatterers was found to be $\eta z_d \approx 9000$ scatterers/ m^2 .

Core samples of the sediment from this area [42] have shown that the gas content in this sediment is distributed in a layer of thickness $z_d < 0.2$ m. From the work by Tang et al [39], it was concluded that the best fit between their model and the experimental data was achieved when the constraint

$$10 \log_{10} [\eta(z_{d2} - z_{d1})P(\pi - \theta_1^{L_1}, \phi; \theta_1^{L_1}, \phi_i)/4\pi] = -10.8 \text{ dB}; \quad (6.6)$$

is met.

In order to provide a numerical example of the application of the RT model, it is assumed that all the bubbles are the same size¹. Figure 6.2 shows the scattering strength as a function of bubble radius, and it was found that the values $a = 3.5 \text{ mm}$ and $\frac{P(\pi-\theta_1^{L1}, \phi; \theta_1^{L1}, \phi_i)}{4\pi} = 6e^{-6} \text{ m}^2 \text{ sr}^{-1}$ meet the constraint in (6.6).

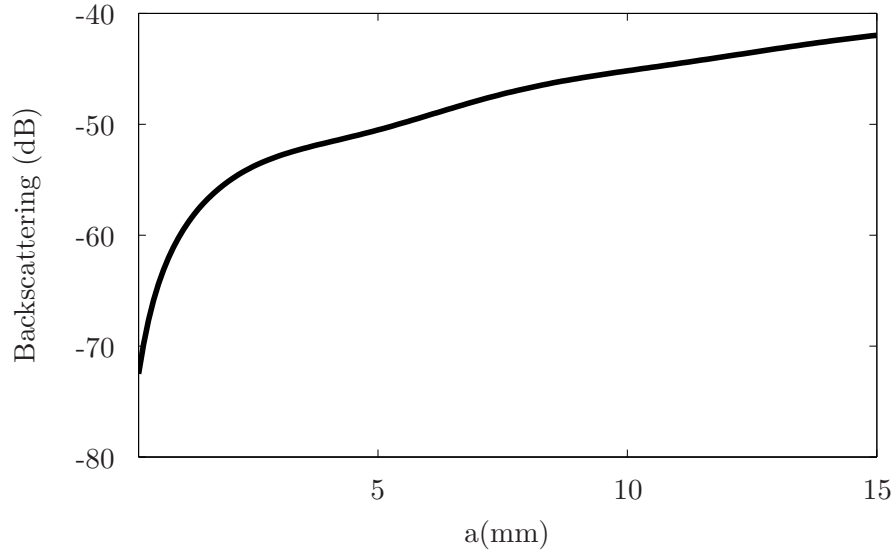


Figure 6.2: Backscattering strength vs bubble radius, for a sand background with $c_{L1} = 1468 \text{ m/s}$ and $\rho_1 = 1100 \text{ m/s}$. The average size of the scatterers is obtained from this figure by choosing a value in agreement with the constraint in (6.6).

With these values, the density of scatterers and the thickness of the layer are found to be $\eta = 112500 \text{ scatterers/m}^3$ and $(z_{d2} - z_{d1}) = 0.08 \text{ m}$, respectively, corresponding to a fractional volume of $FV = 1.2\%$. This parameter is within

¹Note that this assumption is not imposed by the RT model, but rather by the information available in the literature about the sediment. If a better estimate of the size distribution of the bubbles becomes available, it can be incorporated in the RT model.

the range of concentrations measured from core samples [42].

Using the previous parameters as inputs to the RT model, simulations were run for comparison to the experimental data and to the original single scattering model proposed by Tang et al[39], and the results are summarized in Fig. 6.3. Due to the low fractional volume, the RT model converged to the single scattering solution in (6.5), and therefore it closely match the original model. Nevertheless, the RT model is also effective in more restrictive cases when the layer containing scatterers is too thick to be represented as an equivalent surface density of scatterers. This is also illustrated in Fig. 6.3 for $z_d = 0.4 \text{ m}$ and $z_d = 0.8 \text{ m}$, in which all the other parameters were kept constant. As the thickness of the layer increases, the amount of backscattered energy also increases until a saturation is reached. This saturation occurs as the incident energy coming from the water column is attenuated by the background as well as by the scatterers closer to the sediment-water interface, and therefore the contribution from scatterers at the bottom of the layer is reduced.

6.3 Conclusion

In this section, simulations using the proposed RT model have been compared to field experimental data from a region with a thin layer containing random distributions of gas bubbles. The exact value of the fractional volume, the average

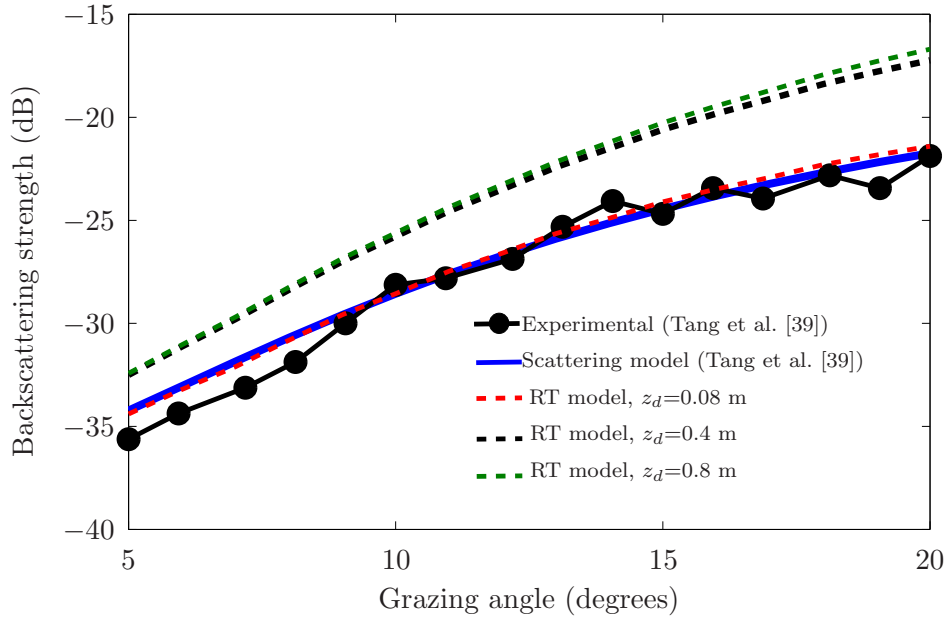


Figure 6.3: Comparison of the RT model to the experimental data collected at the Eckernförde Bay and to a single scattering model proposed in the literature. The RT model was run with $a = 3.5 \text{ mm}$, $\eta = 112500 \text{ scatterers/m}^3$, $FV = 1.2\%$, and the sediment parameters in Table 6.1. The thickness $z_d = 0.08 \text{ m}$ yielded the best match to the experimental data. RT simulations with $z_d = 0.4 \text{ m}$ and $z_d = 0.8 \text{ m}$ are also shown to illustrate the effect of saturation.

size of scatterers and the thickness of the layer were not available in the literature.

For that reason, approximate values that are in agreement with measurements from core samples extracted from the same geographic area were found by exploration of the single scattering solution as well as the scattering strength of a single bubble. It was shown that for a thin layer or small fractional volume, the RT model converges to the single scattering solution that has been proposed in the past by other authors, in which an equivalent surface distribution of scatterers was assumed.

For more restrictive conditions in which a volume distribution of scatterers must be utilized due to thicker layers, the RT model can be directly applied without the need of adjustments. For the simulations with $z_d = 40$ cm and $z_d = 80$ cm, the RT model is shown to converge to a meaningful solution that resembles the skin depth effect of electromagnetic scattering, as well as meeting other physical requirements such as conservation of the normal power flux. The RT model presented in this work is a first order multiple scattering formulation [21], which has advantage over single scattering in the sense that it accounts for scattering and attenuation of the acoustic energy as it travels to and from each scatterer, and therefore it includes some of the multiple scattering effects.

Chapter 7

Time domain solutions obtained by the radiative transfer method

The time-domain solution of the RT equation presented in section 3.3 is the most recent research effort in transport theory in the electromagnetics and the acoustics community. The appeal of the transient solution is that it allows representation of the scattered intensity as a time series, which might carry important information about the micro structure features of the media such as anisotropy or extinction coefficient. The technique also provides a way to simulate more realistic excitation signals, such as the broadband chirp pulses typically used in underwater acoustics. The goal of this chapter is to portray the use of the transient RT equation in a realistic environment. As a reference, an analytical first-order approximation for the scattered intensity is introduced first, and then compared to the solution of the transient RT equation.

7.1 Time domain dependency of the scattered intensity: an analytical model

Without any knowledge of transport theory, an approximate solution can be found for the scattered intensity that results when an energy pulse is incident upon a slab containing random scatterers [21]. Figure 7.1(a) shows the general case of a co-located source/receiver system that transmits a pulse and records the backscattered energy from an arbitrary slab.

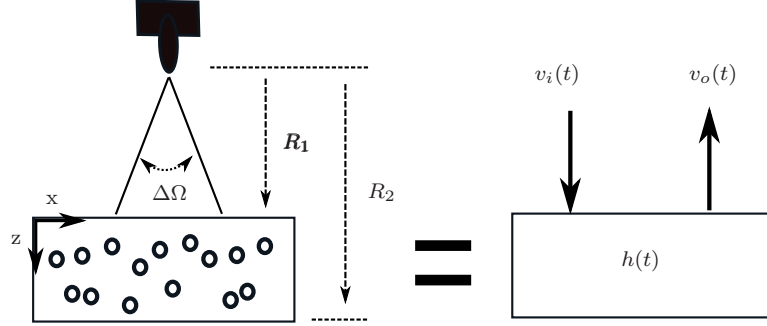


Figure 7.1: General geometry of a monostatic active system that transmits a finite pulse $v_i(t)$ and receive the acoustic echo $v_o(t)$. The scattering media can be represented as a linear system with an impulse response $h(t)$, and an analytical approximate solution can be obtained.

The transmitted and received signals can be represented as

$$\begin{aligned} v_i(t) &= \text{Re} [u_i(t)e^{-j\omega_o t}] ; \\ v_o(t) &= \text{Re} [u_o(t)e^{-j\omega_o t}] ; \end{aligned} \tag{7.1}$$

where $\omega_o = 2\pi f_o$ and $u_i(t)$ are the carrier frequency and envelope of the transmitted pulse, while $u_o(t)$ is the envelope of the received field.

From the properties of linear systems and without any approximation so far, it can be shown[21] that $u_o(t)$ is given by

$$u_o(t) = \int_{-\infty}^{\infty} U_i(\omega) H(\omega + \omega_o) e^{-j\omega t} d\omega \quad (7.2)$$

where $H(\omega)$ is the Fourier transform of $h(t)$. After removing high frequency oscillations, the scattered intensity is $I(t) = \frac{1}{2} \text{Re} [< u_o(t) u_o^*(t) >]$ and several approximations are used to find a solution. Ishimaru[21] obtains the scattered intensity when the following conditions are assumed:

1. The excitation signal consists of a short pulse of the form

$$v_i(t) = \text{Re} \left[\sqrt{\frac{F_{Lo}}{T_o}} e^{-i\omega_o t} \right], \quad 0 \leq t \leq T_o \ll (R_2 - R_1)/c_L. \quad (7.3)$$

2. The transmitter has a narrow radiation pattern where $\Delta\Omega$ is small.
3. Single scattering is dominant, so the transfer function in the frequency domain can be approximated by

$$H(\omega) \approx f(\theta_i, \pi - \theta_i, \omega) \frac{e^{i2k_L(R_1+z)}}{(R_1+z)^2} e^{-\eta\sigma_L z}, \quad (7.4)$$

where $f(\theta_i, \theta_o, \omega)$ was defined in (2.4) as the amplitude of the wave scattered by a single scatterer, and ω has been included as an argument to emphasize its dependency on the carrier frequency.

When $R_1 \gg R_2 - R_1$, the scattered intensity can be written as

$$I(t) \approx \frac{\eta |f(\theta_i, \pi - \theta_i, \omega_o)|^2}{R_1^2} \frac{c_{L1}}{2} e^{-\eta \sigma_L c_{L1} t}, \quad (7.5)$$

$$\frac{2R_1}{c_{L1}} + T_o \leq t \leq \frac{2R_2}{c_{L1}}.$$

The backscattered intensity in (7.5) has been obtained from arguments based on the wave equation, and it will be compared to the transient RT equation.

7.2 Impulse response of a finite layer obtained from the transient RT equation

As a numerical example of the solution of the transient RT equation, the parameters in table 7.1 are used to compute the backscattered intensity. In this example, the scatterers are air bubbles of radius $a = 2.1 \text{ mm}$ with longitudinal scattering cross section of $\kappa_L = 5.6e^{-5} \text{ m}^2$.

The transient RT equation in (3.57) was computed for a maximum outer frequency of $\Theta_{max} = 22000 \text{ rad/s}$ with a step size of 300 rad/s , and the results are shown in Fig. 7.2. The choice of outer frequency parameters have an impact on the oscillations observed in the RT solutions, and they tend to disappear as

Table 7.1: Acoustic properties of environment in Fig. 7.1 used to obtain solutions to the Transient RT equation.

Variable	Value
$\rho_0 = \rho_1 = \rho_2$	1000 kg/m ³
$c_{L0} = c_{L1} = c_{L2}$	1448 m/s
a	2.1 mm
FV	0.034 %
η	8636 scatterers/m ³
$R_2 - R_1$	2 m
F_{L0}	1 watt/m ²

Θ_{max} increases and the step size decreases. The single scattering RT solution was obtained by setting the double integral in (3.57) to zero, and it matches with the analytical solution in (7.5). The sharp transition at $t = 2.73$ ms is caused by the thickness of the layer, and corresponds to the two-way travel time of the energy within the slab. The full solution includes all the terms, and the heavier tail and smoother transition is caused by the contribution of multiple scattering events.

The transient RT equation developed in section 3.3 corresponds to short excitations similar to the pulse in (7.3), which becomes an impulse when $T_o \rightarrow 0$, and the solution of the RT equation gives the impulse response of the random medium. Field experiments with this kind of excitation are performed in seismic exploration with explosive charges[43], and information about the sediment can be extracted by analysis of the rate of decay of the scattered intensity[44]. In acoustic exploration of the seabed, chirp sonars with broadband excitations are utilized to obtain profiles like the one shown in Fig. 1.2(a). In these cases, a

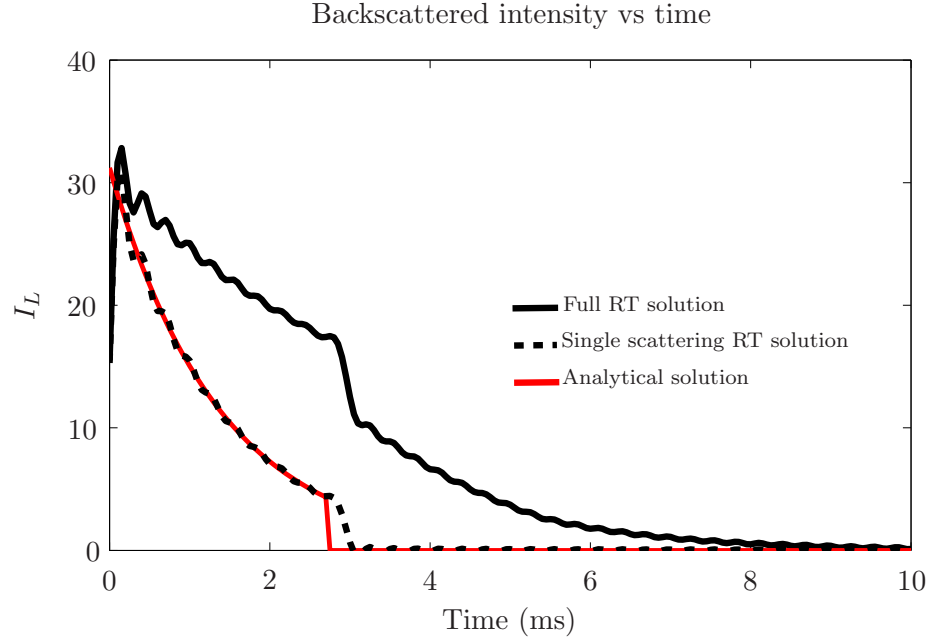


Figure 7.2: Solution of the transient RT equation (full and single scattering approximation) and comparison to the analytical solution in (7.5). The full solution is in agreement with energy conservation and therefore it represents more accurately the impulse response of the random media.

forward model of the scattered intensity is obtained by convolution of the excitation envelope with the impulse response of the media[15], and it can be utilized with methods of sediment classification based on the shape of the envelope of the intensity[45, 46] or more sophisticated methods like the so called *similarity index*[47].

A quantitative comparison between the single scattering and full solutions can be accomplished by verifying energy relations. The power flux definitions presented in section 3.4 also apply to the transient solutions, but notice that the new units of the intensity are $watt\ s^{-1}m^{-2}$ and therefore, an integral on the time

axis must also be carried out. Figure 7.3 shows the coherent and diffuse power fluxes for the single scattering and the full solution at incidence angles from 0° to 80° . In lossless media, the conservation of energy can be verified by adding the scattered normal components of the power flux leaving the layer at $z = 0$ m and $z = z_d$ m, and comparing to the incident power flux. This can be expressed as:

$$F_{ri_0}^{L_1\downarrow}|_{z=0} = F_{ri_0}^{L_1\downarrow}|_{z=R_2-R_1} + F_{d_1}^{L_1\uparrow}|_{z=0} + F_{d_1}^{L_1\downarrow}|_{z=R_2-R_1}. \quad (7.6)$$

This energy constraint is not met in the case of the single scattering solution shown in Fig. 7.3(a), indicating that there is a significant contribution from multiple scattering. The results corresponding to the full solution in Fig. 7.3(b) exhibit the same coherent intensity, but there is an increase in the upward and downward diffuse fluxes and in this case the total scattered energy equals the incident energy.

7.3 Conclusion

A numerical example of the transient RT formulation has been presented and compared to an analytical model derived from wave theory for the special case of a narrow band excitation with a high directivity and the assumption of single scattering. The media can be regarded as a thick layer of air bubbles suspended

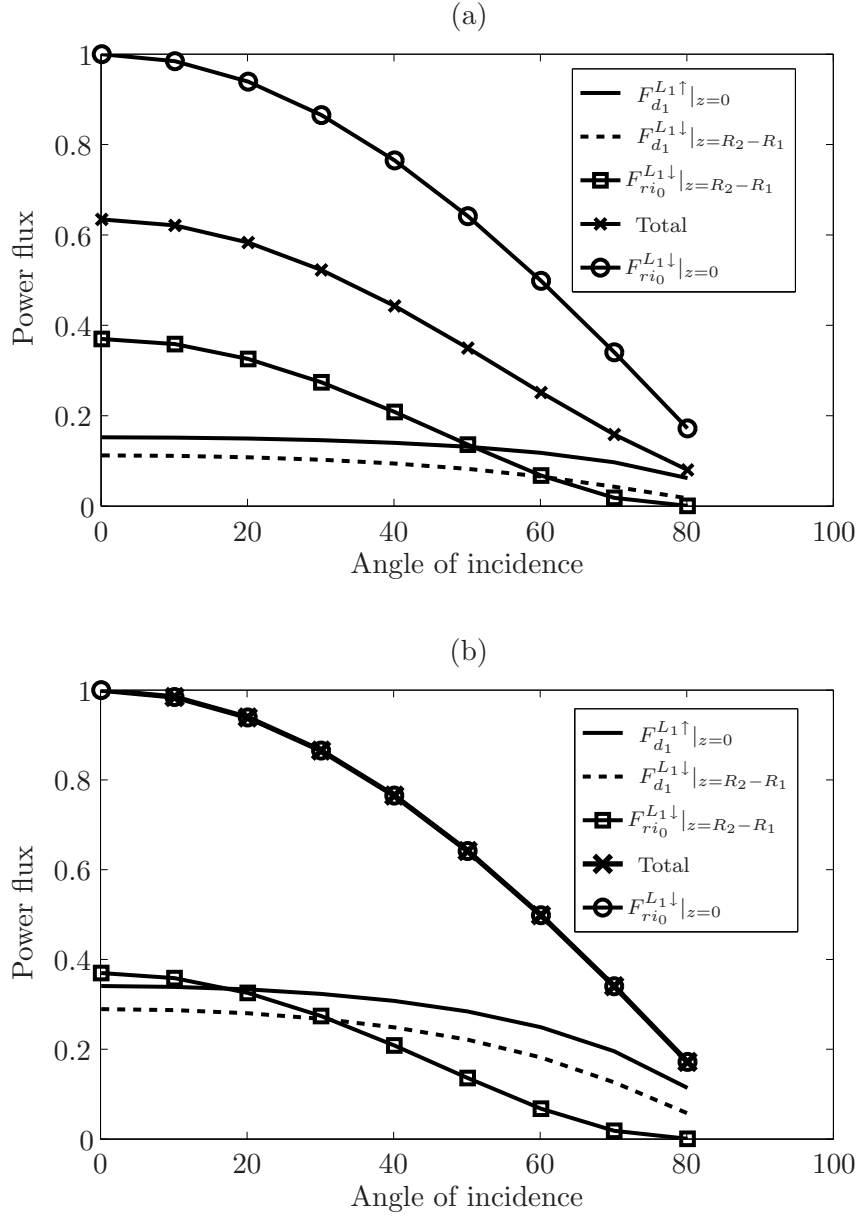


Figure 7.3: Coherent and diffuse normal power fluxes at $z = 0$ and $z = R_2 - R_1$ for: (a) The single scattering solution of the transient RT equation and (b) The full solution. The curve labeled as *Total* refers to the summation in the right hand side of (7.6), and it must equal $F_{ri0}^{L1↓}|_{z=0}$ in conservative media.

in fluid media, and the solution of the transient RT equation including multiple scattering exhibits a slower decay rate as compared to the single scattering solutions, and it is considered more accurate based on arguments of energy conservation. The response of the media to an incident energy impulse can be used as a forward model for comparison to experimental data.

Chapter 8

Conclusion and future work

8.1 Conclusion

Radiative transfer is a promising technique for research of acoustic scattering and propagation in random media. The formulation is based on the equation of transport, which is a statement of the law of conservation of energy as applied to coherent energy interacting with randomly positioned scatterers. The model has been adapted from electromagnetics into acoustics and its application as a seabed scattering model was presented in this work for the first time.

The formulation presented in this work corresponds to the Radiative Transfer for fully elastic media with random independent scatterers distributed in parallel plane layers. This idealized environment is used to introduce some of the common features supported by transport theory: elastic background media with elastic scatterers that can be weak or strong, along with the incorporation of background attenuation, multiple scattering and multiple layers. It is important to keep in

mind that as suggested by applications in electromagnetic remote sensing, more realistic environments can be handled by the RT formulation, including dense distributions of scatterers[48, 49], smooth gradients on the sound speed and/or density[50] and horizontally variable layered environments[51, 52], which are of particular interest in ocean bottom scattering.

The solution of the RT equation for a finite elastic layer with spherical scatterers was implemented and validated, and extensions to include scatterers of arbitrary shape can be easily incorporated. The performance of the RT model was demonstrated using four methods:

1. Laboratory work with a variety of experimental conditions including scatterers in different regimes with strong acoustic contrast, broad frequency band, lossy backgrounds with frequency-dependent attenuation, and environments with multiple layers.
2. Further validation of the RT model was achieved by comparing to field experimental data collected in a region where the seabed consists of three parallel layers, one of which contains trapped gas bubbles (chapter 6).
3. In all cases, energy conservation can be demonstrated for the steady-state and the transient solutions by setting the background attenuation to zero (conservative case).

4. The RT model also performed well when compared to a time-domain scattering model that implements Monte Carlo realizations, developed by Canepa et al [38], as commented in section 5.5.

The main characteristic of the proposed model is its flexibility to accommodate several scattering mechanisms of interest for seabed acoustics. Specifically, the advantages of the proposed model are:

1. The RT model is not subject to some of the assumptions typically required by traditional models, such as small scatterers, small perturbation or high frequency of operation. The tank experiments presented in chapter 5 showed that the RT model is accurate in the Mie and the Geometric Optics regimes, and it has also been validated in the Rayleigh regime[53].
2. Due to the requirement of energy conservation, the RT model has a natural way to incorporate all the polarizations supported by the scattering media, and energy re-distribution from one polarization into another at the layer boundaries or at the surface of the scatterers is implicit in the model.
3. The RT model yields the expected value of the volume scattering taken over multiple realizations of the ensemble of scatterers. This is in contrast to Monte Carlo methods[38], and it might translate into less computation time.

Finally, exploration of the transient RT equation in chapter 7 showed that the full solution including the multiple scattering term can predict the rate of decay of the scattered intensity when an acoustic wave interacts with a finite layer. It was shown that unlike analytical solutions based on single scattering, the transient RT solution meets the conservation of energy. As suggested by Turner et al[15], a potential application of the transient solution is for the extraction of structure information of the sediment such as anisotropy and extinction coefficient, by analysis of time-dependent features in the scattered intensity.

8.2 Future work

The following areas can be considered for further research related to this work:

1. Implementation of the Dense Media Radiative Transfer for acoustics.
2. Extension of the model to include rough interfaces.
3. Radiative Transfer in media with gradients.

8.2.1 Implementation of the Dense Media Radiative Transfer for acoustics

The experimental demonstrations of the RT model in this work were performed with random media in which multiple scattering effects are weak, due to small fractional volume or to the strong effect of background attenuation.

Nevertheless, there are cases in which the scatterers are densely packed and the effect of nearby scatterers becomes strong, so the assumption of independent scatterers is not valid. As an example, it has been shown [4] that at high frequency ($f \approx 100 \text{ kHz}$) water-saturated sediment can no longer be considered as homogeneous, and volume scattering can be measured from the grains of sand in water background, as observed in section 5.4. In order to include these strong multiple scattering effects, the Dense Media Radiative Transfer (DMRT) formulation has been developed in electromagnetics [48, 49].

The DMRT equation has the same form as (3.10), but the scattering cross sections and scattering functions are modified to include the correlation between scatterers. This formulation has not been adapted to acoustics yet, but it would be useful not only in seabed scattering but also in characterization of materials by ultrasound.

8.2.2 Extension of the model to include rough interfaces

The presence of rough interfaces between parallel layers has implications for the way that the coherent energy penetrates in the layer before interacting with the scatterers, as illustrated in Fig. 2.1 (b). If the surface is too rough, the energy enters the sediment at multiple angles defined by a main lobe. If the surface is smooth it results in a narrow main lobe, closer to the case of an ideal flat surface.

The smooth case was observed in the experiment of aluminum spheres with

sand background, where the water-sediment interface was not completely flat. Since the RT model implemented in this work considers only flat interfaces, average over realizations was used to obtain the expected value of the reflection coefficient in section 5.4. Nevertheless, when the roughness is significant it must be included in the RT formulation by modifying the elastic boundary conditions (3.13). There are two general approaches to model rough interfaces [21]: the *perturbation approach*, which applies when the features of the rough surface are much smaller than the wavelength ($h \ll \lambda$ in Fig. 2.1 (b)), and the *Kirchhoff approximation* illustrated in Fig. 8.1 in which the only restriction is for the radius of curvature of the rough features to be greater than λ . In this case, the plane wave reflection coefficients between layers 0 and 1 still apply, but they are modified so the angle of the reflected and the transmitted wave are measured with respect to a local tangent plane.

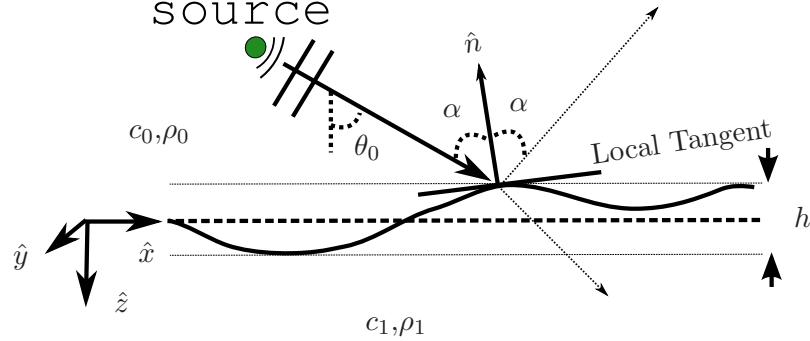


Figure 8.1: Illustration of the Kirchhoff approximation for rough surfaces: with this approach, the plane wave reflection coefficients become a function of the position (x,y) along the rough surface, and the angles of reflection and refraction are defined with respect to the vector \hat{n} , normal to the local tangent.

The Kirchhoff approximation has been applied to Radiative Transfer applications in electromagnetics[54], and it can be included in the proposed scattering model.

8.2.3 Radiative Transfer in media with gradients

In high frequency seabed acoustics, there are numerous examples in which the main mechanism of volume scattering is the presence of gradients in the sound speed of the sediment (Fig. 2.1(c)). To illustrate the typical magnitude of such gradients, Fig. 8.2 shows the depth-dependent sound speed measured in a core sample of sediment from the New Jersey shelf area.

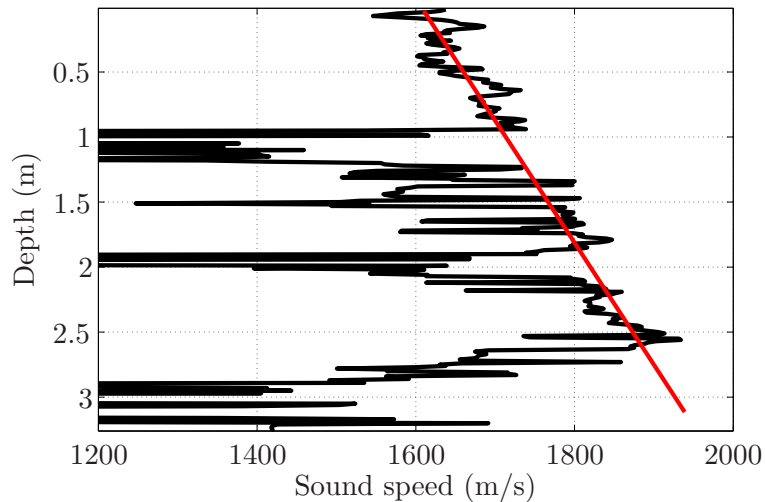


Figure 8.2: Depth-dependent sound speed in a core sample of sediment from the New Jersey shelf area. The red line shows the general trend of the upward refracting sound speed profile. Data provided by Dr. Altan Turgut, NRL.

Comparison of the RT model to data from this regions can be accomplished

by adapting the transport equation to include a depth dependent index of refraction [50, 55, 56]. The most simple implementation is known as the *adding method*, which consists of discretizing the continuous gradient into a stack of thin layers, each one with (almost) constant properties. Then, the transient RT equation is applied to each sub-layer, considering the time delay in the propagation of energy from one segment to the next. A similar approach using reflection/transmission coefficients of plane waves was used to produce synthetic data with similar characteristics as the chirp survey shown in Fig. 1.2(a) [57].

References

- [1] T. K. Stanton, D. Chu, P.H. Wiebe, R.L. Eastwood, and J.D. Warren. Acoustic scattering by benthic and planktonic shelled animals. *J. Acoust. Soc. Am.*, 108(2):535–550, 2000.
- [2] A. P. Lyons, A.L. Anderson, and T.H. Orsi. Modeling acoustic volume backscatter from two shallow-water marine environments by side-scan sonar. In *IEEE proceedings, May 8-11 1994*, pages 862–865, Alexandria, VA, USA, 1994.
- [3] A. P. Lyons and E. Pouliquen. Advances in high-resolution seafloor characterization in support of high-frequency underwater acoustics studies: techniques and examples. *Meas. Sci. Technol*, 15(1):59–72, 2004.
- [4] A. P. Lyons. The potential impact of shell fragment distributions on high-frequency seafloor backscatter. *Meas. Sci. Technol*, 30(4):843–851, 2005.
- [5] A.N. Ivakin. A unified approach to volume and roughness scattering. *J. Acoust. Soc. Am.*, 103(2):827–837, 1998.
- [6] P.D. Mourad and D.R. Jackson. A model/data comparison for low-frequency bottom backscatter. *J. Acoust. Soc. Am.*, 94(1):344–358, 1993.
- [7] D.R. Jackson, D.P. Winebrenner, and A. Ishimaru. Application of the composite roughness model to high-frequency bottom scattering. *J. Acoust. Soc. Am.*, 79(5):1410–1422, 1986.
- [8] D.R. Jackson and M.D. Richardson. *High Frequency Seafloor Acoustics*. ONR. Springer, New York, 2007.
- [9] C. Dezhang, K.L. Williams, D. Tang, and D.R. Jackson. High-frequency bistatic scattering by sub-bottom gas bubbles. *J. Acoust. Soc. Am.*, 102(2):806–814, 1997.
- [10] A. N. Ivakin and D. R. Jackson. Effects of shear elasticity on sea bed scattering: Numerical examples,. *J. Acoust. Soc. Am.*, 103(1):346–354, 1998.

- [11] M.I. Mishchenko and L.D. Travis. *Multiple Scattering of Light by Particles*. None. Cambridge University Press, United Kingdom, 2006.
- [12] A.A. Kokhanovsky. *Optics of Light Scattering Media*. Praxis books in environmental sciences. Springer, United Kingdom, 2001.
- [13] J. A. Turner and R.L. Weaver. Radiative transfer of ultrasound. *J. Acoust. Soc. Am.*, 96(6):3654–3674, 1994.
- [14] J. A. Turner and R.L. Weaver. Ultrasonic radiative transfer in polycrystalline media: Effects of a fluid-solid interface. *J. Acoust. Soc. Am.*, 98(5):2801–2808, 1995.
- [15] J. A. Turner and R.L. Weaver. Time dependence of multiply scattered diffuse ultrasound in polycrystalline media. *J. Acoust. Soc. Am.*, 97(5):2639–2644, 1995.
- [16] L. Margerin. Introduction to radiative transfer of seismic waves. *Geophysical monograph*, 157(1):1–25, 2005.
- [17] A.P. Lyons. The potential impact of shell fragment distributions on high-frequency seafloor backscatter. *IEEE J. Oceanic Engineering.*, 30(4):843–851, 2005.
- [18] P.D. Mourad and D.R. Jackson. A model data comparison for low-frequency bottom backscatter. *J. Acoust. Soc. Am.*, 94(1):344–358, 1993.
- [19] D. Tang. *Acoustic Wave Scattering from a Random Ocean Bottom*. PhD thesis, Massachusetts Institute of Technology and Woods Hole Oceanographic Institution, 1991.
- [20] F.B. Jensen, W.A. Kuperman, M.B. Porter, and H. Schmidt. *Computational Ocean Acoustics*. AIP series on Modern Acoustics and Signal Processing. Springer, New York, 2000.
- [21] Akira. Ishimaru. *Wave Propagation and Scattering in Random Media*. Vol.1 and 2;. Academic Press, New York, 1978.
- [22] Subrahmanyan. Chandrasekhar. *Radiative Transfer*. None. Dover Publications Inc, New York, 1960.
- [23] R.T.Shin and J.A.Kong. Radiative transfer theory for active remote sensing of a homogeneous layer containing spherical scatterers. *J. Applied Physics*, 52(6):4221–4230, 1981.

- [24] T. Okutucu, Y. Yener, and A.A. Busnaina. Transient radiative transfer in participating media with pulse-laser irradiation: an approximate galerkin solution. *J. of Quantitative Spectroscopy and Radiative Transfer*, 103(1):118–130, 2006.
- [25] David J. Griffiths. *Introduction to Electrodynamics*. Prentice-Hall, Inc., New Jersey, 1981.
- [26] D.R. Jackson, K.R. Briggs, K.L. Williams, and M.D. Richardson. Tests of models for for high-frequey seafloor backscatter. *IEEE J. Oceanic Engineering.*, 21(4):458–470, 1996.
- [27] J.E. Quijano and L.M. Zurk. Application of radiative transfer theory to acoustic propagation in the ocean bottom. In *IEEE Oceans Conference, Sept. 29- Oct. 4 2007*, pages 1–7, Vancouver, B.C., 2007.
- [28] S. G. Kargl and K.L. Williams. Double monopole resonance of a gasfilled, spherical cavity in a sediment. *J. Acoust. Soc. Am.*, 103(1):265–274, 1998.
- [29] J.E. Quijano and L.M. Zurk. Modeling acoustics scattering from the seabed using transport theory. In *IEEE Oceans Conference, Sept. 20- Sept. 23 2010*, Seattle, WA, 2010.
- [30] C.F. Ying and R. Truell. Scattering of a plane longitudinal wave by a spherical obstacle in an isotropically elastic solid. *J. Applied Physics*, 27(9):1086–1097, 1956.
- [31] Einspruch N.G., E.J. Witterholt, and R. Truell. Scattering of a plane transverse wave by a spherical obstacle in an elastic medium. *J. Applied Physics*, 31(5):806–818, 1960.
- [32] V.A. Korneev and L.R. Johnson. Scattering of p and s waves by a spherically symmetric inclusion. *Pure and applied geophysics*, 147(4):675–718, 1996.
- [33] R.J. McBride and D.W. Kraft. Scattering of a transverse elastic wave by an elastic sphere in a solid medium. *J. Appl. Phys.*, 43(12):4853–4861, 1972.
- [34] L.M. Brekhovskikh. *Waves in Layered Media*. Applied Mathematics and Mechanics, Vol.16. Academic Press Inc., Florida, 1980.
- [35] Joseph A. Turner. *Radiative Transfer of Ultrasound*. PhD thesis, University of Illinois at Urbana-Champaign, 1994.

- [36] McCord M. Newcomb J. Turgut, A. and R. Fisher. Chirp sonar sediment characterization at the northern gulf of mexico littoral acoustic demonstration center experimental site. In *IEEE Oceans Conference, Oct. 29- Oct. 31 2002*, pages 2248–2252, Biloxi, Mississippi., 2002.
- [37] C. Elbaum R. Truell and B.B. Chick. *Ultrasound methods in solid state physics*. Academic Press Inc, New York and London, 1969.
- [38] A. Tesei R. Guillermin G. Canepa, J.P. Sessarego and R.J. Soukup. A time domain model of scattering from small discrete volume particles: tank validation. In *Proceedings of the ASA-ECUA-Euronoise Conference, June 2008, 2008*, pages 4119–4124, Paris, France., 2008.
- [39] Guoliang J. Jackson D.R Tang, D.J. and K.L. Williams. Analyses of high-frequency bottom and subbottom backscattering for two distinct shallow water environments. *J. Acoust. Soc. Am.*, 96(5):2930–2936, 1994.
- [40] Orsi T.H. Richardson M.D. Fleischer, P. and A.L. Anderson. Distribution of free gas in marine sediments: a global overview. *Geo-Marine Letters*, 21:103–122, 2001.
- [41] J.E. Quijano and L.M. Zurk. Radiative transfer theory applied to ocean bottom modeling. *J. Acoust. Soc. Am.*, 126(4):1711–1723, 2009.
- [42] F. Abegg and A.L. Anderson. The acoustic turbid layer in muddy sediments of eckernfoerde bay, western baltic: methane concentration, saturation and bubble characteristics. *Marine Geology*, 137:137–147, 1997.
- [43] A. Lakew. Study of sediemnt nonlinearity using explotion data in the mississippi embayment. *Pure appl. geophys.*, 165:1835–1860, 2008.
- [44] A. Frankel and L. Wennerberg. Energy-flux model of seismic coda: separation of scattering and intrinsic attenuation. *Bulletin of the Seismological Society of America*, 77(4):1223–1251, 1987.
- [45] R. Tonn. Comparison of seven methods for the computation of q. *Physics of the Earth and Planetary Interiors*, 55(3-4):259–268, 1989.
- [46] LeBlanc L.R. Schock, S.G. and L.A. Mayer. Chirp subbottom profiler for quantitative sediment analysis. *Geophysics*, 54(4):445–450, 1989.
- [47] Kim H.J. Kim D.C. Yi B.Y. Nam S.M. Khim B.K. Lee, G.H. and M.S. Lim. The acoustic diversity of the seabed based on the similarity index computed from chirp seismic data. *Journal of Marine Science*, 66:227–236, 2008.

- [48] L.M. Zurk, L. Tsang, and D.P. Winebrenner. Scattering properties of dense media from monte carlo simulations with application to active remote sensing of snow. *Radio Sci.*, 31(4):803–819, 1996.
- [49] L. Tsang and A. Ishimaru. Radiative wave and cyclical transfer equations for dense non tenuous media. *J. Opt. Soc. Am.*, 2(12):2187–2194, 1985.
- [50] G. Bal. Radiative transfer equations with varying refractive index: a mathematical perspective. *J. Opt. Soc. Am.*, 23(7):1639–1644, 2006.
- [51] K.N. Liou. *Introduction to Atmospheric Radiation*. International Geophysics Series. Academic Press, California, 2002.
- [52] G.A. Titov. Radiative horizontal transport and absorption in stratocumulus clouds. *J. of the Atmospheric Sciences*, 55(1):2549–2560, 1997.
- [53] J.E. Quijano and L.M. Zurk. Tank experiments for validation of volume scattering models. *J. Acoust. Soc. Am.*, 127(3):1938–1938, 2010.
- [54] C.C. Hsu, R.T. Shin, J.A. Kong, A. Beaudoin, and T. Le Toan. Application of theoretical model for microwave remote sensing of forest. In *IEEE Geoscience and Remote Sensing Symposium, Aug. 18- Aug. 21 1993*, pages 595–597, Tokio, Japan, 1993.
- [55] C.C. Chang and C. Wu. Azimuthally dependent radiative transfer in a slab with variable refractive index. *International Journal of Heat and Mass Transfer*, 51:2701–2710, 2007.
- [56] D. Lemonnier and V. Le Dez. Discrete ordinates solution of radiative transfer across a slab with variable refractive index. *J. of Quantitative Spectroscopy and Radiative Transfer*, 73:195–204, 2002.
- [57] J.E. Quijano and L.M. Zurk. Ocean bottom scattering: characterization with chirp sonar. *J. Acoust. Soc. Am.*, 120(5):3321–3382, 2006.

Appendix A

Definition of Stoke's parameters

The definition of the Stoke's parameters used in this work follows that one from Turner et al [13]. Given a wave propagating through random elastic media along the z axis, the energy is partitioned into longitudinal (u_L), shear vertical(u_y) and shear horizontal(u_x) waves. The particle displacement (i.e. the function that describes the oscillation of the particles in the media as the wave propagates) can be written as:

$$\begin{aligned} s_L &= a_L e^{-k_L z - i\epsilon_L} e^{i\omega t}, \\ s_x &= a_x e^{-k_T z - i\epsilon_x} e^{i\omega t}, \\ s_y &= a_y e^{-k_T z - i\epsilon_y} e^{i\omega t}, \end{aligned} \tag{A.1}$$

where a_L, a_x and a_y are the amplitudes of the longitudinal, shear horizontal and shear vertical waves, respectively, ϵ_L, ϵ_x and ϵ_y are the corresponding phases and $k_L = \omega/c_L$ and $k_T = \omega/c_T$ are the longitudinal and transversal wavenumbers. Note that the phase and the amplitude terms are random quantities.

The Stoke's parameters for acoustics are defined[13] as

$$\begin{aligned} I_L &= \left\langle \frac{\rho\omega^3}{2k_L} a_L^2 \right\rangle; \\ I_x &= \left\langle \frac{\rho\omega^3}{2k_T} a_x^2 \right\rangle; \\ I_y &= \left\langle \frac{\rho\omega^3}{2k_T} a_y^2 \right\rangle; \\ U &= \left\langle \frac{\rho\omega^3}{k_T} a_x a_y \cos(\epsilon_y - \epsilon_x) \right\rangle; \\ V &= \left\langle \frac{\rho\omega^3}{k_T} a_x a_y \sin(\epsilon_y - \epsilon_x) \right\rangle; \end{aligned} \tag{A.2}$$

where the operator $\langle \ . \ \rangle$ indicates the expected value. From this definition,

it is concluded that I_L , I_x and I_y represent the power carried by each of the polarizations. The parameters U and V represent the interference between the two shear waves, and no energy is transported by those parameters. Therefore, U and V will be ignored in any computation related to energy conservation of the RT model.

Appendix B

Publications and talks related to this research

Talks given by the author:

1. “Ocean bottom scattering: characterization with chirp sonar”, presented at the 152nd meeting of the Acoustical Society of America, Honolulu, Hawaii. Nov., 2006.
2. “Application of Radiative Transfer Theory to Acoustic Propagation in the Ocean Bottom”, presented at the IEEE Oceans Conference, Vancouver, Canada. Sept., 2007.
3. “Analysis of acoustic backscattering from the ocean bottom using radiative transfer theory”, presented at the 155th meeting of the Acoustical Society of America, Paris, France. June, 2008.
4. “Scattering from an ocean bottom layer using steady-state and transient radiative transfer”, presented at the 156th meeting of the Acoustical Society of America, Miami, Florida. Nov., 2008.
5. “Tank experiments for validation of volume scattering models”, presented at the 157th meeting of the Acoustical Society of America, Baltimore, MD, April, 2010. **This work was awarded the second price to the best student talk in underwater acoustics.**
6. “Scattering from large inclusions using radiative transfer method” (Invited Talk), presented at European Conference on Underwater Acoustics (ECUA), Istanbul, Turkey. July, 2010.
7. “Modeling acoustics scattering from the seabed using transport theory”, presented at the IEEE Oceans Conference, Seattle, Washington. Sept., 2010.

Publications:

Two conference papers[27, 29] and a journal paper[41] contain part of the work related to the proposed RT scattering model.